Hybrid Quantum Dots in InAs Nanowires

Inauguraldissertation

zur
Erlangung der Würde eines Doktors der Philosophie
vorgelegt der
Philosophisch-Naturwissenschaftlichen Fakultät
der Universität Basel

von

Lukas Hofstetter
aus Langnau i.E., BE

UNI
BASEL

Basel, 2011

Genehmigt von der Philosophisch-Naturwissenschaftlichen Fakultät
auf Antrag von
Prof. Dr. C. Schönenberger
Prof. Dr. L. P. Kouwenhoven
Prof. Dr. K. Ensslin
Dr. Sz. Csonka

Basel, 25.5.2011

Prof. Dr. Martin Spiess
Dekan

Contents

1 Introduction 1

2 Background 5
2.1 InAs nanowires 5
2.1.1 InAs quantum dots 7
2.2 Kondo effect 12
2.3 Superconductivity 15
2.3.1 BCS theory 15
2.3.2 Andreev processes 19

3 Basics of sample fabrication and experimental setup 23
3.1 General fabrication steps 23
3.2 Experimental setup 27

4 Giant g-factor fluctuations in InAs nanowires quantum dots 31
4.1 Fabrication and measurement setup 31
4.2 Device characterization 32
4.3 Observation of g-fator fluctuations: main results 35
4.4 Discussion 37
4.5 Summary and outlook 40

5 InAs nanowire quantum dots with ferromagnetic and superconducting leads 43
5.1 Fabrication and measurement setup 44

5.2 Ferromagnetic proximity effect: theory 45
5.3 Ferromagnetic proximity effect: results 48
5.4 S-QD-F devices as spectroscopy tool for the ferromagnetic proximity effect without Kondo correlations 56
5.5 Summary 58

6 Cooper pair splitting in a two-quantum-dot Y-junction 61
6.1 Background, concept and principle of Cooper pair splitting . 62
6.1.1 Entanglement 62
6.1.2 Superconductors as source of EPR pairs 65
6.2 Fabrication and measurement setup 68
6.3 Measurement principle 70
6.4 Observation of Cooper pair splitting 73
6.4.1 Main results 73
6.4.2 Gate dependence of the Cooper pair splitting 75
6.4.3 Temperature and magnetic field dependence 76
6.5 Discussion 79
6.6 Approaches to optimize the splitting efficiency 81
6.6.1 Replacing aluminum by niobium 82
6.6.2 Tuning the tunnel barriers 83
6.7 Summary and outlook 89

7 Finite bias Cooper pair splitting 93
7.1 Introduction 93
7.2 Device fabrication and measurement setup 94
7.3 Measurement principle 96
7.4 Observation of “non-local” signals at finite bias 97
7.5 Discussion 100
7.6 Summary 103

A Additional data to chapter 6 115

B Fabrication recipes 119

Publications 123

Curriculum Vitae 125

Acknowledgments 127

CHAPTER 1

Introduction

Electron transport through nanostructures is of great interest for fundamental research as well as industrial applications. Due to their precise structural control and integration feasibility, nanowires (NWs) emerge as one of the most promising candidates for these purposes [1]. The dimensions of the nanowires allow investigations of transport at the single electron level in so-called *quantum dots* (QDs) [2]. These structures can be viewed as artificial atoms where the geometrical confinement of the electron wavefunctions in all three spatial dimensions results in discrete energy levels. In addition to their use to explore fundamental transport phenomena, QDs have been proposed as possible candidates of *quantum bits* [3]. These *qubits*, in contrast to their classical counterparts, exist not only in the state "0" or "1", but also in coherent superpositions of them. Two or more qubits can be *entangled* with each other. This quantum mechanical property leads to an intriguing connection between the qubits which can be used to construct specific "quantum-algorithms" with significant computational speed-up compared to implementations on classical computers. NWs with their highly controllable growth [4, 5] and scalability [6, 1] are good candidates for the realization of quantum bits. A particularly promising NW material is InAs. This is highlighted by recent experimental results in InAs NW based qubits, where purely electrical single-qubit control is demonstrated utilizing the material specific strong spin-orbit interaction [7]. In addition, hybrid QDs can be realized with InAs NWs facile by standard methods. The term *hybrid* in this context means that the NWs can be contacted with superconducting

or ferromagnetic materials alongside normal metal leads, which allows to inject the different electron correlations of these materials and exploit their interplay in a nanoscale object.
In this thesis measurements performed on InAs NW based hybrid QDs are presented. The thesis is organized such, that the main chapters (4,5,6 and 7) contain all the relevant information to be read independently. Additionally, **chapter 2** provides the basics of InAs NWs, QDs, Kondo physics and superconductivity and in **chapter 3** details on InAs NW based device fabrication and low temperature measurement setups are given.
In **chapter 4**, the level dependence of the g-factor of InAs NW quantum dots is investigated. The g value is the key parameter for spin manipulation at the single electron level. Thus, its tunability and control is highly desirable for experiments where different spin states need to be addressed individually (e.g. qubit control).
In **chapter 5** the transport in InAs NW QD structures is explored that are contacted with a ferromagnetic and a superconducting lead. The proximity-induced exchange field in the QDs is analyzed in the Kondo regime. Furthermore, it is shown that a superconducting contact can serve as spectroscopy tool for the visualization of the ferromagnetic exchange field in the absence of Kondo correlations.
Chapter 6 is dedicated to the study of Cooper pair splitting in a two-quantum dot Y-junction. Cooper pairs are electron pairs in an s-wave superconductor, which occur naturally in a spin-singlet state [8]. Therefore, extracting Cooper pairs from the superconductor is a possible source of electrically controllable electron-electron entanglement. The experiment follows closely the proposal by Recher *et al.* [9], who suggest to make use of the Coulomb interaction in quantum dots, for the controlled generation of spatially separated entangled Einstein-Podolsky-Rosen (EPR) pairs [10]. Besides the interest to study fundamental quantum mechanical properties, such entangled pairs could e.g. be used for entanglement distribution to synchronize quantum circuits or to investigate non-classical correlations in other materials. In chapter 6, the first

Figure 1.1: Illustration of the Cooper pair splitting.

realization of an electrically tunable Cooper pair splitter is presented. In addition, experiments to optimize the splitting efficiency are discussed. The chapter is closed by a summary and detailed outlook for future experiments. In **chapter 7** preliminary results on a Cooper pair splitting experiment at finite bias are shown. It seems that if the device is operated at finite bias, the relative rates of Cooper pair splitting and elastic cotunneling can be tuned by exploiting the gate dependence of the level energy and the density of states at the relevant energies.

All the experiments are focusing on essential building blocks in the field of solid-state quantum computation with electrons. The control of the g-factor is needed to address selectively the spin states of individual qubits. The magnetic proximity effect is promising for the use of efficient spin filtering, necessary for the detection of entanglement in split Cooper pairs. And the control over a source that generates spatially separated spin-entangled electrons is of importance for applications in the context of on-chip quantum computation.

CHAPTER 2

Background

In this thesis experiments in InAs nanowire (NW) quantum dots (QDs) are discussed. Due to the reduced dimensions of the NWs (diameter $\approx$ 100 nm, see Fig. 2.1) the work is centered around phenomena where the wave-nature of the partaking constituents plays a major role. In the following single electron tunneling, the superconducting proximity effect and the Kondo effect are introduced, to build the theoretical fundament for the subsequently presented experiments. In this short theory chapter only the basics to understand the presented experiments are given. Specific theoretical models for the interpretation of each experiment, are described in the corresponding chapters.

2.1 InAs nanowires

The experiments in this thesis have been performed with molecular beam expitaxy (MBE) grown nanowires from the III-V semiconductor material InAs. The NWs were provided by the group of Jesper Nygård from the Niels Bohr Institute in Copenhagen. Nanowires are one of the most promising building blocks for quantum transport devices [1]. A scanning electron microscope (SEM) image of a typical InAs NW is shown in Fig. 2.1. The Au catalyst particle from the MBE growth is clearly visible. NWs are typically 2-5 μm long and have diameters ranging from a few tenth of nanometers to around 150 nm, depending on the growth parameters. They are covered by a few

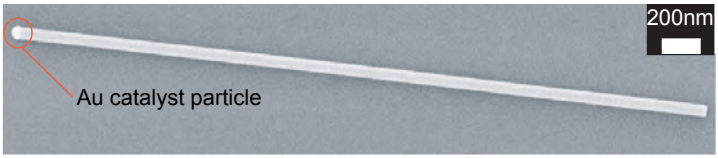

Figure 2.1: *An SEM image of a typical InAs NW as used in the experiments of this thesis. Inside the red circle the Au catalyst particle from the MBE growth is still visible.*

nanometer thick native oxide layer (see below) [11]. For the measurements shown in this thesis NWs with diameters between 60-80 nm were chosen. Too thin NWs are unsuitable for transport measurements, since the mobility ($\approx 4000\ cm^2/Vs$ at $T = 300$ K), is decreasing rapidly if the diameter gets below ≈ 40 nm [12]. In the bulk InAs forms a zincblende (ZB) crystal with well known band properties: A direct band gap of $E_g^{ZB} = 0.42$ eV, a g-factor of -14.7 and an effective mass of $m^* = 0.026\ m_e$ [11, 13]. The large g-factor indicates the presence of a strong spin-orbit interaction, which can be useful e.g. for the control of quantum bits [7]. Also for the detection of the exotic Majorana fermions strong spin-orbit is a necessity [14], rendering InAs NWs an optimal candidate to search for these particles. InAs NWs occur also in wurtzite (WZ) crystal structure [15]. Even though the WZ structure has been observed in various experiments [16, 17, 11], experimental [18, 19] and theoretical [20, 21] data about band properties has become available only recently. Commonly, WZ is found to have a higher band gap than ZB, with experiments yielding energies between 0.52 eV and 0.54 eV, roughly in agreement with the theoretical results around 0.47 eV - 0.48 eV. Thus, the energy difference of the band gap between ZB and WZ is of the order of the Fermi energy ($E_F = 60$ meV [22]) of NWs with average radii of 100 nm. Therefore, in addition to defects, crystal structure changes within a single NW might influence transport properties or even the device fabrication (e.g. different etching rates, see section 6.6). Recent progress in growth techniques [4, 5] allows to create defect-free, single-crystal NWs. This will diminish the mentioned issues and probably increase the mean free path ($l_e \approx 60 - 100$ nm at 8 K [13]).
The great control of their growth (e.g. size, crystal structure) [4], their semiconducting nature (e.g. ease of carrier tunability by gate voltages) and the electronic properties (e.g. high mobility, strong spin-orbit interaction) makes InAs NWs a suitable material for fundamental transport studies. In addition, no Schottky barrier is formed in contact with a metal, due to pinning of the metals Fermi level in the conduction band [23]. This is different

from most other semiconductors. InAs NWs make also very good contact to superconducting (S) and ferromagnetic (F) materials [24, 11, 25] allowing to construct interesting S-F hybrid devices [26]. Before contacting the InAs nanowires with any material their few nanometer thin oxide layer has to be removed (see chapter 3). For certain applications the oxide is even useful: If devices with topgates are fabricated (see e.g. chapter 4, 6 & 7), it serves as reliable gate oxide. Voltages up to a few volts can be applied before it breaks down and it seems to induce less noise due to trap charges than artificial oxide layers [27].
The experiments in this thesis rely strongly on InAs NW based quantum dots. QDs, as discussed in the following subsection, are small electronic islands with quantized energy levels, similar to atoms. There are several experimental techniques to realize QDs in InAs NWs. In this thesis, QDs are created between two contacts ≈ 300 nm apart along the NW axis (Fig. 2.2a). In accordance with [2, 28, 11] barriers are generated close to the contacts if the carrier density is reduced by appropriate gate voltages. However, the exact origin of the barriers in InAs NW QDs is still not fully clear [5, 29, 30, 31]. Therefore, for future experiment it would probably be more elegant, to generate the confinement potential by etching [32, 33] or electrostatic means (e.g. topgates or bottomgates) [34, 27, 7].

2.1.1 InAs quantum dots

QDs are small electronic islands with discrete energy levels. These islands are formed due to confinement of the electron wave functions in all three spatial directions. Only certain standing-wave solutions are allowed, determined by the exact shape of the confinement potential. These *zero-dimensional* (0D) objects are realized in various systems (e.g. two-dimensional electron gases (2DEGs), carbon nanotubes (CNTs), metallic nanoparticles, self-assembled systems, nanowires, etc.). The QDs are often characterized by electronic transport measurements at low temperatures (millikelvin regime), where the small thermal energy allows to resolve the QD energy levels. Due to the small size of these systems, adding an additional electron to the island is linked to a considerable energy need (*the charging energy*), as a result of the Coulomb repulsion from the QD electrons. Thus, the transport across such a QD is usually governed by single electron transfer and can only take place if the necessary charging energy is available. QDs and their electronic properties are of fundamental importance for the presented experiments. Therefore, the basics of the governing transport mechanisms are discussed here in more detail. For extensive reviews on this topic see for example [35, 36, 37].
When a nanowire is contacted by two leads (source (S) and drain (D)), a QD

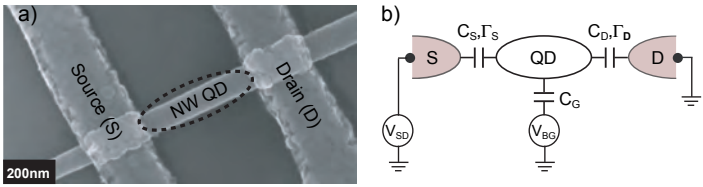

Figure 2.2: *a) An SEM close-up of a NW contacted by two leads. Between the leads a quantum dot (QD) can form. b) Schematic of a QD connected to a source (S) and drain (D) lead by specific barriers (characterized by the tunnel coupling $\Gamma_{S,D}$ and the capacitances $C_{S,D}$). In addition, a gate voltage V_{BG} is capacitively coupled to the QD.*

system is generated between them due to the formation of tunnel barriers (Fig. 2.2a). The barriers are characterized by the QD's coupling strength $\Gamma_{S,D}$ and the source and drain capacitance $C_{S,D}$. Gate voltages (V_{BG}) can also be capacitively coupled to the QD to tune its energy levels. The connections of the leads and the gates to the QD are depicted schematically in Fig. 2.2b. As shown in Ref. [36], a commonly used, simplified description of this system is the *constant interaction model, CIM*. For its validity two assumptions have to be made: The number of electrons on the QD (N) has no influence on the energy levels of the system and the interaction between the electrons on the QD and the environment are captured by a single total capacitance $C_{tot} = C_S + C_D + C_G$. In *CIM*, the total energy $\hat{U}$ of a QD with D on ground and containing N electrons is given by [38]

$$\hat{U}(N) = \frac{(q(N - N_0) + C_S V_{SD} + C_G V_G)^2}{2C_{tot}} + \sum_{n=1}^{N} E_n. \tag{2.1}$$

N_0 is the number of electrons at zero gate voltage and $q = -|e|$ is the electron charge. Since the energy spectra of a QD and an atom are similar, the single particle levels are often called *orbitals* and E_n the energy of the nth electron orbital. The electrochemical potential of the QD is defined as $\mu_{dot}(N) = \hat{U}(N) - \hat{U}(N-1)$, i.e. the energy required to add one electron to the QD. From the electrochemical potentials for N and $N+1$ electrons on the QD the difference between the discrete energy levels, the *addition energy* E_{add}, can be calculated:

$$E_{add} = \mu_{dot}(N+1) - \mu_{dot}(N) = U + \delta E \tag{2.2}$$

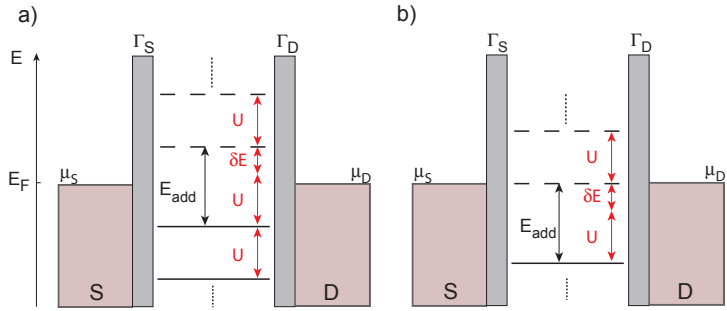

Figure 2.3: *Typical energy diagram of a QD coupled to a source (S) and a drain (D) lead at $T \to 0$. μ_S and μ_D correspond to the electrochemical potential of the leads. $\Gamma_{S,D}$ are the coupling of the leads to the QD. The discrete energy levels and the addition energy of the QD is depicted. Occupied states are drawn with full lines, empty states are drawn with dashed lines. a) Off resonance situation. The number of electrons is fixed. b) The 1st empty QD level is brought in resonance with μ_S and μ_D generating transport through this level.*

Here, $U = e^2/C_{tot}$ is the charging energy of the QD (not to be confused with the previously introduced $\hat{U}$) and $\delta E = E_{n+1} - E_n$ the *orbital level spacing*. In this model the orbitals are spin-degenerate in the absence of interactions and magnetic fields, resulting in $E_{add} = U$ for adding a second electron to the same orbital.

In Fig. 2.3a, a typical energy diagram of a QD coupled to S/D leads is illustrated. The dashed lines are empty states whereas the full lines correspond to occupied ones. Not shown in the drawing is the tunnel broadening of the single particle levels. In Ref. [37], within a resonant tunneling model, it is shown that for low temperatures ($k_B T \ll \Gamma$) the broadening of the QD levels can be described by Lorentzian profiles with $\Gamma = \Gamma_S + \Gamma_D$ being the full-width at half-maximum (FWHM). This so-called Γ broadening of the QD states can be understood by considering the Heisenberg uncertainty relation $\Delta E \Delta t \geq h$. An electron in the QD will in a time interval $\Delta t \approx h/\Gamma$ leave into one of the leads. Thus, due to the uncertainty principle, the electron energy on the QD is only defined within ΔE, determined by the tunnel rate Γ/h. Another effect of the low temperatures besides the Γ broadening of the particle levels is the possibility to describe the electron occupation in the leads by the $T \to 0$ approximation of the Fermi-Dirac distribution, i.e. by a step-function. In Fig. 2.3a and b, this is sketched by the S and D density of states (DOS) with their corresponding electrochemical potentials μ_S and μ_D. All the QD levels below $\mu_{S,D}$ are occupied, the ones above are empty.

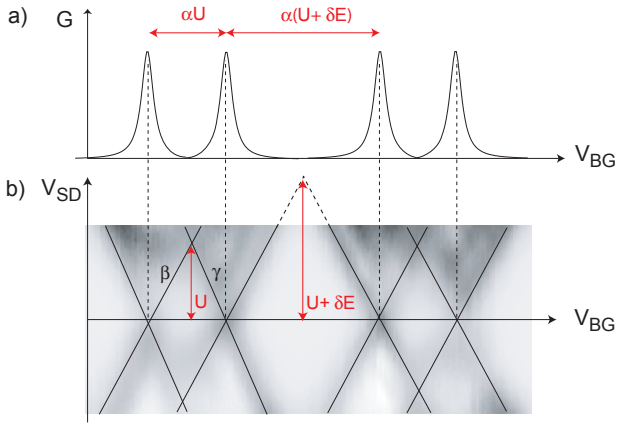

Figure 2.4: *a) A schematic of a conductance versus gate measurement in an ideal QD for $k_BT \ll \Gamma \ll \delta E, U$. Whenever a QD level is in resonance with μ_S and μ_D a resonance peak appears, otherwise transport is forbidden due to Coulomb blockade. b) A $G(V_{BG}, V_{SD})$ measurement performed at $T = 4.2K$ is shown. For illustration reasons the high conductance (dark colors) regions are highlighted resulting in so-called Coulomb diamonds. Within the white/grayish regions, transport is strongly suppressed due to Coulomb blockade and the number of electrons on the QD is constant. β and γ correspond to the two slopes of the Coulomb diamonds.*

For $\mu_S = \mu_D$, electron transfer is only possible if the QD level is in resonance with the electrochemical potential of the leads (Fig. 2.3b). Otherwise the next available level can only be accessed if E_{add} is overcome, as depicted in Fig. 2.3a. Since this is not possible for the used temperatures in the investigated NW QDs where $E_{add} \sim meV > k_BT$, the system is said to be in the *Coulomb blockade*. It should be noted that this is only true if the above-mentioned level broadening is not too large, i.e. the tunnel resistances are larger than the quantum resistance h/e^2 [35]. Otherwise Coulomb blockade can not be seen. As long as the QD is in Coulomb blockade, the number of electrons on it is fixed. A possibility to bring QD levels into resonance with the leads is to apply an appropriate gate voltage. Sweeping the gate voltage and measuring the differential conductance $G = dI/dV$ (see chapter 3), a characteristic pattern of Coulomb blockade alternating with Coulomb peaks is observed, as shown in Fig. 2.4a. The spacing between the Coulomb peaks is $\alpha(\delta E + U)$ for *even* occupation of the QD and αU for an *odd* number of electrons on the QD. The prefactor α is the *leverarm*, arising from the fact that the gate is only capacitively coupled to the QD levels (see Fig. 2.2b), thus $\alpha = e\frac{C_G}{C_{tot}}$.
Transport through the QD can also be generated by applying a DC voltage

V_{SD} across the two contacts. As depicted in Fig. 2.2b, the voltage is applied on S with D kept on ground. This means that, by applying a negative voltage, the electrochemical potential of the source μ_S shifts upwards. Therefore, a finite V_{SD} generates a transport window where i.e. $\mu_S \geq \mu_{dot} \geq \mu_D$ and an electron can tunnel from the source to the QD and then off to the drain. Using the "tuning knobs" V_{BG} and V_{SD} simultaneously, the QD can be characterized. In a typical measurement the differential conductance as a function of V_{BG} and V_{SD} is measured. Fig. 2.4b shows the outcome of such a measurement. Diamond-shaped regions with high G borders (black lines and dark background color) are visible. These borders correspond to resonance positions where a QD level is aligned with either μ_S, μ_D or both. Inside these regions (white/gray background) the QD is in Coulomb blockade. Thus, transport is strongly suppressed and the number of electrons on the QD is fixed. Therefore, these $G(V_{BG}, V_{SD})$ measurements with the resulting Coulomb diamonds are often referred to as *stability diagrams*. Comparing the height of the Coulomb diamonds with the distance between the corresponding Coulomb peaks from a cut along $G(V_{BG}, V_{SD} = 0)$, allows to determine the leverarm α (see Fig. 2.4). In addition, from the slopes of the Coulomb diamonds (β and γ in Fig. 2.4) the system's capacitances C_G, C_S and C_D can be calculated. For this, one needs to consider that by applying a negative voltage on the S contact not only μ_S gets shifted to higher energies, but μ_{dot} gets affected via C_S as well (see Fig. 2.2b). Thus, starting from a resonance situation at $V_{SD} = 0$ V, γ can be obtained by calculating the needed V_{BG} voltage to leave D in resonance with the QD, if V_{SD} is varied. The capacitive correction $\Delta\mu_{dot} = eV_{SD}\frac{C_S}{C_{tot}}$ has to be compensated by the gate voltage such that $\Delta V_{BG}\frac{C_G}{C_{tot}} = -\Delta V_{SD}\frac{C_S}{C_{tot}}$. Hence, the slope γ for this resonant situation is given by $-C_G/C_S$. Similarly, the slope β can be calculated to be $C_G/(C_{tot} - C_S)$. With α, β and γ all information for obtaining C_G, C_S and C_D are in principle available. Additionally, it is simple to show that β and γ allow for an alternative method to calculate the leverarm $\alpha = e\frac{\beta|\gamma|}{\beta+|\gamma|}$.

Depending on the coupling $\Gamma_{S,D}$ and the temperature, there is more information available in such stability diagrams. For low coupling excited state lines are often visible which correspond to tunneling events through excited states instead of the ground state. These appear at V_{SD} voltages where besides the ground state also an excited state starts to enter the bias window. *CIM* only allows electron transport in the resonant case due to the otherwise present Coulomb blockade. In more elaborate models transport within the Coulomb blockade through virtual intermediate states is also accounted for. Such higher order processes can be observed in systems with more transparent barriers and are referred to as *cotunneling* events [39]. Depending

on the total energy of the QD after the tunneling, the event is called elastic (same energy as before tunneling) or inelastic (final state differs from initial one), respectively. A peculiar result of such cotunneling events is the *Kondo effect* [40] which will be discussed in more detail in the following section.

2.2 Kondo effect

The Kondo effect plays a major role in some of the main chapters of this thesis, therefore a short introduction is presented. In 1964, Jun Kondo provided the explanation for a phenomenon already experimentally observed in the 1930's: The resistance below a critical temperature (the Kondo temperature T_K) increased logarithmically in metals containing magnetic impurities [40]. Antiferromagnetic screening of the impurity by surrounding conduction electrons results in the formation of a singlet state between the screening conduction electrons and the localized impurity. This so-called *Kondo singlet* is a more effective scatterer than the localized impurity itself, giving rise to the observed resistance increase [41]. However, if the magnetic impurity is a localized state coupled to two leads (e.g. a single spin in the highest spin-degenerate orbital of a QD) this resistance increase is not observed. Instead, as suggested by Glazman and Raikh in 1988, a fully transmitting channel ($G = 2e^2/h$) emerges towards $T = 0$ K [42]. Ten years later, first observations of the Kondo effect in QD systems were achieved [43, 44], triggering tremendous interest in experimental and theoretical physics alike [45].
A good insight for the formation of the Kondo-singlet can be gained by considering a magnetic impurity embedded in a metallic host as shown e.g. in Ref. [41]. A localized electron situated on the impurity site (e.g. with spin-↑) can lower its kinetic energy by spreading its wavefunction if it is virtually hopping to an empty state at the Fermi energy of the metal. Free spin-↑ states are needed for this, which indicates an excess of spin-↓ conduction electrons in the vicinity of the impurity. Converting delocalized conduction electron states into these semi-localized spin-↓ states costs energy. Therefore, the screening of the impurity is essentially a competition between the energy gain by delocalizing the wavefunction of the impurity electron through virtual hopping in/out of the localized site and the energy cost to create the free states for this process. At low enough temperatures (below T_K) the delocaliztion is favorable and the Kondo-singlet forms.
The calculations of the Kondo problem in a QD starting from the corresponding Anderson Hamiltonian is beyond the scope of this introduction and a more complete review is given in [46]. The above picture of the formation of the Kondo singlet also holds for QD systems. However more often the following, equivalent description is used. In a QD tuned to an odd-

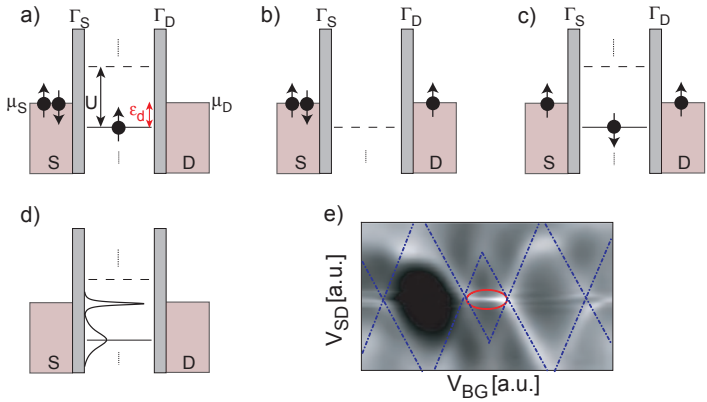

Figure 2.5: *Successive spin-flip cotunneling events (a,b,c) lead to a formation of an extra peak in the DOS of the QD pinned at the Fermi energy of the leads (d). This becomes visible in $G(V_{BG}, V_{SD})$ measurements in odd occupied charge states as finite conductance at $V_{SD} = 0\,V$ within the Coulomb blockade region (e).*

state and with sufficiently transparent tunnel barriers, the spin-1/2 Kondo effect can arise due to successive *spin-flip* cotunneling events [44]. These cotunneling processes result in a screening of the localized spin residing on the QD and the formation of an extra conductance channel through the QD. Fig. 2.5a,b,c illustrate this in more detail. The model system is a single electron in the highest spin-degenerate orbital of a quantum dot. The QD level with the single localized spin, has an energy of ϵ_d with respect to the Fermi energy of the leads. Double and zero occupations are prohibited due to the Coulomb blockade. Good coupling allows tunneling processes through virtual intermediate states within the allowed time window given by the Heisenberg uncertainty principle. Since the QD level is degenerate, the localized electron on the QD can be in either of the two quantization orientations, e.g. spin-↑ or spin-↓. If the electron in the QD is in the spin-↑ state it may tunnel out into the lead D when it gets replaced sufficiently fast (h/Γ) by another electron from lead S. This lead electron may be in the spin-↓ state. The entire process is called a spin-flip cotunneling event. Successive spin-flip cotunneling leads to the formation of a screening cloud associated to the QD spin and the opening up of a transport channel, which manifests itself in the formation of an additional peak in the density of states (DOS) of the QD pinned at the Fermi level of the leads (see Fig. 2.5d). As a result of the extra DOS a finite conductance at $V_{SD} = 0$ V in the Coulomb blockade region of the odd state can be observed (see red circle in Fig. 2.5e).

The width of this zero bias conductance Γ_K is related to the Kondo temperature T_K: $\Gamma_K \sim k_B T_K$. The Kondo temperature T_K is the binding energy between the localized unpaired electron and the surrounding lead electrons. For $\epsilon_d \sim -U/2$, T_K is given by [47]

$$T_K = \frac{\sqrt{\Gamma U}}{2} e^{\pi \epsilon_d (\epsilon_d + U)/\Gamma U}. \tag{2.3}$$

It is evident by looking at Eq. 2.4 that the strength of the Kondo effect can be varied by tuning QD parameters such as the charging energy U, the level position ϵ_d or the coupling Γ. The temperature dependence of the conductance maximum of the Kondo resonance has been shown to follow a logarithmic behavior, being maximal for $T \to 0$ [47]. Thus, a well established check for attributing zero bias anomalies to the spin-1/2 Kondo effect is the increase in $G(V_{BG}, V_{SD} = 0)$ between every other Coulomb peak if the temperature is lowered.

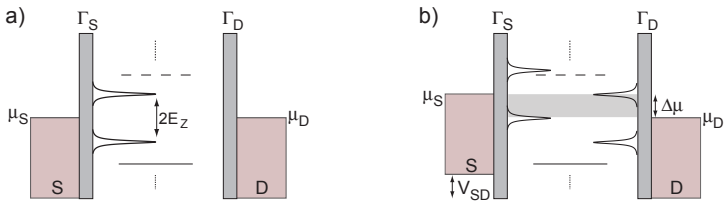

Figure 2.6: *a) Kondo DOS at finite magnetic field B. The DOS peak splits up into a doublet separated by $2E_Z = 2g\mu_B B$. In this situation the formation of a Kondo singlet is suppressed. b) Non-equilibrium ($V_{SD} \neq 0$) situation at finite magnetic field. A split Kondo DOS peak gets pinned at the electrochemical potential of each lead. Whenever $|eV_{SD}| = g\mu_B B$ a Kondo resonance per lead with opposite spin direction is aligned with μ_S and μ_D, respectively. Schematics after [48]*

The magnetic field evolution of a Kondo resonance exhibits also characteristic signatures in transport measurements. Meir *et al.* calculated the QD DOS for non-equilibrium situation and finite magnetic field [48]. Starting from the Anderson Hamiltonian for a QD they showed that the Kondo induced DOS peak splits by twice the Zeeman splitting, $E_Z = g\mu_B B$ in a finite external magnetic field B. g is the Landé g-factor[1] and μ_B is the Bohr magneton. Fig. 2.6a illustrates this splitting. For clarity, the DOS

[1] For InAs NWs the g-value can vary for different orbitals due to fluctuations in the spin-orbit interaction (see also chapter 4).

peaks of the QD is omitted. Clearly, the magnetic field also lifts the spin degeneracy of the QD levels. Thus, spin-flip cotunneling events as shown in Fig. 2.5a,b,c leave the QD in an excited state. In equilibrium ($\mu_S = \mu_D$), the energy for this inelastic cotunneling process is not available. However, if finite bias is applied such that $\Delta\mu = |\mu_S - \mu_D| = g\mu_B B$, the energy comes available and peak in the differential conductance is observed. This can be understood intuitively by looking at Fig. 2.6b where the Kondo DOS in the non-equilibrium situation (i.e. $V_{SD} \neq 0$ V) is depicted. A split Kondo peak gets pinned at the electrochemical potential of each lead, shifting together with μ_S and μ_D if the V_{SD} voltage changes. By applying a bias voltage such that $eV_{SD} = g\mu_B B$, one of the split Kondo peak per contact (with opposite spin) species crosses the electrochemical potential of the opposite lead. This gives raise to the observed finite bias Kondo resonances in $G(V_{BG}, V_{SD})$ measurements [48].

2.3 Superconductivity

Superconductivity is an other well-known many-body effect in solid state physics. Kammerlingh Onnes discovered one of the predominant effects of superconductivity, namely vanishing resistance below a critical temperature, in the beginning of the 20th century [49]. But, similarly to the Kondo effect, it took decades to get a microscopic description of the governing principle. In 1957 Bardeen, Cooper and Schrieffer introduced the so-called *BCS theory*, revolutionizing the understanding of superconductivity [8]. In following subsections, the BCS theory is briefly discussed and the transport mechanisms at the interfaces of normal/ferromagnetic (N/F) and superconducting (S) materials are presented.

2.3.1 BCS theory

Cooper laid the foundation for the BCS theory in 1956 [50]. Taking inputs from earlier works he showed that in the presence of even a very weak attractive interaction, electrons with wavevectors $\boldsymbol{k} > \boldsymbol{k_F}$ can form bound pairs (so-called *Cooper pairs*) with energies lower than the Fermi energy of the system (for a derivation of this remarkable effect see e.g. Ref. [49]). For most superconducting materials the origin of this attractive interaction is phonon-mediated and can be understood intuitively: An electron moving through the material attracts ion cores due to the Coulomb interaction. The resulting positive excess charge attracts the other electron and results in an effective attraction between the two electrons. For the formation of a Cooper pair this

attractive interaction needs to be larger than the repulsive Coulomb interaction. Approximating the time for maximal displacement of the ion cores equilibrium position by the Debye frequency ($\omega_D = k_B\Theta_D/\hbar$), it is evident that the polarizing electron has already moved hundreds of Ångstroms further until the other electrons get maximally attracted. Over this distance the Coulomb repulsion of the two electrons is efficiently screened, leaving room for the necessary net attraction for the Cooper pair formation. Generally, for the derivation of this result, two electrons are added to a Fermi sea with the following constraint: The only interaction taken into account with the other electrons from the Fermi sea is the Pauli exclusion principle. The lowest energy state is expected if the two electrons have equal but opposite wavevectors $\boldsymbol{k}$ and $-\boldsymbol{k}$, respectively [51]. Thus, a good starting point for the calculation is the following orbital wavefunction

$$\Psi(\boldsymbol{r_1}, \boldsymbol{r_2}) = \sum_{\boldsymbol{k}} g_{\boldsymbol{k}} e^{i\boldsymbol{k}\boldsymbol{r_1}} e^{-i\boldsymbol{k}\boldsymbol{r_2}} \tag{2.4}$$

with $|g_{\boldsymbol{k}}|^2$ the occupation probability of the state $\boldsymbol{k}$. $g_{\boldsymbol{k}}$ is symmetric with respect to $\boldsymbol{k}$. This is obtained by calculating the energy of this state with the above-mentioned constraint. Furthermore, the problem is simplified by setting the phonon-mediated electron-electron interaction constant for $\boldsymbol{k}$-states within an energy window of $\hbar\omega_D$ around the Fermi energy and 0 otherwise. The symmetry of $g_{\boldsymbol{k}}$ yields (consider Eq. 2.4) a symmetric orbital wavefunction with respect to the exchange of the two electrons. Since the total wavefunction (orbital and spin contribution) has to be antisymmetric, the spin part has to be a *singlet* which reads in the Dirac notation as

$$|\Psi_S\rangle \approx (|\uparrow_1\downarrow_2\rangle - |\uparrow_2\downarrow_1\rangle). \tag{2.5}$$

The finding that a Cooper pair is a *spin-singlet* is of great importance for the motivation of the experiment discussed in chapter 6.
In the BCS theory the discussed work from Cooper is extended by letting *all* the electrons from the Fermi sea participate in the formation of Cooper pairs ($\boldsymbol{k}\uparrow, -\boldsymbol{k}\downarrow$) in a connected fashion, reducing thereby the energy of the entire system [49]. The condensation continues until the energy gain for forming an additional Cooper pair reaches zero. Consequently, the ground state for this many-body problem can be quite complicated and is here not further discussed. For a review see for example [49]. A very distinct characteristic of superconductivity emerging from the BCS theory is the appearance of an energy gap Δ in the quasiparticle DOS N_s of the superconductor (see Fig. 2.7a). 2Δ is the *pairing energy*, which can be considered as the excitation energy of the two electrons resulting from breaking up a Cooper pair. It should be noted that in principle the excitations are not simple electrons but

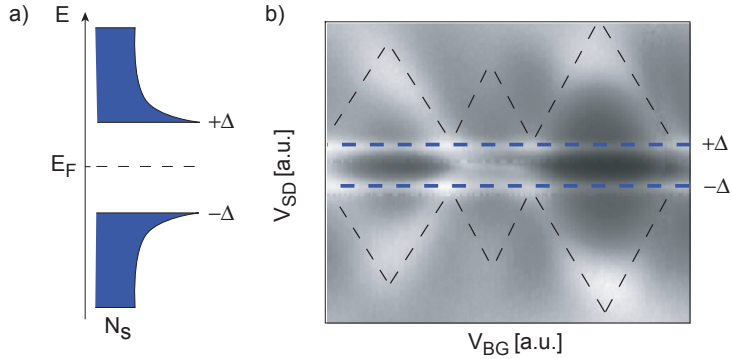

Figure 2.7: *a) The quasiparticle DOS of a superconductor N_s with the characteristic energy gap Δ is shown. b) A $G(V_{SD}, V_{BG})$ measurement of an N-QD-S device is presented where Δ is clearly visible as the onset of quasiparticle tunneling at $V_{SD} = \pm\Delta/e$ (see blue dashed lines).*

quasiparticles, often called *Bogoliubons* (see e.g. [49]). Far from the Fermi energy E_F these quasiparticles have the same characteristics as electrons or holes in the normal metal, giving a similar structure for N_s and the DOS N_n of the normal state. Yet, closer to E_F they differ more, as a direct consequence of the emergence of the superconducting gap Δ. N_s turns out to have the following form:

$$\frac{N_s(E)}{N_n(E_F)} = \begin{cases} \frac{|E-E_F|}{\sqrt{((E-E_F)^2-\Delta^2)}} & \text{for } |E-E_F| > \Delta \\ 0 & \text{for } |E-E_F| < \Delta \end{cases} \tag{2.6}$$

From Eq. 2.6 it is evident that there are no quasiparticle states below $|E - E_F| < \Delta$ and that there is a divergence in N_s for $|E - E_F| = \Delta$. This divergence gives rise to distinct peaks in a $G(V_{SD}, V_{BG})$ measurement at $V_{SD} = \pm\Delta/e$ for a QD contacted with a normal and a superconducting electrode (see Fig. 2.7b). The temperature evolution of the superconducting gap Δ (which is related to the Cooper pair density $N_{CP} \propto \Delta^2$) can also be calculated in the BCS framework and results in [49]

$$\Delta(T) \approx 1.74\Delta(0)\left(1 - \frac{T}{T_c}\right)^{1/2} \tag{2.7}$$

with $\Delta(0) = 1.76 k_B T_c$ and T_c the *critical* temperature where the transition between superconducting and normal state takes place[2]. Although in principle the control over the temperature provides means to tune the system between the S and N state, it is often not the optimal technique to switch off S. Raising the temperature too high would influence the transport characteristics in QD spectroscopy where orbital level spacing and barriers are of similar energies than $k_B T_c$ and coherence plays an important role. However, superconductors have very specific magnetic field behavior: They are perfect diamagnets. This so-called *Meissner-Ochsenfeld effect* [52] has its origin in creation of supercurrents in the superconductor, generating magnetic fields which cancel the external magnetic field. But if the external magnetic field B exceeds a (material dependent) critical field B_c, superconductivity vanishes. Thus, by applying $B > B_c$, the transition between the superconducting and normal state can be achieved without raising the sample temperature.
Within the framework of the BCS theory also an approximate spatial extent of the Cooper pairs can be obtained which results to $\xi_{CP} = \frac{\hbar v_F}{\pi \Delta(0)}$, with v_F being the Fermi velocity [49]. As will be shown in chapter 6 this length scale has an important influence on fabrication details of the studied devices. For completeness it should be noted that the BCS theory explains the absence of electrical resistance in S. The electrons in a Cooper pair have opposite momentum and spin and therefore all of the Cooper pairs have zero total momentum $P = 0$ in thermal equilibrium. They also occupy the same "macroscopic" quantum state Ψ [51]. The mechanism for resistance is electron scattering (which corresponds essentially to a momentum change) on impurities or phonons. Although a current can flow for $P \neq 0$, Cooper pairs can only scatter if the momentum P would change such that enough energy is provided to overcome the pairing energy 2Δ. Thus, currents flow dissipationless in S. From this viewpoint, the above mentioned critical field can be understood better. Higher currents are needed to compensate higher external magnetic fields. This increases P, and at the point where the resulting energy gain is of the order of 2Δ, pair breaking occurs and superconductivity diminishes.
So far, only the general properties of superconductivity have been discussed. However, superconducting electrodes affect transport measurements on S-QD-X (where X = N, F or S) systems (see Fig. 2.7b and chapters 4 through 7) as a result of the *proximity effect*. Crudely spoken, the proximity effect can be viewed as a "leaking of Cooper pairs" into the QD (or simply into a normal conducting material) [53]. Transport in S-X/S-QD-X systems shall be considered in the remaining part of this theory chapter.

[2]For completeness it should be noted that Eq. 2.7 only holds close to T_c.

2.3.2 Andreev processes

A microscopic description of a S-N interface is given by the Bogoliubov-de Gennes equations [54]. However, a detailed analysis of the system within this framework is beyond the scope of this thesis and only an intuitive picture is provided. It is convenient to look at the system from the normal metal side. If an electron with e.g. spin-↑ impinges on the superconductor, it cannot enter S as long as its energy is lower than Δ. The reason is that within the superconducting gap only Cooper pairs exist and only above the gap free states would be available. Also normal reflection is strongly suppressed: At a S-N interface normal reflection requires a momentum change of $2p_F$. A rough estimation of the possible momentum transfer to the interface $\Delta p_{max} = \left(\frac{dU}{dx}\right)\Delta t \approx \frac{\Delta}{\xi}\frac{\xi}{v_F}$ yields that $\Delta p_{max} \ll p_F$ [55]. Andreev found that the electron gets retroreflected as a spin-↑ hole [56]. As a net result a Cooper pair forms in the superconductor and charge and momentum is conserved. This process is called *Andreev reflection* (see Fig. 2.8a process I, where a filled particle corresponds to an electron whereas the empty ones are supposed to be holes). Clearly, considering time-reversal symmetry, also the opposite is possible: an incident hole gets retroreflected as an electron while removing a Cooper pair from the superconductor (process II Fig. 2.8a). This process is the one which can be considered as the leaking of Cooper pairs into the QD[3] which gives rise to the proximity effect. For completeness it should be noted that only in the case of fully transparent barriers Andreev reflections are the only possible mechanism. Blonder *et al.* presented a model (the so-called BTK model) by which transport for arbitrary barrier strength at the N-S interface can be calculated [57], showing that for non-zero barrier strength also normal reflection occurs. However, for simplicity, finite barrier strength is neglected at this point and only Andreev processes are taken into account. Specifically interesting for the experiments presented in parts of this thesis is the transport in N-QD-S-QD-N structures. Here the basic transport processes in such systems is discussed in the simpler N-S-N structure (Fig. 2.8b), while referring to e.g. chapter 6 for the modifications expected if QDs are incorporated. Equivalently, as for standard Andreev reflections, an incident hole from the normal contact N1 with a given spin orientation (e.g. spin-↑) and momentum $\boldsymbol{k}$ impinges at the S interface. An Andreev reflection takes place, thereby removing a Cooper

[3] For a rigorous proof of this statement the interested reader is referred to refs. [53, 54]. There it is shown, by solving the Bogoliubov-de Gennes equation, that the pairing amplitude (being essentially the Cooper pair density N_{CP}) has a finite value in the normal conductor, which is directly proportional to the amplitude of the Andreev reflection. Thus, saying that Cooper pairs leak into the normal conducting region is equivalent to state that the electron and hole from the Andreev process remain phase coherent over a certain length scale [53].

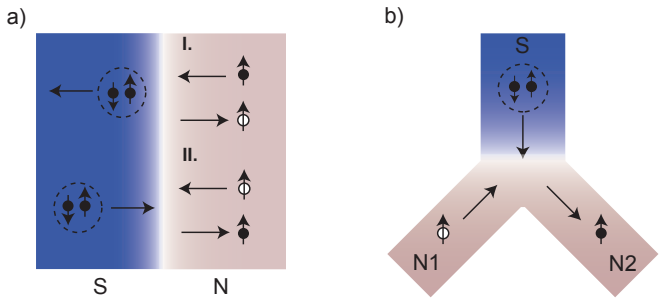

Figure 2.8: *a) Two Andreev reflection processes at a superconducting (S) - normal metal (N) interface are shown. In I, a spin-↑ electron with momentum* $\boldsymbol{k}$ *impinges on S and gets retroreflected as a spin-↑ hole with momentum* $\boldsymbol{k}$*. In order to conserve charge a Cooper pair is created in S. Process II shows the time-reversed process where a Cooper pair leaves S. Process II can be considered as the leaking of Cooper pairs into N giving rise to the proximity effect. b) Non-local Andreev reflection is shown. An S lead is contacted to two N leads. The incoming hole from N1 is Andreev reflected as electron in N2. Thus, considering charge and momentum conservations a Cooper pair is removed from the S condensate.*

pair from the superconductor. But in addition to the retroreflection of an electron with spin-↑ and momentum $\boldsymbol{k}$ as described above, another process might take place. If the spatial extent of the S lead (or more accurately, the distance between N1 & N2) is not exceeding the superconducting coherence length ξ [4], the electron might get reflected into lead N2 [59]. This process is called non-local Andreev reflection or *crossed Andreev reflection* (CAR). If, as presented in Fig. 2.8b, the incoming particle is hole-like, the CAR process removes a Cooper pair from the superconductor and thus CAR can be considered as the *splitting of a Cooper pair* into the two normal contacts N1 and N2. In addition to CAR, another important process in N-S-N structures is elastic cotunneling (EC) [60]. EC is the transport of an electron from N1 to N2 (or vice versa) via a virtual state in S. It is, like AR and CAR, a 2nd order process in the tunnel barrier strength, since it involves two coherent tunneling events. As long as N1 and N2 are on the same potential and bias is applied on S, this process is not of importance. However, if there is a bias between N1 and N2, special care has to be taken to distinguish CAR and EC (see Ref. [60] and chapter 7). For the experiments on CAR in chapter 6, bias is only applied on S and the other contacts were held at the same potential. Therefore, EC can there be neglected.
The means of transport are more delicate if F contacts are coupled to S

[4] In the case of clean BCS superconductors ξ_{CP} is the relevant length scale whereas in the case of "dirty" superconductors $\xi \sim \sqrt{\xi_{CP} l_e}$ has to be used [58].

ones as e.g. in the experiments presented in chapter 5. This is a direct consequence of the difference in the DOS of the spin-↑ and spin-↓ bands of a F lead. As pointed out by de Jong and Beenakker, such differences modify the Andreev reflection probability and hence the conductance across the NS interface [61]. If $N_\uparrow$ is the number of spin-↑ channels and $N_\downarrow$ the number of spin-↓ channels with $N_\uparrow \geq N_\downarrow$, the conductance across the interface is

$$G_{FS} = 4\frac{e^2}{h}N_\downarrow \tag{2.8}$$

Therefore, in the case of fully polarized F leads (i.e. $N_\downarrow = 0$) AR are fully suppressed. Furthermore, in an F-S-F structure, it is possible to tune between the suppression of CAR (both F leads parallel-polarized) and EC (F leads anti-parallel). Eq. 2.8 is also applicable for arbitrary polarization P of the F contact[5]. However, as pointed out e.g. by Grein *et al.* [63], considering only the polarization of the F contacts is insufficient since the influence of the interface can not be neglected. P seems to be at least partially an interface property instead of solely depending on the bulk polarization, as a result of spin-active scattering processes. This means that spin-dependent transmission probabilities do not capture the entire scattering event. In addition the acquisition of spin-dependent phase shifts of the electrons wavefunction need to be considered [63]. Grein *et al.* developed a microscopic model accounting for spin-active scattering by introducing an interface region with a spin-dependent scattering potential whose quantization axis might differ from the bulk ferromagnet one. Although in the simplest case the two spin-quantization axes are parallel, there are many mechanisms (e.g. spin-orbit coupling, magnetic anisotropy, spin relaxation) leading to an extra interface magnetic moment. This is insofar interesting, as it has been shown that inhomogeneities of the magnetization at the S-F boundary can induce a long-range *triplet proximity effect* [64]. This triplet proximity effect results from spin-flip Andreev reflections (SAR), a process where the reflected hole (considering an incoming electron on the S lead) of an Andreev process has the opposite spin orientation[6] as the incoming electron.

[5] Eq. 2.8 is obtained for a diminishing barrier between the S and F contact. Following the concept of the BTK model, the problem of S-F interfaces can also be considered with finite barrier strength [62, 59]

[6] This corresponds to a missing electron with the same spin orientation as the incoming electron.

CHAPTER 3

Basics of sample fabrication and experimental setup

This chapter serves as an introduction to the basic principles needed to produce and measure the devices presented in this thesis. At first, the general fabrication procedures are presented and then the measurement setup is described. However, since all experiments are to a certain extent independent of each other, the corresponding processing steps and measurement setups are presented at the beginning of each chapters. Details of the individual process steps can be found in the appendix B.

3.1 General fabrication steps

In this section the used fabrication methods are introduced. This includes nanowire (NW) deposition, electron beam (e-beam) lithography, metalization, oxide removal and bonding.
Starting point for all devices used in this thesis is a highly doped Si wafer with a 400nm insulating SiO_2 oxide layer (see Fig. 3.1a). The high doping and the oxide barrier enables the usage of the wafers backside as a voltage gate, the so-called backgate. After cleaning, standard e-beam technology (see Fig. 3.1b-f) was used to create the so-called base structure, a pattern consisting of macroscopic contact pads and a grid (see Fig. 3.2) which eases later NW localization. This fabrication process is based on two main steps: e-beam lithography and metalization. To perform the lithography, first polymethylmethacrylat (PMMA) resist is spun on the wafer (Fig. 3.1b). After

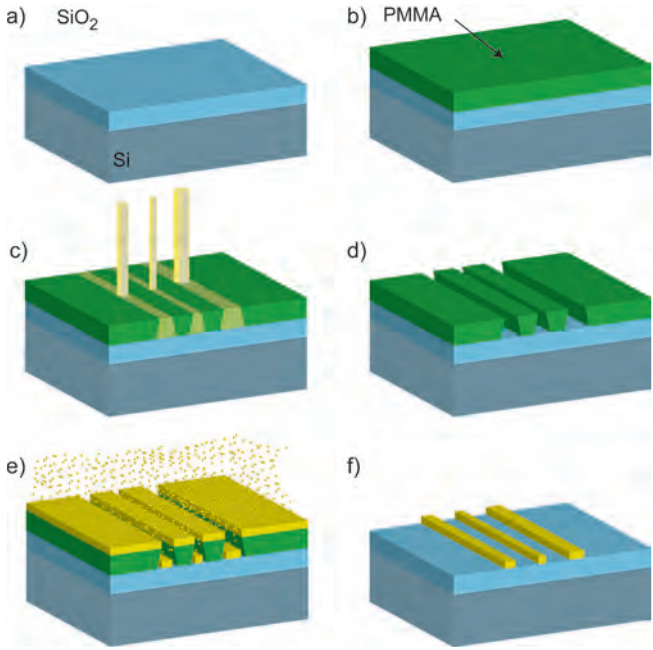

Figure 3.1: *Illustration of a standard e-beam lithography fabrication process. a) Cleaned, highly doped Si wafer with a 400nm insulating SiO_2 oxide layer. b) Wafer coated with PMMA resist. c) Writing the desired structure with a highly focused electron beam (e-beam). d) Obtaining the desired PMMA mask by dissolving the e-beam exposed areas. e) Evaporating the desired metals. f) Removing the remaining PMMA and covering metal.*

hardening the resist (either on a hotplate or in an oven), the desired structure is transferred into the PMMA using a highly focused electron beam (Fig. 3.1c) in a scanning electron microscope (SEM). The e-beam breaks the polymer chains in the exposed areas. In the following development process the broken polymers are dissolved and the designed mask is obtained (Fig. 3.1d). After development and before evaporation, the samples are often exposed to a gentle oxygen plasma in a reactive ion etcher (RIE) to remove unwanted PMMA contamination. In the metalization process, metal is heated (thermally or with an electron beam, depending on the used machine) and deposited onto the structure (Fig. 3.1e). The process is done in a vac-

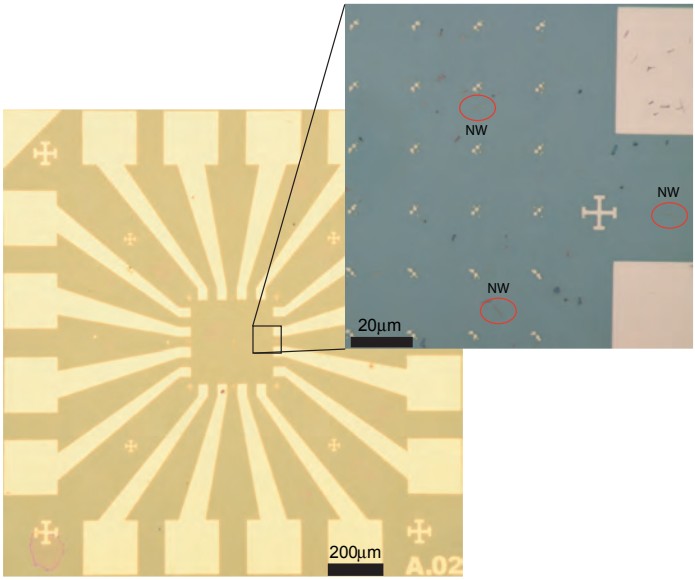

Figure 3.2: *Optical images taken of a base structure with deposited nanowires (NWs, see red circles in close-up). The crosses are used for alignment for e-beam lithography. Small symbols (see close-up) are used to locate the NWs and for fine tuning of the alignment.*

uum chamber with base pressures ranging from 10^{-7} mbar to 10^{-10} mbar, depending on the used evaporation machine. Immersing the wafer after metalization into warm acetone, the so-called lift-off procedure, removes the remaining PMMA and the covering metal. The remaining metal on the wafer has then the shape as designed into the PMMA mask (Fig. 3.1f).
Having obtained the base structure (consisting of Titanium (Ti)/Gold (Au) bilayer where Ti is used to increase the adhesion of the Au which results in a high contrast in a scanning electron microscope (SEM)) high quality molecular-beam epitaxy grown InAs NWs [28] with diameters in the range of $d \simeq 80 - 100\,\text{nm}$ are deposited from an isopropanol (IPA) suspension. Several different deposition methods have been exploited: spin coating, by boiling [65] and evaporation. In the end, letting the IPA-NW solution evaporate on the wafer seemed to be the best approach concerning deposition speed, NW concentration and dirt contaminations on the wafer. To localize the NWs an optical microscope is used (see Fig. 3.2). Even though this

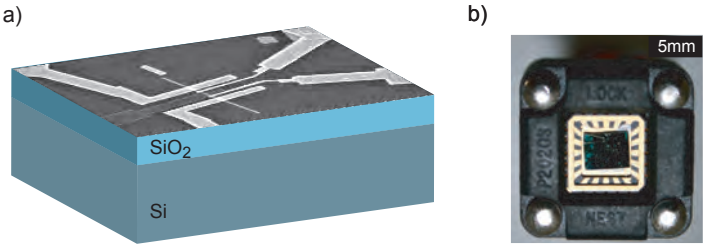

Figure 3.3: *a) Schematic of device fabricated by e-beam lithography, ready to be bonded. The device image is an SEM picture of an actual sample where a NW is contacted by three ohmic contacts (left,middle,right) and two topgates. b) An image of a sample glued with silver epoxy into a chipcarrier. The chipcarrier is mounted into a chipcarrier holder which can easily be soldered to the measurement lines.*

method does not give the same accuracy in choosing NWs concerning their cleanliness as localization with an SEM, it is nevertheless to be preferred due to its non-invasive character. Having transferred the positions of the NWs into a design file (e.g. Elphy or CleWin) the desired structures can be easily created by applying the above described fabrication steps (e.g. e-beam lithography and metalization) in a repetitive manner. Note, that the NWs have a native oxide layer of a few nm thickness [11] which need to be removed before evaporating the desired contact materials. During this work two oxide removal methods were used: sputtering with an argon ion gun (see appendix B) which is installed in the used evaporators or by NH_4S_x passivation [66]. An illustration of a finished device fabricated by the above described fabrication techniques is shown in Fig. 3.3a.
In a final step the processed wafers are glued with silver paint into a chip-carrier which serves as gateway between the *macroscopic* measurement setup and the fabricated *nanostructures* (see Fig. 3.3b). The used chip-carriers have 20 bidirectional contact pads: one side connects to the measurement setup and the other part to the contact pads of the basestructures. This connection between the chip-carrier and the basestructure is achieved by soldering the ends of an Al wire with an ultrasonic bonding-machine to the contact pads of the chip-carrier and the basestructure, respectively. The parameters for this melting process have to be deduced carefully to ensure that during the process the SiO_2 layer does not get damaged since this would lead to leakage currents between the backgate and the device. Distributing some silver-paint on a contact of the chip-carrier allows to use the substrate as

backgate[1]. Attention to proper grounding should be paid during processing, to avoid destruction of the devices due to electrostatic discharge.
At this stage the devices are ready to be mounted into a measurement setup: either a test-box for room temperature checks or directly into a *cryostat* (see below). If measurements at cryogenic temperatures are planned it is preferable to use directly a cryostat to avoid delicate transfers between setups. In the next section the used setups are discussed.

3.2 Experimental setup

The samples are first tested at **room temperature**. For low resistance samples a (quasi) four point setup is the best choice whereas for high resistance samples and especially gate leak tests, voltage biased setups are used. In this manner basic functionality of the devices (e.g. no gate leakages, existence of a gate response, etc.) can be checked. In addition, knowing about the behavior of the device at ambient temperature often sheds light on low temperatures outcomes (e.g. samples with $R_{T=300\mathrm{K}} > 1\mathrm{M}\Omega$ often are fully depleted already at 4K and do not become conducting even by applying high gate voltages).
For the study of quantum dot systems, it is crucial that the temperature T is lower than the the relevant energy scales such as charging energy U, orbital level spacing δE, tunnel coupling Γ, superconducting gap Δ and others (see chapter 2), which are all in the order of meV or smaller in the investigated devices. The samples are therefore built into a **low temperature** measurement setup, if they exhibit promising transport signatures at room temperature. Several systems are available to achieve cryogenic temperatures ranging from 20 mK up to 4.2 K. These so-called cryostats are based on liquid ^{4}He, ^{3}He or ^{4}He/^{3}He mixtures and rely (with the exception of simple *dipstick* setups where the sample is lowered in liquid ^{4}He being at T = 4.2 K) on the same principle: Pumping on the helium mixture leads to evaporation. This costs latent heat which is provided by the system under consideration which is cooled in this process. Most of the presented measurements have been performed in a ^{4}He/^{3}He - cryostat (*dilution refrigerators*). A schematic and the basic principle of operation of such a system can be found e.g. in Ref. [67]. The low temperatures in them are achieved as a consequence of a peculiar feature of the mixture below T = 0.86 K [68]. At this temperature a phase separation takes place: The helium mixture divides into a concentrated ^{3}He-rich and a diluted ^{3}He-poor phase (therefore the name *dilution refrigerator*). Pumping on the ^{3}He-poor phase causes the

[1] To ensure good contact to the highly-doped Si part of the wafer, it is recommended to scratch the side of latter prior to this process to remove a possible oxide layer.

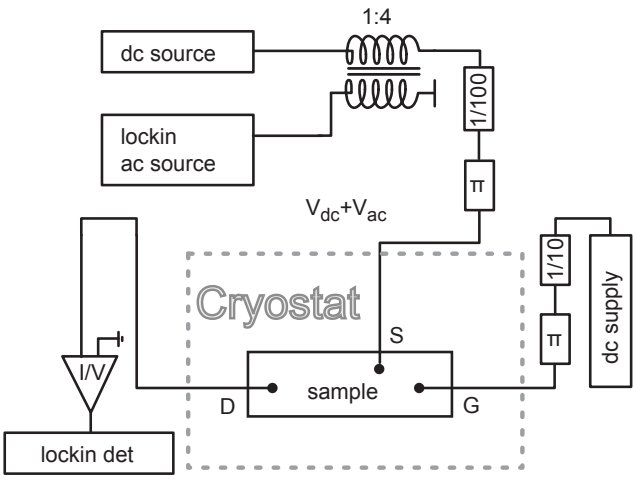

Figure 3.4: *Schematic of the basic measurement setup. Lock-in measurement techniques are applied to measure the differential conductance G. The source (S) contact is biased by both a dc and ac voltage. The dc voltage is used to explore the non-linear differential conductance of the sample. The voltages are divided as close to the sample as possible (i.e. at the top of the cryostat) to obtain a better signal to noise ratio. The used resistances for the voltage divider on the source and gate contacts (S,G) are variable and chosen according to the measurement. The gate voltage (V_G) is representative for all the gate voltages applied (e.g. backgate and topgates). At the input of the source and gate contacts π-filters are installed (see main text) and at cryogenic temperatures further filter stages are employed (not shown). The gain of the I/V converter on the drain (D) contact is chosen according to the measurements performed.*

transfer of ^{3}He from the ^{3}He-rich phase into the ^{3}He-poor phase yielding cooling of the system due to the needed "latent heat" of this process. Due to the significant vapor pressure of ^{4}He/^{3}He mixtures even at T→0 the system can be cooled to temperatures in the millikelvin regime. This process happens at a very specific location within the dilution refrigerator to which the sample is well coupled thermally. However, it is important to note, that even though the base temperatures of the cryostat may reach values around 20 mK, the effective electron temperature T_{el} is usually significantly higher ($T_{el} \geq 100$ mK). The reason is insufficient precooling of the connecting cables or heating due to electromagnetic radiation. Thus, to keep T_{el} sufficiently low, good thermal anchoring of the measurement lines and strong filtering

of high frequency radiation is essential. In the used dilution refrigerators several filtering and radiation shield stages are employed. One protection mechanism is to cover the sample by a Faraday-cage and install radiation baffles along the insert. Furthermore, at low temperatures so-called *tape-worm* filers [69] are installed which consist of twisted wire pairs which are packed into Cu foil. This forms an RLC element which acts as low-pass filter attenuating high frequency radiation by making use of the skin-effect. At room temperature, commercial π-filters (LC circuit elements) are installed at most measurement lines (specifications can be found in [70]).
Since the measured devices can exhibit resistances up to several megohms, voltage biasing is the natural choice to explore the transport characteristics. It is done by measuring the differential conductance $G = dI/dV$ through the samples, normally as a function of gate voltages V_G and/or a dc bias voltage V_{dc}. For this, an ac signal from a *Stanford SR830* lock-in source is applied on the device and the generated ac current is measured by converting it with an home built I/V converter[2] to a voltage which can be detected with the lock-in amplifier. As shown in the corresponding measurement setup (Fig. 3.4[3]) the ac signal is imposed on a tunable dc voltage from a *HP 3245A* or *YK 7651* using a transformer, to measure also the non-linear differential conductance. The use of lock-in amplifiers allows to measure the signal at a chosen frequency and eliminates spurious signals appearing at other frequencies. The chosen ac excitation was kept low $eV_{ac} \sim k_BT < k_BT_{el}$ as not to spoil the effect of the cryogenic temperatures. Furthermore, it allows to assess directly the differential conductance. A typical AC voltage of $V_{ac} = 5\ \mu eV$ is chosen at base temperatures of 20 mK. To have a better signal to noise ratio, the voltages from the sources are only divided to the desired value close to the cryostat. The noise level could be further minimized by keeping the I/V converters as close as possible to the measurement box and the elimination of ground-loops. *HP 3245A* and *YK 7651* voltage sources were used to apply dc gate voltages. All the ingoing signals (S,G in Fig. 3.4) are filtered by the above described π-filters. Via GPIB buses the electronics were controlled and read-out by LabView programs installed on a nearby computer.

[2] The gain of the I/V converters are chosen depending on the measurements. For most purposes a gain of 10^7 V/A was chosen (see the corresponding chapters for details).
[3] It should be noted that only the basic principle is shown and deviations from this scheme for specific measurements are described later.

CHAPTER 4

Giant g-factor fluctuations in InAs nanowires quantum dots

In this chapter the g-factor of discrete electron states in InAs nanowire based quantum dots is studied. It is shown that the g-factor strongly depends on the orbital states as a result of the strong spin-orbit interaction in InAs NWs. Moreover, even within a single charge state, gate voltage dependence of the g-value is observed. The g-factor is insofar of importance as it is the key parameter for the control and the manipulation of spin information at a single electron level. This has e.g. been recently exploited in individually addressable qubits realized in an InAs nanowire [7].
First the device fabrication and measurement setup are presented. Afterwards the measurements characterizing the device are shown, followed by the main results. The discussion and outlook of this experiment are at the end of this chapter. The content of this chaper has been also published elsewhere in a similar form [71].

4.1 Fabrication and measurement setup

An SEM image of an investigated device is shown in Fig. 4.1. After dispersing the high quality InAs NWs [28] on a highly doped Si substrate with 400 nm insulating SiO_2 cap layer and the predefined basestructure they are located with the help of an SEM. In repeating standard e-beam lithography procedures, Ohmic contacts for transport measurements (S,D) and a top gate electrode (TG) for local gating (see Fig. 4.1) are fabricated. The

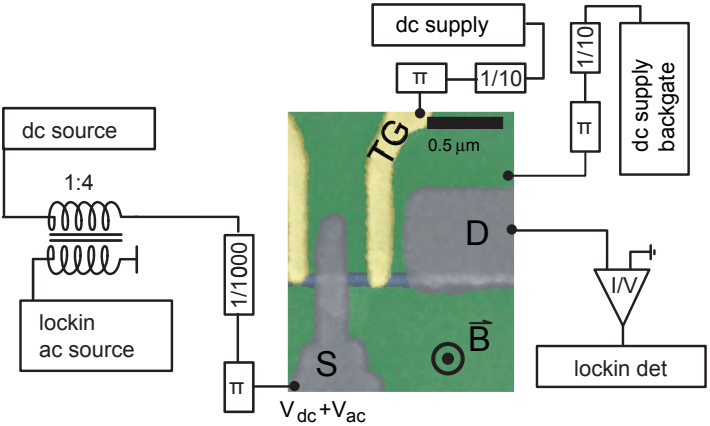

Figure 4.1: *Measurement schematic and SEM picture of the device: The quantum dot forms in the NW segment between the two Ti/Al Ohmic contacts (S,D). A Ti/Au topgate (TG) is deposited on the NW between the Ohmic contacts. The nanowire (blue) has a diameter of* 80 *nm.*

Ti/Au (10/100 nm) TG electrode is isolated from the nanowire by the native surface oxide layer [72]. Before the evaporation of the Ti/Al (10/100 nm) Ohmic contacts this oxide layer was removed by gentle argon sputtering. The transport measurements were performed using standard lock-in techniques in a dilution refrigerator at a base temperature of $35 - 45$ mK. A magnetic field perpendicular to the wafer plane could be applied. The ac excitation was $V_{ac} = 5\ \mu$V and the I/V converter had a gain of 10^7 V/A. In addition to the voltage source for the backgate a second voltage source was attached, to apply a topgate voltage on the device.

4.2 Device characterization

The electron density of InAs nanowires can be strongly varied by applying a voltage on the backgate electrode. Based on the backgate dependence the nanowires have n-type charge carriers (applying negative voltages lead to depletion). When the backgate potential is decreased, barriers are generated at the contacting source and drain electrodes, and a quantum dot forms in the middle of the wire segment [28, 30]. In the presented device architecture the topgate provides additional means to modify the shape of

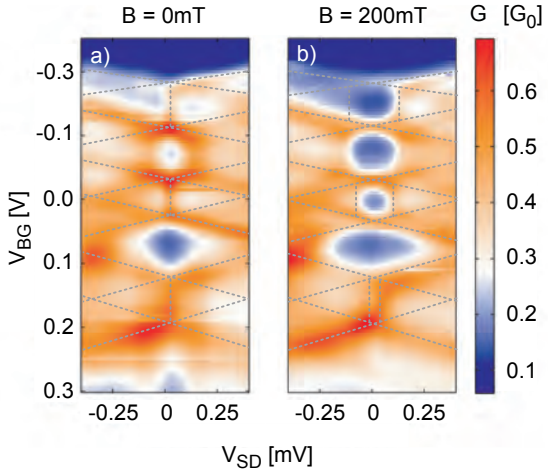

Figure 4.2: *Colorscale plots of the differential conductance vs. backgate and source drain voltage measured at $V_{tg} = 0.07$ V. The stability diagram at $B = 0$ T (a) clearly shows the even/odd filling of the quantum dot. There is a Kondo ridge at zero bias voltage in every other Coulomb diamond (dotted lines). At $B = 200$ mT (b) the Kondo ridges split up, however differently for each Kondo state.*

the confinement potential of the QD besides the backgate.
A typical stability diagram measured on such a QD is plotted in Fig. 4.2a for a constant $V_{tg} = 0.07$ V. Since the QD is in a rather open state (intermediate coupling) the differential conductance $G = dI/dV$ exceeds the value of ~ 0.7 G_0 ($G_0 = 2e^2/h$) and the border of the Coulomb blockade diamonds are rather faint. From the size of the diamonds (see the dotted lines) the estimated charging energy is in the range of $0.5 - 1$ meV, which is consistent with the length of the nanowire segment of 400 nm [28].
The subsequent Coulomb diamonds have alternating sizes, a smaller diamond is followed by a larger one and then a smaller one again. In the smaller diamonds the differential conductance shows a pronounced increase at zero source drain bias voltage (see dotted lines at $V_{SD} = 0$). This type of even-odd symmetry of the stability diagram is a strong indication of the spin$-1/2$ Kondo effect [43], which was analyzed in InAs nanowire QDs by T. S. Jespersen *et al.* in detail [28]. If the QD contains an odd number of electrons the highest occupied orbital is filled only by a single electron. Due to the strong coupling to the leads the spin of this unpaired electron is screened by the spin of electrons in the lead forming a many-body state, the so-called Kondo cloud, which gives rise to an enhancement of conductance

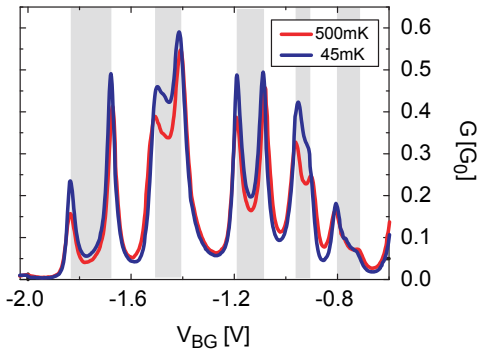

Figure 4.3: *Differential conductance versus backgate voltage at $T = 45\,mK$ and $500\,mK$. The conductance increases inside every second Coulomb diamond for decreasing temperature (gray regions) in agreement with Kondo physics. Measured at $V_{tg} = 0.06\ V$ and $V_{SD} = 0\,mV$.*

at zero bias voltage. Although zero-bias anomalies in every second charge state are a strong indication for the presence of the spin$-1/2$ Kondo effect, further tests should be performed to confirm this assumption.
Fig. 4.2b shows the differential conductance as a function of backgate and source/drain voltage for the same topgate voltage ($V_{tg} = 0.07$ V) as in Fig. 4.2a at a magnetic field of $B = 200$ mT. It is evident that the zero-bias peaks in the odd charge states split up as expected for Kondo resonances in magnetic field. To gain further confidence that these features are Kondo signatures, one can look at the temperature dependence of these states. In a QD without Kondo correlations (or in even charge states in general) Coulomb blockade is more pronounced for lower temperatures since additional transport channels (e.g. cotunneling processes) become blocked. Therefore, the conductance between Coulomb peaks decreases by lowering the temperature. However, in a Kondo state, the conductance increases with decreasing temperatures as a result of the Kondo effect [43]. The temperature dependence of the slice of the stability diagram at $V_{SD} = 0$ V shown in Fig. 4.3a is consistent with the described behavior. Inside the charge states with even number of electrons the differential conductance decreases when cooling down the sample, while an increase is observed in charge states where Kondo correlations are present (gray regions in Fig. 4.3a). Thus, the observed zero-bias anomaly can be attributed with confidence to the spin-1/2 Kondo effect.

4.3 Observation of g-fator fluctuations: main results

The magnetic field dependence of the spin$-1/2$ Kondo is behaving according to the Zeeman-splitting ($\Delta V_{Kondo} = 2g\mu_B B/e$) and is thus proportional to the effective g-factor of the highest discrete electron state occupied with an unpaired electron [48, 44]. The other terms in the energy dependence are the Bohr magnetron μ_B, the electron charge e and the external magnetic field B. Thus, one can extract the $|g|$ values by investigating the magnetic field splitting of the spin-1/2 Kondo effect. There are different methods in the literature for the precise determination of the $|g|$ value from the Kondo splitting. In Ref. [48, 44] the positions of the maximums of the split Kondo peak were used, which yields a slight overestimation (few percent) based on later studies [73]. Here $|g|$ is determined from the magnetic field dependence of the two inflection points [74], which provides $\sim 5\%$ smaller values. A typical analysis of the magnetic field dependence of a zero bias ridge is shown in Fig. 4.4. The zero bias anomaly peak (black arrow) splits up linearly with magnetic field in agreement with the Kondo physics (see also inset). Note, that the two side peaks (gray arrows) are related to the superconducting electrodes and they are completely suppressed by a field of 50 mT. For the analysis of the g-factor they are not of importance and are at this point not

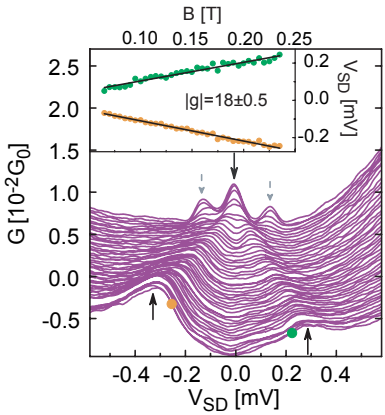

Figure 4.4: *Differential conductance vs. source drain voltage at different perpendicular magnetic field values $B = 0, 5, 10, ..., 240$ mT (back to front). Measured at $V_{BG} = -2.64$ V and $V_{tg} = 0.08$ V. The curves are shifted for clarity. Note, the two side peaks (gray arrows) are superconducting features induced by the Ti/Al electrodes. (inset): The position of the inflection points of the $G(V_{SD})$ curves from the main panel (orange and green dots) as a function of the magnetic field. Linear fit (line) with the extracted $|g|$-factor.*

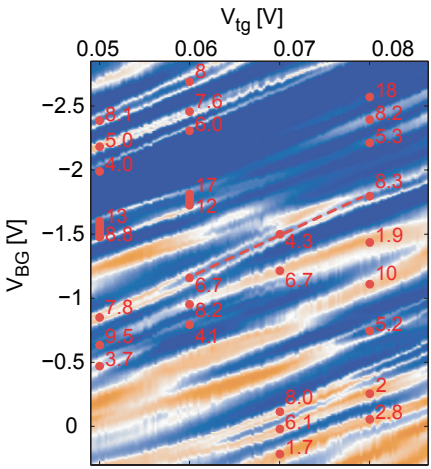

Figure 4.5: *Summary of the evaluated $|g|$ values. Colorscale plot of the differential conductance vs. backgate voltage and TG voltages (at $V_{SD} = 0$ V and $B = 0$ T) with the absolute value of the g-factors determined from the magnetic field splitting of the Kondo ridges.*

further discussed. The position of the inflection points (see orange and green points for the highest B field in the main panel of Fig. 4.4) are plotted as a function of the B field in the inset of Fig. 4.4 and their difference is fitted by $\Delta V_{Kondo} = 2|g|\mu_B B/e$.

In the following it is analyzed how the effective g-factor of individual discrete electron states behave when the confinement potential of the QD is changed with the gate electrodes. The stability diagram measured at $B = 200$ mT in Fig. 4.2b shows that the magnetic field splitting of the Kondo ridge in subsequent odd Coulomb diamonds strongly varies between different states. The extracted $|g|$ values of these three neighboring electron states are ~ 8, 6.1 and 1.7. Thus adding only two extra electron on the QD can change the g-factor by over 100%. Fig. 4.5 summarizes the evaluated $|g|$ values. The colorscale plot shows $G(V_{tg}, V_{BG})$. Higher conductance regions appear along diagonal lines since the backgate voltage induced shift of the electron levels of the QD is compensated by opposite tuning of the topgate. At four different TG voltages the V_{BG} voltage of the diamonds where Kondo ridges were observed are plotted by red circles. The neighboring numbers are the absolute value of the g-factors evaluated similarly as in Fig. 4.4. $|g|$ does not show a systematic behavior as a function of the backgate voltage, and

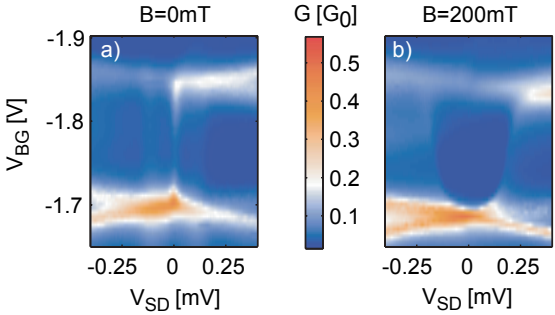

Figure 4.6: *(a,b) Stability diagram of a Coulomb diamond with a Kondo zero bias anomaly, where the magnetic field induced splitting is changing inside the diamond. Measured at* $V_{tg} = 0.6$ *V.*

one finds values up to 18, which exceeds the bulk value of $|g| = 14.7$.
By modifying the backgate and topgate voltage simultaneously along the Coulomb blockaded regions (blue stripes) the confinement potential of the QD changes while its charge state is preserved. Such a tuning of the gate voltages can also lead to marked g-factor variations. For instance along the red dotted line in Fig. 4.5 the $|g|$ varies almost by a factor two, while the number of electrons is kept fixed on the QD. Furthermore, in some of the Coulomb diamonds the magnetic field splitting of the Kondo ridge is clearly *not* constant over backgate voltage. In Fig. 4.6a,b a differential conductance measurement of a odd occupied charge state with a Kondo resonance is shown for $B = 0$ mT (a) and $B = 200$ mT (b). As it is clearly visible in Fig. 4.6b the splitting of the Kondo ridge varies more than 30% between the two sides of the diamond at $B = 200$ mT. Thus changes of the g-factor are visible even inside single charge states. Such a gate tunability of the g-factor of a single electron state provides an efficient way for selective addressing of electron spins.

4.4 Discussion

The experimental results show that the g-factors can vary over an order of magnitude for neighboring discrete electron states, which highly exceeds most previous observations in semiconductor based quantum dots [75, 76]. Only in a more recent study on InSb nanowires [77] similar g-factor fluctuations as presented in this chapter have been reported. In addition, strong gate tunability of the g value of individual charge states is also demonstrated

(see Fig. 4.6b).
In the presented data the g-factors have been extracted from the magnetic field evolution of the Kondo resonances. Therefore, it seems evident to check for correlations between the Kondo effect and the observed strong fluctuations in the $|g|$ value. The strength of a Kondo state is determined by the Kondo temperature T_K, the characteristic energy scale for the Kondo singlet state [43]. Therefore, the relation between the observed $|g|$ values and T_K estimated from the full width at half maximum (FWHM) of the Kondo ridges was investigated. As it is shown in Fig. 4.7a, no correlation was found between $|g|$ and T_K. Thus, it can be concluded that the level-to-level fluctuation of the g-factor is not related to Kondo physics.
The large g-factor ($g = -14.7$) of bulk InAs (zincblende (ZB) crytal structure) is due to the presence of strong spin-orbit coupling and the contribution of the orbital degree of freedom. It should be noted that the NWs used in this experiment have most likely wurtzite (WZ) crystal structure [11, 4]. Only recently band properties of InAs WZ structure have been become available. g-factors of this crystal structure are not available so far and there might be deviations from the bulk ZB g-factor due to the different crystal structure. In addition, confinement of the electrons also plays a role. If the electrons are hold in a small constriction the large $|g|$ value can decrease even down to the free electron value of 2 because of the quenching of the angular momentum [78, 79]. This phenomenon was reported by Björk *et al.* for InAs nanowires [16]. They studied quantum dots formed between two (few nanometer thin) InP tunnel barriers. In contrast to the here presented work,

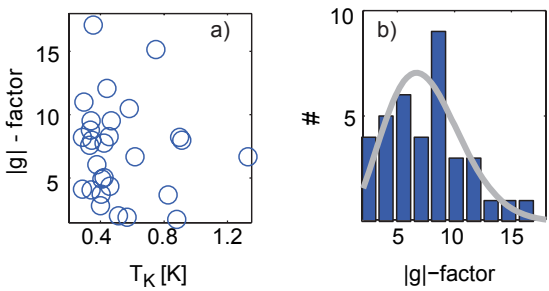

Figure 4.7: *a) Extracted $|g|$ values vs. estimated Kondo temperature from the full width at half maximum of the Kondo zero bias anomaly at $B = 0$ T (FWHM=$2k_BT_K/e$). b) Distribution of the evaluated $|g|$-factors (bar) and the expected probability distribution from Eq. 4.1 (line).*

the $|g|$ values were extracted from the excited state spectrum of the dots. Yet, as shown by Ref. [77], obtaining the g-factor from excited state spectrum gives in good approximation the same result as extracting the values from the magnetic field evolution of Kondo peaks. When Björk *et al.* decreased the distance between the barriers to 8 nm the $|g|$ value decreased down to $\simeq 2$. However, they did not observe measurable changes in $|g|$ varying the number of electrons on the quantum dot. In comparison to their work, the size of the QD presented in this chapter is relative large, $L \simeq 300 - 350$ nm and the occupation number is also significantly higher. Therefore, a considerable orbital angular momentum is preserved. This is supported by the average value of the measured g-factors of $\langle |g| \rangle = 7.4 \pm 3.6$. The elastic mean free path and spin orbit length ($l_e \approx 80$ nm, $l_{SO} \approx 125$ nm [80]) are significantly smaller than the size of the QD thus the electrons cover diffusive trajectories and several SO scattering events are expected to take place in the QD. Since the QD has a rather asymmetric form induced by the high aspect ratio and the topgate/backgate defined geometry the orbital contribution and the SO correction of a particular electron state are expected to vary. This is in agreement with the recently shown measurements on InSb nanowires by Nilsson *et al.* [77]. Their NWs are the only other semiconducting nanostructures, besides the here presented InAs NW QDs, where giant g-factor fluctuations have been reported. InSb has a even larger bulk g value ($|g| = 50$) than InAs and therefore the system is even more sensitive to magnetic fields. Taking advantage of this magnetic field sensitivity, they have analyzed the g-factor variation of different charge states with four different methods (magnetic field evolution of zero-bias Coulomb peaks, magnetic field evolution of differential conductance at finite bias, stability diagram a finite magnetic field and spin-1/2 Kondo splitting in magnetic field). A strong level dependence was observed with $|g|$ varying between 20 and 70. Their argumentation why the g-factors are not strongly suppressed compared to the bulk value as e.g. in Ref. [16], follows the one mentioned in the above paragraph: Their rather large QD size ($L \simeq 250$ nm) and NW diameter ($d \simeq 70$ nm) preserves a considerable contribution to the g value from the orbital motion of the electrons. The level-to-level fluctuations they attribute to the presence of spin-orbit interaction.

Even though in semiconductor nanostructures these g-factor fluctuations are surprising, in metallic nanoparticle based QDs in the presence of spin-orbit interaction level dependent g values were found already some time ago [81]. In that work, g-factors of discrete electron levels for e.g. silver nanoparticles (diameter of $\simeq 5 - 10$ nm) vary between $0.25 - 1$. The variation is explained by the fact that the g-factor of a particular state gets contribution from the SO matrix elements with all the other discrete levels. Since the precise nature of the wave function of electron states is fluctuating and the

level spacing is also varying the SO induced correction exhibits fluctuation for different levels [81]. The observed fluctuations in Ref. [81] agree quantitatively with random matrix theory (RMT) calculations [82, 83], which describe the SO interaction with the parameter $\lambda = \sqrt{(\hbar\pi/\tau_{SO}\delta)}$ (τ_{SO} and δ are the SO scattering time and the level spacing, respectively). For the here presented InAs NW measurements a rough estimation of SO strength is $\lambda \approx 0.4$ based on $\delta \approx 0.1$ meV and the bulk value $\tau_{SO} \approx 100$ ps [84]. This is close to the range of $\lambda \approx 0.7-10$, where g fluctuation was observed in metallic grains. The RMT provides an analytic expression for the distribution of the g-factor at the strong SO coupling regime:

$$P(g) = 3\left(\frac{6}{\pi}\right)^{1/2} \frac{g^2}{\langle g^2\rangle^{3/2}} \exp\left(-\frac{3g^2}{2\langle g^2\rangle}\right), \tag{4.1}$$

where $\langle g^2\rangle$ is the mean square value of the distribution. For the experimental distribution function of $|g|$ (see bar graph in Fig. 4.7b) $\langle g^2\rangle = 67$. Using this mean square value the RMT predicted distribution is plotted by a line graph in Fig. 4.7b. Probably not being in the strong SO regime, the distribution functions show nevertheless a reasonably good agreement with no adjustable parameters. Based on the theory $\langle g^2\rangle = 3/\lambda + \langle g_o^2\rangle$, where the first term is the spin contribution and $\langle g_o^2\rangle$ is the orbital part. In the case of metallic nanoparticles the spin contribution dominates the g-factor. In contrast, for InAs QDs the orbital part is expected to provide the main contribution due to the small effective mass and relative large dot size. This is consistent with the large broadening of the distribution of $|g|$. However, a proper estimate of the spin and orbital contribution of the g-factor for the semiconductor NW geometry would require the extension of the model.
Based on the previous comparison, the following explanation of the observed fluctuation in the InAs NW based QDs is proposed: Since the precise nature of the wavefunction of the discrete electron states is random, each state gets a different orbital contribution and spin-orbit correction to its g-factor. In other words the strongly varying $|g|$ value is a manifestation of the general mesoscopic fluctuation phenomenon.

4.5 Summary and outlook

The g-factor of discrete electron states of InAs nanowire based quantum dots has been analyzed. The $|g|$ values were evaluated from the magnetic field splitting of zero bias Kondo ridge. The extracted values show an unexpected large level-to-level fluctuation. Furthermore, the g-factor can be tuned up to a factor of two for the same charge state by gate electrodes. A possible explanation is that the random nature of the wavefunction of the discrete

electron states generates different orbital contribution and spin-orbit corrections to their g-factors.
The observed gate tunability of the g-factor of confined electrons can be used to drive the spin in and out of resonance in a static magnetic field which could provide a fast and selective manipulation of quantum dot based spin qubit. In a similar approach, g-factor variation between the two QDs of a double quantum dot system realized in an InAs NW has been used, to address the spin qubit of each dot separately [7].
As a follow-up to the experiments presented here, measuring the g-tensor of discrete electron levels of InAs NW QDs is proposed. This could be realized if a vector magnet in the measurement setup is available. Knowledge about the anisotropy of $|g|$ could give insights into the wavefunction and confinement potential of InAs NW QDs and lead to a better understanding of these NW systems.

CHAPTER 5

InAs nanowire quantum dots with ferromagnetic and superconducting leads

In the previous chapter a phenomenon intrinsic to InAs NW QDs has been discussed. The observed level dependence of the g-factors has its origin in the large spin-orbit interaction in InAs NWs, an interaction which is fundamental for the rich field of spin physics. An important aspect of it is the study of devices connected to spin-sensitive contacts, such as ferromagnets (F) or superconductors (S). S/F heterostructures have already been investigated extensively in the past. Due to the different spin ordering of an s-wave superconductor and a ferromagnet, a large variety of interesting phenomena have been observed at an S/F interface: probing the spin polarization by Andreev reflection [62], π-junction behavior [85, 86], ferromagnetically induced triplet superconductivity [87] or ferromagnetically assisted Cooper pair splitting [88].
In this chapter the work is centered around *novel* S/F hybrid devices where an InAs quantum dot is fabricated between an S and an F lead. First, the fabrication and the measurement setup are presented, followed by a short theory part, interpreting the effects induced by the F lead. In the subsequent sections the influence of the F and S lead on the electric transport characteristics are shown and discussed. The entire chapter is closed by a summary and outlook. Please note that parts of this chapter have been published similarly in Ref. [26].

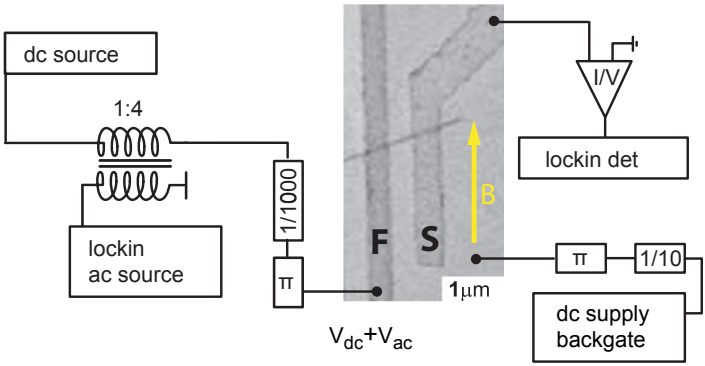

Figure 5.1: *SEM picture of a device and schematic of the measurement electronics. The right lead is a Ti/Al bilayer superconductor, while the left longer one is a Ni/Co/Pd trilayer ferromagnet. The B field is applied parallel to the F stripe.*

5.1 Fabrication and measurement setup

The devices for the measurements shown in this chapter are fabricated as follows: The NWs are dissolved in IPA and deposited on doped Si substrates with 400 nm insulating SiO_2. Afterwards, Ohmic contacts at spacings of $300-500$ nm are fabricated by standard e-beam lithography technique. The procedure is done twice: once for the ferromagnetic Ni(15 nm)/ Co(80 nm)/ Pd(10 nm) contact and once for the superconducting Ti(10 nm)/Al(110 nm) contact. To ensure good contacts, the native oxide was removed by gentle in-situ argon sputtering immediately before the metal evaporation (for detailed parameters see appendix B). Measurements are performed with standard lock-in techniques (*ac* excitation = 4 μV, I/V converter gain 10^7) at a temperature of 25 mK. In agreement with other measurements presented in this thesis, QDs form between these contacts and can be tuned by the voltage applied on the backgate, V_{BG}. An external magnetic field (B) is applied parallel to the F contact (see Fig. 5.1). B allows to switch the orientation of the magnetization of the F stripe and to control the size of the superconducting gap. To magnetize the F lead the external field is ramped to $B = +300$ mT and then back to $B = 0$ mT before measuring. Otherwise, the polarization of the F lead could be different between subsequent mea-

surements and render the interpretation of the data very difficult (see also section 5.3).

5.2 Ferromagnetic proximity effect: theory

The differential conductance $G = dI/dV$ of the devices is analyzed in the intermediate coupling regime where the manybody spin-1/2 Kondo effect [43] can prevail (see chapter 2 & 4 for more details). Following the theoretical proposals [89, 90, 91, 92] and experimental verifications [93, 94, 95], it is straightforward to understand why the Kondo regime is of highest interest: As pointed out by Utsumi *et al.* [96], if an electron in a QD coupled to F contacts has the same spin orientation than the majority of the tunneling electrons from F, charge fluctuations between the lead and the QD are more probable than if the QD spin orientation is equal to the one of the minority tunneling electrons. Consequently, in the presence of F leads the spin-$\uparrow$ and $\downarrow$ energy levels of the QD can split by an exchange energy, E_{ex} due to the hybridization between the QD states and the F lead (see Fig. 5.2a). This proximity ferromagnetism has the same effect on the QD as the presence of an external magnetic field, B. Thus, the exchange splitting is often characterized by the so-called local magnetic exchange field (B_{ex}) in the literature, where $E_{ex} = g\mu_B B_{ex}$. The Kondo resonances split into a doublet in an external magnetic field according to the Zeeman energy $E_{\downarrow/\uparrow} = \mp 1/2 g\mu_B B$, thus being a sensitive tool to investigate B_{ex}.
Pasupathy *et al.* [93] were the first to show experimentally the predicted lifting of the QD spin degeneracy due to spin-dependent energy renormalization. They observed a splitting of the Kondo resonances in electromigrated Ni gaps holding a C60 molecule, when the magnetization of the Ni contacts was parallel to each other. They were able to restore the Kondo resonance by applying an appropriate magnetic field that aligns the magnetization of the leads antiparallel. More recently, Hauptmann *et al.* [95] have exploited the Kondo peak as a "magnifying glass" to analyze the magnetic exchange field in gateable carbon nanotubes (CNT) QDs. With their Ni contacted CNTs they reproduced the work by Pasupathy *et al.* and observed an other intriguing effect, proposed by Martinek *et al.* [91]: B_{ex} can be gate dependent and even change sign in a single charge state. Hence, *electrically* controlled reversal of the spin occupation of the QD can be achieved which is highly desirable for example in spintronic applications. In the subsequent part of this section the relevant theoretical background to understand the effects of the ferromagnetic leads are discussed.
To better understand the origin of the ferromagnetic exchange effect it is helpful to look at the energy diagram of the investigated devices (see

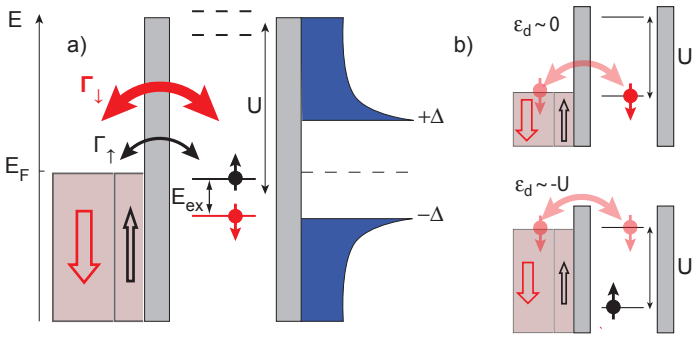

Figure 5.2: *a) Schematic view of the F-QD-S system. The spin degeneracy on the QD is lifted by an exchange splitting induced by the ferromagnetic proximity effect. b) Due to the spin-polarized charge fluctuations, the spin ground state of the QD is opposite when the QD occupation fluctuates between 1 and 0 ($\epsilon_d \approx 0$) or 1 and 2 ($\epsilon_d \approx -U$).*

Fig. 5.2a). Between the F contact (left side) and S contact (right side) the discrete energy levels of the QD are shown. The S lead is represented by the BCS density of states (DOS) with its energy gap Δ. Electron-electron interactions in ferromagnetic materials give rise to a magnetic ordering and thus result in a spin dependent DOS, $\rho_\uparrow(\omega) \neq \rho_\downarrow(\omega)$ [89]. Martinek *et al.* [91] have compared elaborate numerical renormalization group analysis for general types of DOS with simple flat band DOS ($\rho_\sigma(\omega) = \rho_\sigma$, σ being the spin index) calculations. Results show that a flat band DOS captures the relevant physics quite accurately. Because of the difference of the spin-↑ and spin-↓ electron density of the F lead at the Fermi energy and by the tunneling matrix elements of these electrons (e.g. in Ni, two bands couple with opposite spin-imbalance and different tunneling matrix elements to the QD at E_F [97]), the F lead induces an asymmetry of the tunnel coupling (Γ) of spin-↑ and spin-↓ electrons to the QD (red and black bidirectional arrows in Fig. 5.2a). This asymmetry of the couplings is described by the tunneling spin polarization $P = (\Gamma_\uparrow - \Gamma_\downarrow)/(\Gamma_\downarrow + \Gamma_\uparrow)$. By hybridization, the spin dependent tunnel coupling generates a spin imbalance on the QD, described as an exchange field B_{ex}. The ferromagnetic proximity effect and the related ground state transition on the QD can be described in a simple model, using perturbative scaling analysis for a flat bandstructure with spin-dependent tunneling rates and including finite Stoner splitting in the

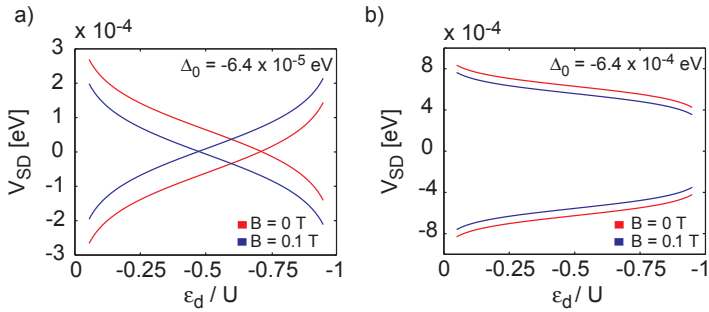

Figure 5.3: *Eq. 5.1 is used to plot the exchange-split Kondo resonances for two different regimes. a) As long as Δ_0 is small enough, a crossing of the split Kondo resonances is observed. This implies a sign-change of B_{ex} leading to a transition of the spin-ground state in the QD. The blue curves show the behavior at finite magnetic field. b) If Δ_0 is the dominant term, no crossing of the Kondo ridges is seen. B_{ex} remains roughly constant within the charge state.*

leads. In this regime an analytical formula for the energy splitting of the spin-↑ and the spin-↓ is given by [91]:

$$\delta_{ex} = g\mu_B B + \Delta_0 + (P\Gamma/\pi) ln(|\epsilon_d|/|U + \epsilon_d|). \tag{5.1}$$

Here P is as defined earlier, Γ is the total coupling to the F lead ($\Gamma = \Gamma_\uparrow + \Gamma_\downarrow$), U the charging energy of the QD and ϵ_d the level position of the QD, tunable by V_{BG}. $g\mu_B B$ is the Zeeman splitting due to an external magnetic field, Δ_0 is a Stoner splitting induced shift, which might also contain contributions from spin-dependent interfacial phase shifts induced by reflection of the dot electrons at the F interface [98]. Note, that δ_{ex} for $B = 0$ is equal to $E_{ex} = g\mu_B B_{ex}$. In Ref. [91] an electrically controlled spin ground state reversal has been predicted. Based on Eq. 5.1 the spin ground state of the QD is different for ϵ_d close to 0 and ϵ_d close to $-U$, if Δ_0 or the Zeeman term are not too big. This can be explained by the charge fluctuations between the QD and the F lead (see Fig. 5.2b). Electrons with majority tunneling spin orientation dominate the charge fluctuations. Thus, when the QD occupation fluctuates between 1 and 0 ($\epsilon_d \approx 0$), the majority tunneling spin preferably occupies the QD. However, when the occupation fluctuates between 1 and 2 ($\epsilon_d \approx -U$), the remaining (non fluctuating) spin on the QD has the minority spin orientation of the tunneling electrons to obey the Pauli principle [91, 95]. The transition between these opposite ground states is described by the sign change of the exchange field in Eq. 5.1. However, if Δ_0 is the dominant term, a roughly constant splitting

of the Kondo resonance within a charge state is expected. This is shown in Fig. 5.3. Eq. 5.1 is used to plot the exchange-split Kondo resonances appearing at $\pm\delta_{ex}$ for two different Δ_0 values (panel a): $\Delta_0 = -0.064$ meV, panel b): $\Delta_0 = -0.64$ meV) and magnetic fields B is plotted. For $P\Gamma$ the experimentally found value of 0.22 meV is used. Clearly, it is oversimplified to only change Δ_0, since Δ_0 is in principle dependent on Γ [92]. Thus, changes of Δ_0 would also modify the prefactor of the logarithmic term in Eq. 5.1. Nevertheless, the basic feature is clearly reproduced in Fig. 5.3. Also visible is the effect of an external magnetic field B. A positive B brings the two split Kondo resonances closer together. A negative B would split the resonances further apart. Consequently, from magnetic field dependence measurements of exchange-split Kondo resonances the sign of B_{ex} can be deduced. This is demonstrated using the plots of Fig. 5.3. For Δ_0 being dominant as in panel b), it is more straight forward and is discussed first. A positive B reduces the splitting and therefore the sign of B_{ex} is opposite to the external field, in this case negative. The situation shown in panel a) is slightly more delicate: The crossing of the split Kondo ridge can be interpreted as spin ground state reversal of the QD. This implies a sign change of the field, responsible for the spin degeneracy lifting. Thus, B_{ex} left and right from the crossing point have opposite signs. To obtain the sign of B_{ex} for the two sides, one either uses Eq. 5.1 to fit the data points (see next section) or makes a $G(B, V_{SD})$ measurement somewhere within the charge state. If the splitting increases/decreases B_{ex} is parallel/antiparallel to B. Knowing the sign of B_{ex} allows to attribute the ground state spin orientation to the two sides (left/right from the restored Kondo peak) by considering the Zeeman energy. But where do the different signs of B_{ex} originate? From Eq. 5.1 the main contributions can be determined. It is the tunneling spin polarization P and Γ (which essentially also influence Δ_0). If Γ is considered to be roughly constant (e.g. V_{BG} fixed) then a reversal of the polarization of the F contact, leads to a B_{ex} sign change. Furthermore, by varying V_{BG}, different charge states are accessed. This modifies Γ and thus influences B_{ex}.

5.3 Ferromagnetic proximity effect: results

In this section it is shown that the main results described in the previous section can be found experimentally in InAs NW QDs contacted only with a single F lead. In addition, it will be highlighted that InAs NW QDs are an ideal system to study these effects since the g-factor can be comparable to the bulk value of g $\approx$ 15 [71]. Thus, much smaller external fields are needed to access the regime, where the exchange energy and the Zeeman splitting are comparable. In Fig. 5.4a $G(V_{BG}, V_{SD})$ of several charge states

of a studied F-QD-S device is presented. The features seen in this figure (see discussion below) have been observed not only in this gate region but over a wide range of V_{BG} and different devices. However, Fig. 5.4a captures in principle all the aspects of the ferromagnetic proximity effect within a small voltage range and is therefore chosen as a reference measurement. In accordance with the spin-1/2 Kondo effect, a pronounced conductance is seen around ($V_{SD} = 0$ V) in every odd charge state. However, in these states (labeled with numbers 1,3,5,7 in Fig. 5.4a) the Kondo resonance shows different signatures due to correlations induced by the F lead. State 7 shows a normal spin-1/2 Kondo situation with a single resonance line at $V_{SD} = 0$ V. As shown in Fig. 5.4b this zero bias Kondo resonance splits up linearly with B as expected. In contrast, state 3 exhibits clear signature of F correlations,

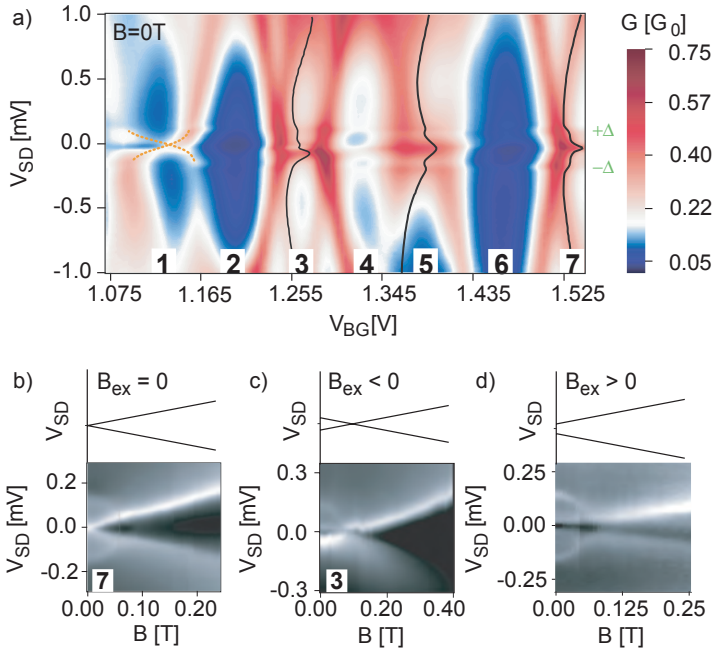

Figure 5.4: *a) $G(V_{BG}, V_{SD})$ of a F-QD-S device at $B = 0T$. B_{ex} modifies the Kondo resonances (odd numbered states) differently. The S lead induces peaks in the conductance at $V_{SD} = \pm\Delta$. B dependence of different charge states: b) with no signature of B_{ex} (state 7 in fig 5.4a), c) with $B_{ex} < 0$, which is compensated by external B (state 3 in Fig. 5.4), d) with $B_{ex} > 0$, which is enhanced by B. Panel d) is measured in a charge state at $V_{BG} = 2.31$ V.*

i.e. the Kondo resonance has a finite and roughly constant splitting at $B = 0$ mT (see black cross-section). Measuring the magnetic field evolution of a split Kondo situation $G(V_{SD}, B)$ the value for B_{ex} can be deduced from the B field where the Kondo resonance is restored. This is shown in Fig. 5.4c, where the splitting from state 3 is compensated by $B \approx 64$ mT and split again at higher B fields. Thus $B_{ex} = -64$ mT, having an opposite sign than the external field. Another type of B dependence of the Kondo ridge is presented in Fig. 5.4d (measured at $V_{BG} = 2.31$ V), where the zero field splitting of the resonance is further increased by an applied field. It means that B_{ex} is parallel to B for this state. The three markedly different magnetic field behaviors (Fig. 5.4b-d) demonstrate that B_{ex} strongly depends on the QD level. Even in a small backgate range the amplitude and the sign of B_{ex} varies. This observation highlights the particular importance of the coupling of the QD state to the F lead for the charge fluctuations induced local exchange field [91]. Two things should be noted: First, in order to make statements about the sign of B_{ex} it is crucial that prior to each magnetic field evolution measurement the F contact is first magnetized by applying B in the order of the saturation field. This ensures that the magnetic state of the contact is known at all times. Second, from the above shown measurements, the different B dependencies from Fig. 5.4b,c,d also prove that the observed effect can not solely be described by stray fields, since the stray field does not depend on the backgate.

Asymmetry in the maximum conductance of split Kondo resonances

Additional attention should be payed on a particular feature seen in Fig. 5.4a state 1 & 3 and all the magnetic field evolutions of Kondo resonances shown in Fig. 5.4b,c,d. In all these figures one of the split Kondo peaks has a larger maximum conductance. This can be understood intuitively. In equilibrium and no magnetic field the Kondo singlet gives rise to a peak in the density of states at the chemical potential of the lead. Upon applying a magnetic field, this peak in the DOS splits up (Fig. 5.5a) by twice the Zeeman energy [48]. In the case of F contacts, the transmission coefficients for spin-$\uparrow$ and spin-$\downarrow$ are different (see above). Thus, the split DOS peaks from the Kondo resonance have different strength (Fig. 5.5b) which gives rise to the observed asymmetry of the differential conductance of the two resonances. This is substantiated by calculations of Soller [99]. In Ref. [99], the differential conductance (and even the full counting statistics, FCS) through a F-QD-S structure in the Kondo regime is calculated, by describing the transport properties of the Kondo effect by a resonant level system. Due to the F contact, the induced exchange splitting has to be taken into account. This

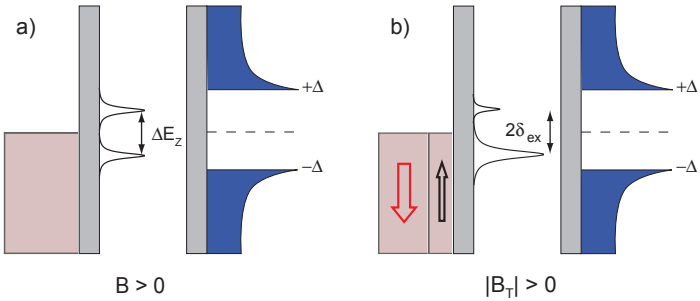

Figure 5.5: *a) Schematic for the Kondo density of states (DOS) in a finite magnetic field for a N-QD-S system. The DOS is split by $\Delta E_Z = 2g\mu_B B$. b) Exchanging the normal contact (N) by a ferromagnetic (F) contact the spin asymmetry is reflected in the split Kondo DOS for a finite B_T ($B_T = B + B_{ex}$).*

is done by exchanging first Γ in Eq. 5.1 by the effective Kondo-coupling Γ_K to the superconductor. From this the DOS for the Kondo peaks for both spin directions can be written as

$$\rho_{K\sigma}(\omega) = \frac{\Gamma_K^2}{(\hbar\omega - eV + \sigma\delta_{ex})^2 + \Gamma_K^2} \tag{5.2}$$

where δ_{ex} describes the exchange field induced energy splitting from Eq. 5.1 including the effective Kondo-coupling Γ_K. The effective transmission coefficients for the system (i.e. single electron and Andreev processes) can then be calculated by using the tunneling transmission coefficients for an S-quantum point contact (QPC)-F system multiplied with the relevant effective DOS (Eq. 5.2). Furthermore, also a finite (constant) DOS from outside of the Kondo peak (background DOS) is taken into account. Using these results, the differential conductance (from the FCS) can then be calculated. In Fig. 5.6 the theoretical results (blue curve) are compared to a $B = 0$ mT slice taken from Fig. 5.4a state 3 at $V_{BG} = 1.28$ V (red curve). Good agreement is found with $P = 0.46$ and $\Delta = 140$ μeV, reasonable values for the used F and S material. Observed deviations may result from neglecting the energy dependence of the background DOS. This implies a weak/strong coupling of the Kondo QD to the S/F contact, since only in this case the mapping to the resonant level works well [99]. This is reflected in the absence of spin-active scattering [63] (see also section 2.3.2). In the model of Soller *et al.* [99] it has not been accounted for. Spin-active scattering processes would lead to a reduction of the asymmetry of the differential

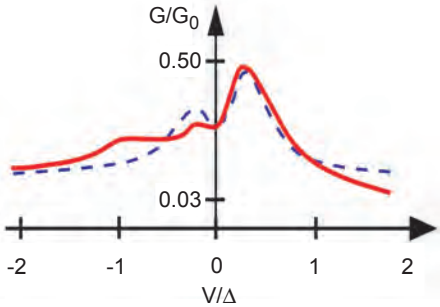

Figure 5.6: *Theoretical differential conductance (blue curve) through a F-QD-S system compared to a DC bias slice taken from Fig.5.4a state 3 at* $V_{BG} = 1.28$ *V (red curve). Taken from [99]*

conductance peaks, since the tunnel transmission of one spin orientation would couple to the Kondo singlet corresponding to the opposite spin direction [99]. Since the model is in agreement with the data without spin-active scattering and additionally a strong asymmetry is observed (see Fig. 5.6), it can be concluded that spin-active scattering is not relevant in this case. No spin-active scattering means that the spin quantization axis at the interface is almost perfectly aligned with the one of the bulk F. This is especially interesting for follow-up experiments of the ones shown in chapter 6, which would rely on effective spin projection measurements (see i.e. section 6.1 & 6.7). E.g. by exploiting the asymmetry in the two Kondo peaks for efficient spin filtering. Using the FCS obtained from the above mentioned model, the conductances for the different spin species, G_σ can be calculated [99]. These allow to determine the quality factor for spin filtering: $q = |\frac{G_\uparrow - G_\downarrow}{G_\uparrow + G_\downarrow}|$ [99]. For appropriately chosen voltages, $q \approx 70$ % with the parameters used for the fit shown in Fig. 5.6. This is significantly higher than what can be achieved otherwise with a contact polarization of $P = 46$ % which has been used for the fitting.

Magnetic exchange field variations in a single charge state

The discussion of the exchange field manifestation observed in state 1 of Fig. 5.4a, has been omitted so far. The Kondo resonance is also split for this state, however the size of the splitting strongly varies with V_{BG} (The resonance lines are highlighted with dashed lines in Fig. 5.4a). The split Kondo resonance lines also cross the $V_{SD} = 0$ mV value inside the charge

state. This dependence suggests that B_{ex} within this charge state first gets smaller as V_{BG} is increased. With further increasing V_{BG} it changes its sign and increases further in the opposite direction. This situation corresponds to the electrically controlled ground state transition on the QD described by Eq. 5.1. Eq. 5.1 quantifies the energy difference between the spin-↑ and

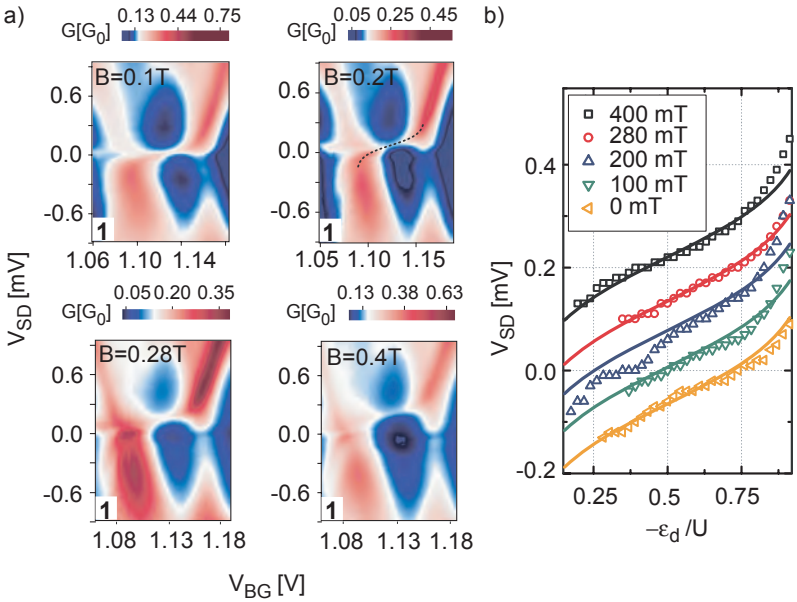

Figure 5.7: *Measurements on state 1. a) Colorscale plots at different magnetic fields. The dashed line highlights the position of the tilted Kondo resonance at $B = 0.2$ T. b) The evolution of the Kondo resonance is presented for different B fields by symbols. The lines are fits using Eq. 5.1*

the spin-↓ states for different V_{BG} values, which corresponds to half of the energy (eV_{SD}) between the split Kondo ridges. Using the g-factor extracted from the B evolution of $G(V_{BG}, V_{SD})$ (see below), the energy can be converted to a magnetic field value to obtain $B_{ex}(V_{BG})$. Therefore, reading-out V_{SD} for the appearance of the Kondo resonance for each V_{BG} allows to determine B_{ex} at all backgate voltages within the investigated states. More importantly, agreement with Eq. 5.1 is the strongest evidence that the fundamental mechanism for the observed features is the magnetic proximity effect. In addition, from Eq. 5.1 important device parameters can be obtained. $G(V_{BG}, V_{SD})$ of state 1 is measured in different magnetic fields. As

it is seen in Fig. 5.7a, the position of the more pronounced split Kondo line moves to higher source drain voltage values as B is increased. The (V_{BG},V_{SD}) coordinates of this line is read out from the measurements, see e.g. the dotted line for $B = 0.2$ T. Fig. 5.7b summarizes the measured position of the Kondo ridge by symbols at different B fields. The theory described by Eq. 5.1 nicely fits the experiment (see lines) with the parameters: $|g| = 12.3$, $\Delta_0 \approx -64$ μeV and $P\Gamma = 0.22$ meV. It should be noted that first the g-factor has been determined from the expected (vertical) Zeeman shift of the curve and afterwards Δ_0 and $P\Gamma$ have been obtained by fitting the data to Eq. 5.1. Converting Δ_0 to a magnetic field, B_{ex} at $\epsilon_d = -U/2$ is calculated to ≈ -90 mT.
As it has been shown, from fitting the data with Eq. 5.1, B_{ex} in the center of the charge state can be deduced. However, B_{ex} in situations like state 1 of Fig. 5.4a is strongly gate dependent. A measure for the exchange splitting at different gate voltages can be obtained by measuring the compensation field for which the Kondo peak is restored. Thus, if one measures $G(V_{BG}, B)$

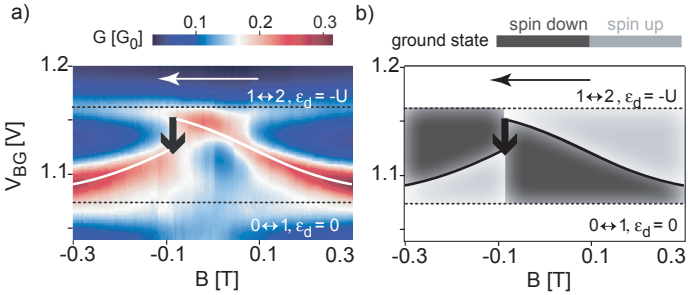

Figure 5.8: *a) Measurements on state 1. Differential conductance as a function of V_{BG} and B measured at $V_{SD} = 0$ mV. The two horizontal ridges (dotted lines) are the charge state boundaries. The high conductance ridge is the restored Kondo resonance, where $B = -B_{ex}(V_{BG})$. This ridge separates the regions where spin-↑ or spin-↓ is the ground state. The white line is a plot based on Eq. 5.1 using the parameters obtained from the fits shown in Fig. 5.7b. The white arrow shows the sweeping direction of B. The black arrow points out the position where the magnetization of the F lead changes sign. b) Indicating the spin ground state of the QD in the $V_{BG} - B$ plane for the measurement from panel a).*

at $V_{SD} = 0$ mV, at each V_{BG} signatures of high conductance are expected if $B = -B_{ex}(V_{BG})$ due to the restored Kondo resonance. Such a plot is presented in Fig. 5.8a. The lower/upper ridge (see dashed lines) defines the resonance positions when the occupation of the QD level changes between $0 \leftrightarrow 1$ /$1 \leftrightarrow 2$. The white arrow indicates the sweep direction of B. The

high conductance lines with finite slope show the evolution of the Kondo resonance (marked with a white line). At each B field the gate position of the restored Kondo resonance defines the border between the spin-↑ and the spin-↓ ground states. At high external magnetic fields (i.e. $B \geq 0.3$ T) the Zeeman term dominates (see Eq. 5.1). Therefore, considering that the g-factor of InAs is negative, the spin-↑ is the ground state for all gate values in high field and the Kondo resonance coincides with the border at $\epsilon_d = 0$. Hence, at each magnetic field, in the V_{BG} range between the Kondo resonance and the charge state border at $\epsilon_d = -U$ the QD has spin-↑ as ground state, whereas a spin-↓ ground state is found between the Kondo resonance and $\epsilon_d = 0$ as illustrated in Fig. 5.8b. As the B field decreases the restored Kondo peak moves towards $\epsilon_d = -U$, opening backgate regions where spin-↓ is the ground state. At $B = 0$ mT the spin-↓ state dominates, and spin-↑ remains only in a small gate region around $\epsilon_d = -U$ the preferable spin orientation. The gate voltage value as a function of B, where the spin ground state change takes place, can be expressed with Eq. 5.1 using the condition of $eV_{SD} = 0$. The white line in Fig. 5.8a shows such a curve, giving a good agreement without fitting parameters but by using the values deduced from Fig. 5.7b ($|g| = 12.3$, $\Delta_0 \approx -64$ μeV and $P\Gamma = 0.22$ meV). Additionally, since the g-factor of the InAs QD state is large ($\approx$ six times the free electron g value), the sign change of B_{ex} can be nicely observed. It is induced by switching the polarization of the F lead to the opposite direction by B larger than the coercive field of the contact. In the measurement this appears as a step in the $G(V_{BG}, B)$ plot (see black arrow in Fig. 5.8a) since the splitting turns from $g\mu_B(B + B_{ex})$ to $g\mu_B(B - B_{ex})$.
Furthermore, the ferromagnetic proximity effect allows for the comparison of the polarization of the F lead and the polarization of the tunneling electrons. As visible in Fig. 5.8 in the vicinity of the $0 \leftrightarrow 1$ border at $B = 0$ mT, the ground state is spin-↓. At this border the preferable spin orientation on the QD is the majority tunneling spin orientation (see section 5.2 and Fig. 5.2b) [91, 95]. Since the F lead prior to the measurement has been polarized into spin-↓ state by a positive B field[1], it can be concluded, that the polarization of the F lead and the polarization of tunneling electrons are the same.

[1] The magnetic moment $\mathbf{m}$ is parallel to $\mathbf{B}$, thus the spin $\mathbf{S}$ must be antiparallel ($\mathbf{m} = -g_s\mu_B\mathbf{S}/\hbar$ with $g_s \approx 2$).

5.4 S-QD-F devices as spectroscopy tool for the ferromagnetic proximity effect without Kondo correlations

So far only the effects of the ferromagnetic contact on the InAs NW QD system has been described. However, the investigated devices have, in comparison to the previous experimental studies on ferromagnetic proximity effect [93, 95], instead of two F contacts, an F lead and an S contact. The interplay of S and F correlations in this hybrid configuration might lead to novel effects. Indeed a subgap structure is observed, which seems to be related to the exchange field [26, 99]. This is addressed in this section in more detail.

The most predominant effect of the S contact in transport measurements such as $G(V_{BG}, V_{SD})$ is the appearance of conductance maxima at $V_{SD} = \pm\Delta$ (see e.g. Fig. 5.4). These maxima are related to the singularities of the S DOS as depicted in the schematics shown in Fig. 5.2a and diminish with increasing B field. The interplay between Kondo physics and superconductivity has already been studied in detail in the literature [100, 101, 102, 103, 104, 105] and is not addressed in this thesis. Here the focus is on a novel subgap feature appearing in several charge states of different devices, where spin-1/2 Kondo resonances are not present (neither in the S nor in the normal state). This seems to imply that *even states* are considered. As a matter of fact, most of the states where such signatures have been observed seem to be even states. However, there are a few which can not be attributed to even states with certainty (i.e. in these cases, no clear even-odd behavior has been seen). In Fig. 5.9 a $G(B, V_{SD})$ measurement is presented for a state where this subgap feature is visible. In a bias window of $\approx 50\ \mu$V the conductance shows significantly smaller values than in the rest of the superconducting gap (see horizontal dashed line). As can be seen in Fig. 5.9 (and also Fig. 5.10b), this mini-gap is clearly connected to superconductivity since it is strongly suppressed above the critical field of the S lead (see green dotted lines in Fig. 5.9 for the magnetic field evolution of the superconducting gap Δ).

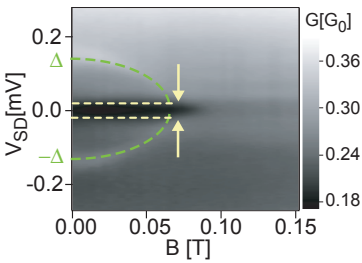

Figure 5.9: $G(B, V_{SD})$ measurement: A subgap feature appears (horizontal dashed lines) at the energy scale of the exchange field. The feature is suppressed above the critical field of the superconductor.

On the other hand, the energy scale of the novel subgap feature coincides with the exchange energy observed in the split Kondo states discussed in the previous section (see e.g. Fig. 5.4c,d). This suggests that the subgap feature is also exchange field related. Further evidence for this relation is shown in the $G(V_{BG}, V_{SD})$ measurement at $B = 0$ mT on an other device (see Fig. 5.10a). The middle charge state with odd electron filling (o) shows a slightly split Kondo resonance, while the two even states (e) exhibit the new subgap feature. As it is highlighted by the dotted lines, the mini-gap in

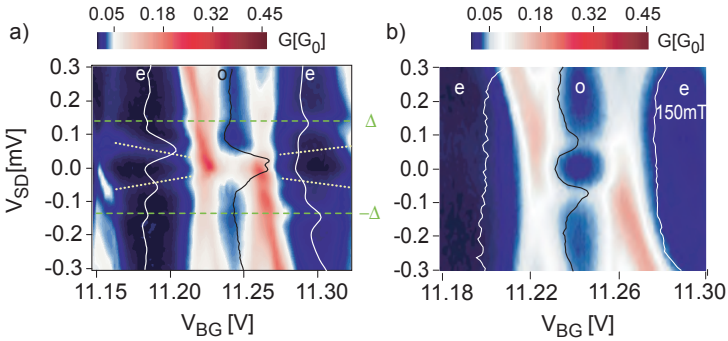

Figure 5.10: *a) $G(V_{BG}, V_{SD})$ at $B = 0$ mT showing the relation of the new subgap structure to B_{ex}. Inside the superconducting gap additional resonance lines appear in even charge states (see dotted lines). These resonances change their position with gate voltage and merge into the exchange split Kondo resonance lines at the border of the odd charge state. The line graphs show $G(V_{SD})$ cuts in the middle of the three charge states. b) $G(V_{BG}, V_{SD})$ at $B = 150$ mT from the same charge states as in a). All the signatures of superconductivity as well as the subgap feature have vanished.*

the even charge states merge into the split Kondo resonance at the border between the even and the odd states. In panel b) the same charge states at $B = 150$ mT are shown. No signature of the mini-gap can be seen anymore and superconductivity has vanished. Thus, superconductivity related transport processes in non-Kondo states are presented, which seem to be correlated with the exchange splitting.

In the following a possible explanation for the observed feature is given, which relies on spin-active scattering mechanisms [99]. It has be shown that in the presence of Kondo correlations the QD forms a collective state with the F contact, which can be described by a resonant level system (section 5.3). For these states, it has been concluded that spin-active scattering is absent. On the other hand, the sub-gap feature was seen in non-Kondo states[2]. For such states, there is no reason why the interface quantization

[2]There are hints that it is also visible in Kondo states but the Kondo resonance renders

axis should be aligned with the bulk F one. Therefore spin-active scattering needs to be taken into account, which can induce spin-flip Andreev reflections (SAR) [63]. SAR goes only through one spin level on the QD, therefore the two SAR conductance peaks (for spin-↑/spin-↓) split up in the presence of a finite exchange field. This gives rise to a mini-gap feature, like the ones shown in Fig. 5.9 & 5.10a. In Ref. [99] within the framework of the full

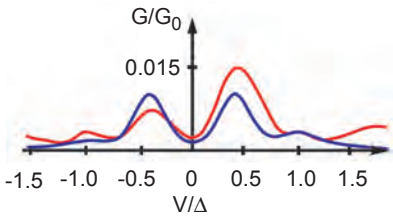

Figure 5.11: *Theoretical differential conductance (blue curve) through a F-QD-S system compared to a DC bias slice taken from Fig.5.10a at* $V_{BG} = 11.175$ *V. Taken from [99]*

counting statistics an effective model of a S-QD-F system, with an exchange field induced level splitting and spin-active scattering has been calculated. A fit of the resulting differential conductance (blue line) to a $G(V_{SD})$ slice (red curve) taken from the measurements shown in Fig. 5.10a is presented in Fig. 5.11. The four-peak structure referring to the superconductor DOS and the exchange field is nicely obtained, for $P = 0.46$, $\Delta = 140$ μeV and $\delta_{ex} = 0.4 * \Delta$. Thus, it appears as if in this S-QD-F system the proximity induced ferromagnetic exchange field can be visualized also in charge states where no Kondo correlation is present. Furthermore, the observation of the subgap structure can be viewed as a signature of the triplet proximity effect induced by the spin-active interface of the F lead similar to the recent observations by Hübler *et al.* [106].

5.5 Summary

The reported measurements demonstrate that a ferromagnetic proximity effect is present in devices containing only a single F lead. It was shown that the signal can be observed in split Kondo resonances which are strongly asymmetric in splitting strength. This allows for efficient spin selection if

clear observation impossible.

the source-drain bias window is chosen appropriately [99]. Additionally, it seems that the Kondo effect also aligns the interface spin with the bulk ferromagnet. This implies an absence of spin-flip scattering at the interface which is an advantage for spin projection measurements, e.g. for entanglement detection (see chapter 6). Furthermore, in accordance with observations by Hauptmann *et al.* [95] and predictions by Martinek *et al.* [91] an electrical tuning of the QD spin ground state has been observed. This makes the F-InAs QD-S system a promising building block for spin correlation studies, if implemented into a Cooper pair splitter device [107, 108] (see chapter 6). Having a S lead in these devices induces additional transport channels. As a result a subgap structure is observed in even charge states, which appears to be exchange field related. A possible model is presented which relies on spin flip scattering. Reference to detailed calculations is made [99] where within an effective model for a S-QD-F system, with an exchange field induced level splitting and spin-active scattering, good agreement with the here presented data is obtained. All this suggests that the subgap structure originates from triplet correlations in the ferromagnet [99] . Besides, it would allow for the visualization of the ferromagnetic proximity effect in charge states where no-Kondo correlations are present.

CHAPTER 6

Cooper pair splitting in a two-quantum-dot Y-junction

Entangled Einstein-Podolsky-Rosen (EPR) pairs [10] are the toy objects to explore non-locality, fundamental to quantum mechanics. Whereas pairwise entangled photons have been used to test Bell inequalities [109], such experiments are not yet possible for solid-state systems where spin-1/2 mobile electrons are the natural quantum objects [3]. Although termed single quasiparticles, electrons participate in a macroscopic ground state called the Fermi sea. It is therefore not straightforward to generate entangled pairs of electrons on demand, separate the two electrons of each pair and move them apart in order to eventually test Bell inequalities. A superconductor, however, can act as a source of EPR pairs of electrons, because its ground-state is composed of Cooper pairs in a spin-singlet state [8]. These Cooper pairs can be extracted from a superconductor by tunneling. However, the splitting of the pairs into separate electrons has to be *enforced* to obtain an efficient EPR source. This can be achieved by having the electrons "repel" each other by Coulomb interaction [9]. Controlled Cooper pair splitting can thereby be realized by coupling of the superconductor to two normal metal drain contacts via individually tunable quantum dots.
In this chapter, the experimental realization of such a tunable Cooper pair splitter (CPS) is demonstrated. Before the details of the setup are presented, the (theoretical) background is provided. The experimental part is closed by first approaches to optimize the Cooper pair splitting. A summary and outlook can be found at the end of this chapter. Parts of this chapter have been published elsewhere in similar form [107].

6.1 Background, concept and principle of Cooper pair splitting

This section has two main purposes. One is to introduce the concept of entanglement and discuss the consequences of this remarkable feature of quantum mechanics. The other is to present one specific source of entanglement, namely Cooper pairs in an s-wave superconductor, and possible mechanisms to extract them in a controlled manner. Special attention is paid to the proposal provided by Recher *et al.* [9].

6.1.1 Entanglement

Entanglement is a resource provided by quantum mechanics (QM). Formally it is best understood in a two particle system[1], described by the state $\Psi(x_1, x_2)$. Following the principles of quantum mechanics Ψ can be written as a superposition of product states $\phi_i(x_1)\phi_j(x_2)$, with $\phi_i(x), \phi_j(x)$ the single particle wave functions and x_1, x_2 the coordinates for each of the two constituents. In other words, the Hilbert space H of the entire system, has been partitioned into the two subspaces of the single particles. Entanglement is now defined such, that a wave function *is not entangled* if it can be written as a product of the wavefunctions, $\phi_i(x_1)$ and $\phi_j(x_2)$, from the two subspaces, e.g. $\Psi(x_1, x_2) = \phi_1(x_1)\phi_2(x_2)$.
For illustration, consider the spin singlet:

$$|\Psi\rangle = \frac{1}{\sqrt{2}} \left(|\uparrow_1\downarrow_2\rangle - |\uparrow_2\downarrow_1\rangle\right) \tag{6.1}$$

The indices stand for electron 1 and electron 2, respectively, whereas the arrows indicate the "spin orientations". It is impossible to tell the spin states of the two electrons without performing a measurement on the system. However, a "projection measurement" of the spin state on one of the electrons dictates, according to quantum mechanics, the state of the other. Even more remarkable is the insensitivity of this effect on the distance between the two electrons. Separating the two electrons by an infinite distance does not alter the instantaneous determination of the spin state of e.g. electron 1, if a measurement on electron 2 is performed. This apparent conflict with special relativity has led to the formulation of the famous Einstein-Podolsky-Rosen paradox [10], fundamental to the debate on the completeness of QM. The quantum mechanical description of the spin measurement implies a non-local influence on electron 1 if electron 2 is measured. To circumvent the problem

[1] It should be noted, that the concept is not limited to two particles, but for simplicity and the usefulness of two particle systems, the discussion is limited here to this case.

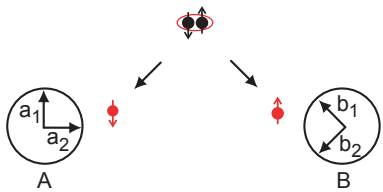

Figure 6.1: *A schematic for a Bell measurement with spin-1/2 particles. First, they are separated to the points A and B. Afterwards projection measurements along the axes $a_{1,2}$ and $b_{1,2}$ are performed. Calculating the required correlations (see Eq. 6.2), allows to determine whether or not the two particles are entangled.*

of *non-locality*, local hidden variable theories were suggested [110]. Applied on the above example, they rely on the assumption of the two electrons interacting with each other before separation, determining their behavior depending on the measurement performed. In these theories the interaction is characterized by a so-called hidden variable [110]. With the help of it, locality can be preserved. The nowadays present believe in the completeness of quantum mechanics and thus non-locality, has its foundation in the work of Bell from 1964 [111]. For a correlation measurement between two separated particles (see Fig. 6.1) a simple inequality can be derived, which has to be fulfilled by all local hidden variable theories [112]:

$$|-\langle\sigma_1^A\sigma_1^B\rangle+\langle\sigma_1^A\sigma_2^B\rangle-\langle\sigma_2^A\sigma_2^B\rangle-\langle\sigma_2^A\sigma_1^B\rangle|\leq 2 \tag{6.2}$$

$\langle\sigma_i^A\sigma_i^B\rangle$ stands for the expectation value of a correlation measurement of the particles spin along the axis $a_i (i = 1, 2)$ for the positions A and b_i for B as shown in Fig. 6.1. It is expected that for the angle between the projection axes, namely $(a_1, b_1) = (b_1, a_2) = (a_2, b_2) \equiv \Theta$ and $\Theta = 45°$, a maximal violation of this inequality occurs [112]. A violation of Eq. 6.2 has experimentally been shown with photons the first time in 1982 [109] and later as well in Josephson qubits [113]. However, the experiments with spin-1/2 particles have not yet been performed. So far, this originates mainly in the difficulty of generating entangled electron pairs (so-called *EPR pairs*) on demand. The here presented measurements may lay the foundation to circumvent this problem. But still many challenges have to be overcome to finally realize Bell inequality measurements with electrons. This is discussed in section 6.7.

Having introduced entanglement and the related fundamental question about non-locality raises the question: what is entanglement good for? A topical field is quantum information science. To understand the value of entangle-

ment for this field, it is useful to introduce *qubits*. A qubit is the quantum analog to the classical bit. It can be any quantum two-level system available, like ion-traps, superconducting loops and QDs, to name a few. Here, following Ref. [3], the electron spin in QDs is the candidate of choice. Besides the recent progress in the field of QD based spin qubits [76, 7], this is motivated by the use of such systems for *on-chip* quantum computation. A natural computation basis for the electron spin is the spin-$\uparrow$ (e.g. $|\uparrow\rangle \equiv |0\rangle$) and spin-$\downarrow$ (e.g. $|\downarrow\rangle \equiv |1\rangle$) state. In contrast to classical bits, a qubit can now be in a superposition of $|\uparrow\rangle$ and $|\downarrow\rangle$ states: $|\Psi\rangle = \alpha_1 |\uparrow\rangle + \alpha_2 |\downarrow\rangle$ with $|\alpha_1|^2 + |\alpha_2|^2 = 1$. Similarly, a two qubit system can be described as $|\Psi\rangle = \alpha_1 |\uparrow\uparrow\rangle + \alpha_2 |\uparrow\downarrow\rangle + \alpha_3 |\downarrow\uparrow\rangle + \alpha_4 |\downarrow\downarrow\rangle$ with the four coefficients fulfilling $\sum_{i=1}^{4} |\alpha_i|^2 = 1$. Scaling this up, a n-qubit state $|\Psi\rangle$ would have 2^n coefficients α_i, which satisfy $\sum_i |\alpha_i|^2 = 1$. A classical computer would therefore need 2^n bits to store the information of $|\Psi\rangle$, in contrast to the n qubits used in a quantum system. In $|\Psi\rangle$ the classical bits are encoded by the corresponding basis states. More interesting are superpositions of basis states since they are entangled. They are an important ingredient for fast algorithms in quantum computations and quantum cryptography [114, 115]. An operation performed on a quantum state which is in a superposition of basis states, acts on all the states simultaneously at once! Considering that a n-qubit state may be in a superposition of 2^n basis states reveals the vast power of entanglement. This *quantum parallelism* is at the heart of the speed-up of quantum computation [115]. However, already the entanglement between two qubits is sufficient to illustrate its power. One already experimentally realized example is teleportation [116, 114]. Sharing an EPR-pair (see Eq. 6.1) between the spatially separated Alice and Bob allows, due to the principles of non-locality, to transmit a quantum state ψ from Alice to Bob. More technically, Alice interacts her part of the EPR-pair with ψ by some unitary transformations (*quantum gates*) and measures her system. Since the two qubits from the EPR-pair are correlated, Bob performs the necessary transformations depending on the classically communicated outcome of Alice's measurement to obtain ψ from his part of the EPR-pair. It is quite remarkable consequence of entanglement that in this simple scheme, a quantum state can be transferred from Alice to Bob.

Being aware of the power of entanglement and the use of electron spins in QDs as qubits, it is natural to look for possibilities to generate controlled entangled mobile electrons. A possible mechanism to deal with this challenge is the topic of the subsequent part: the use of superconductors as EPR-source is discussed, where Cooper pairs are naturally in a spin-singlet state.

6.1.2 Superconductors as source of EPR pairs

An "entangler" that generates correlated EPR pairs of electrons in the solid-state has to be based on two-particle interactions, such as the exchange interaction and Cooper pairing in superconductors. The former is mediated by electron-photon (Coulomb interaction) and the latter by electron-phonon interaction. Proposals for electron entangler that make use of Coulomb interaction in quantum dots [117, 118] and superconducting devices [119, 120, 121] have been put forward. Even more advanced, and in practice also more versatile and efficient, are device proposals that exploit both phenomena [9, 122, 123, 124, 125].

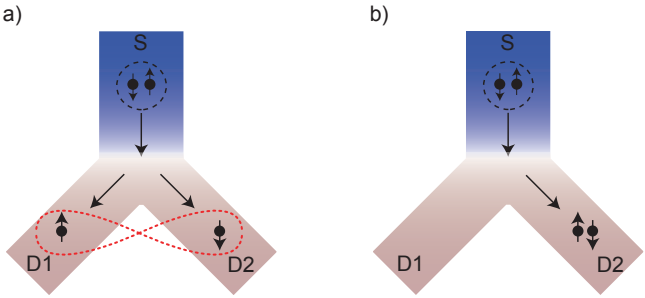

Figure 6.2: *a) Illustration of Cooper pair splitting in a Y-junction geometry with the superconductor (S) acting as a source. b) Undesired process of the Cooper pair being transmitted into the same contact.*

An electron entangler is a device which converts a charge current on the input to a stream of spin-entangled electron pairs. Each pair is split into its individual electrons that emerge at two different arms of an electronic fork or Y-junction device (Fig. 6.2a) [126]. However, if Cooper pairs are injected into the fork, the pairs do not necessarily split as required, but may also be transmitted together into either arm as shown in Fig. 6.2b. The ratio between pair splitting and direct pair transmission depends on details of the scattering matrix [126, 127, 128, 129, 130, 131]. Such a device does not provide control over the two processes, a problem also encountered in experiments on metallic nanostructures where first hints for Cooper pair splitting have been observed [88, 132, 60]. The desired Cooper pair splitting can be enforced if the fork is made up of two QDs as shown in Fig. 6.3 [9, 125]. This structure is now discussed in more detail.
At energies below the superconducting gap Δ, only Cooper pair tunneling is

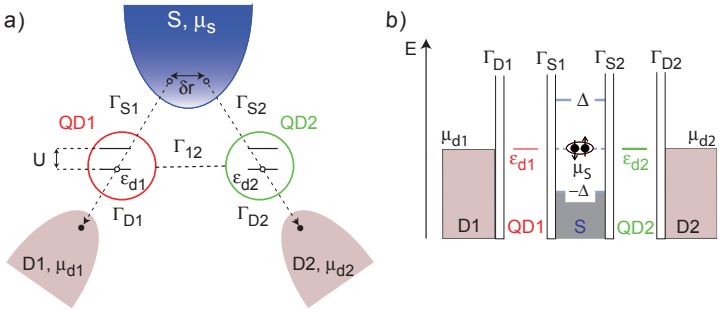

Figure 6.3: *A schematic of a Cooper pair splitter based on the proposal by [9] a) with the corresponding energy diagram b). The two constituents from the Cooper pair singlet are injected into the QDs from two points, separated by δr. The tunnel coupling of S to the QDs is characterized by $\Gamma_{S1,2}$ and the one from the QDs to the drains $D1, 2$ by $\Gamma_{D1,2}$. Γ_{12} is the interdot coupling. U symbolizes the charging energy of the QDs and $\epsilon_{d1,2}$ their electrochemical potentials. The electrochemical potentials of the leads are given by μ_s, μ_{d1} and μ_{d2}. Illustration after [9, 108]*

possible[2]. To exploit the QDs at each arm as efficient filter for the undesired process of both electrons tunneling into the same lead (direct pair tunneling (DPT)), the QDs have to satisfy certain constraints and need to be tuned into the optimal parameter regime. The illustration in Fig. 6.3a gives an overview of the relevant device parameters and introduces the used notations. In panel b) the corresponding energy diagram is drawn, to illustrate the following description. The tunnel coupling of the superconductor S to QD1 and QD2, is characterized by the tunneling coupling Γ_{S1} and Γ_{S2}. The points where the two electrons tunnel into the respective QDs are separated by δr. The QDs, with their chemical potentials $\epsilon_{d1,d2}$ and (for simplicity equal) charging energy U, are tunnel coupled to the drain contacts $D1, D2$ by $\Gamma_{D1,D2}$ and connected to each other with the interdot coupling Γ_{12}.
Complementary to the frequently used ac biasing to measure the differential conductance, also a small dc bias could be applied $\Delta\mu = |\mu_S - \mu_{d1,2}|$ with $\mu_{d1} = \mu_{d2}$. In such setups, to have the tunneling into different QDs at resonance, $\epsilon_{d1} + \epsilon_{d2} = 2\mu_S$ has to be fulfilled [9, 125]. The QDs can therefore act as energy filters. Besides this energy conservation constraint, the most obvious requirement for efficient splitting is a large charging energy U. Because if one of the electrons from the Cooper pair tunnels into QD1, double occupancy of QD1 is prohibited due to the large charging en-

[2]In this chapter transport is considered from the superconducting side. Direct Cooper pair tunneling can be viewed as normal Andreev reflection, whereas Cooper pair splitting is the terminology used for crossed Andreev reflection.

ergy (more accurately, it is suppressed by $\sim 1/U$ [9]). Therefore, the second electron leaves into QD2 or has to wait till the first electron has left QD1. However, this unwanted sequential tunneling of the Cooper pair through the same QD is suppressed by $\sim 1/\Delta$. Naturally, this reasoning makes only sense if $k_B T, \Delta\mu < \Delta, U$. If this constraint is not met, the next level in the QD becomes accessible and the Coulomb repulsion is not an efficient filter anymore. Moreover, the 2nd electron may remain as a quasiparticle in the superconductor as a final excited state [9]. The desired regime is experimentally feasible. In InAs nanowire QDs, U/k_B is in the order of $10 - 50$ K and the usually used superconductor material (aluminum) has a gap Δ around 1.5 K, temperatures well above standard dilution refrigerator base temperatures. However, CPS may be suppressed if the tunnel coupling $\Gamma_{1,2} = \Gamma_{S1,2} + \Gamma_{D1,2}$ are larger than Δ. In this case the tunneling of the 1st electron through e.g. QD1 happens on a timescale h/Γ_1 which is shorter, than the time given by the Heisenberg uncertainty h/Δ during which the 2nd electron is allowed to be in a virtual quasiparticle excitation in the S lead. Thus, after the 1st electron has left QD1, the 2nd electron may leave S through the same QD, spoiling the desired filtering effect due to the charging energy. It should be noted, that smaller Γ imply less current, which essentially can be translated into less EPR-pairs per second. However, a perfect EPR-pair source should yield entangled pairs at maximum rate and efficiency. Therefore, for possible future applications, a trade-off will be necessary. In real devices, the interdot coupling Γ_{12} can also be relevant. The efficiency of the splitting is higher for small or even no interdot coupling. Otherwise, if e.g. $\Gamma_{12} > \Gamma_{D1,2}$ the efficiency can not exceed 50 % [108]. As an example of a spurious process, imagine that one electron tunnels into QD1, the other into QD2. After the electron from QD1 tunnels into D1, the other electron has a high probability to tunnel from QD2 into QD1 and afterwards into D1, spoiling the desired Cooper pair splitting. A similar unwanted cotunneling process can also take place if Γ_{12} is not relevant but $\Gamma_S \gg \Gamma_{D1,2}$[3]. In this case the cotunneling is mediated through the superconductor resulting into a similar undesired process. To circumvent these issues, the above mentioned energy filter constraint $\epsilon_{d1} + \epsilon_{d2} = 2\mu_S$ can be made more stringent. To simplify the discussion, $\mu_S = 0$. Then, if $\epsilon_{d1} = -\epsilon_{d2}$ with $\epsilon_{d1,2} \neq 0$ and $\Delta\epsilon = |\epsilon_{d1} - \epsilon_{d2}| > \Gamma_1/2 + \Gamma_2/2$, these unwanted cotunneling processes are suppressed. In summary, a Cooper pair splitter operating in the regime

$$U \geq \Delta > \Gamma_{D1,2} > \Gamma_S > \Delta\mu, k_B T \text{ and } \epsilon_{d1} = -\epsilon_{d2} \text{ with } \epsilon_{d1,2} \neq 0 \qquad (6.3)$$

[3] As pointed out in [9], to preserve the spin-correlation of the split Cooper pair it is anyhow more desirable to work in the regime where $\Gamma_S < \Gamma_{D1,2}$.

allows to obtain the maximum splitting efficiency of 100% [9, 125].
However, this is only half the story. In the calculation of the splitting efficiency, a suppression factor of the splitting current arises. It has its origin in the fact that the two electrons from the Cooper pair are injected from two separated points into the respective QDs. This is illustrated in Fig. 6.3 where the two tunneling points in S are δr apart of each other. For a 3D S contact, this results to a suppression factor $p(\delta r)$ depending on δr, the coherence length ξ of the Cooper pair and on the Fermi wavevector k_F [9][4]. In [58], $p(\delta r)$ is calculated in the limit of a mean free path l smaller than ξ. In this case, $p(\delta r)$ is modified from the clean superconductor value to the one valid in diffusive superconductors, which is proportional to $|sin(k_F\delta r)^2/(lk_F)(k_F\delta r)|exp(-2\delta r/\pi\xi)$. Nevertheless, the term $p(\delta r)$ is very small, because already the factor $(lk_F)^{-1}(k_F\delta r)^{-1}$ is, for Al as superconducting material, estimated to $\approx 5 \cdot 10^{-6}$, using the Fermi wavelength $\lambda_F = 3.6\,\text{Å}$, the mean-free path $l = 5\,\text{nm}$ and $\delta r = 150\,\text{nm}$ corresponding to the width of the superconducting contact. Further enhancement of $p(\delta r)$ can be obtained in confined geometries [58, 123]. For 2D S leads it will be only proportional to $1/(k_F\delta r)exp(-2\delta r/\pi\xi)$ and for 1D S only the exponential term should remain. Thus, only in confined systems 100 % splitting efficiency can be reached. Experiments have demonstrated efficiencies up to 50 % [107, 108]. In order to reconcile the experiments with the theory, one might think that the prefactor is inactive. This is substantiated by experiments in metallic structures, where also no suppression of CPS was observed [88, 132, 134]. Another possibility to understand the large measured splitting efficiency, is the leaking of superconductivity into the NW, leading to the mentioned absence of $p(\delta r)$. This issue is addressed in more detail in section 6.5.

6.2 Fabrication and measurement setup

The samples were fabricated by high-resolution electron-beam (e-beam) lithography on pieces of highly doped Si wafers with a 400 nm insulating SiO_2 barrier layer. High quality molecular-beam epitaxy grown InAs nanowires (NWs) with diameters in the range of $d \simeq 80 - 100\,\text{nm}$ were then deposited from an isopropanol solution. The NWs are located with an optical microscope and further processed by e-beam lithography. This includes the fabrication of an aluminum superconducting (S) source contact (blue stripe in Fig. 6.4), ohmic drain contacts (light red), as well as top-gates (yellow stripes). The top-gates are isolated from the NWs by their native surface

[4] Please note, although for the Cooper pair splitting efficiency irrelevant, the existence of theories suggesting the absence of any entanglement for $\delta r > k_F$ [133].

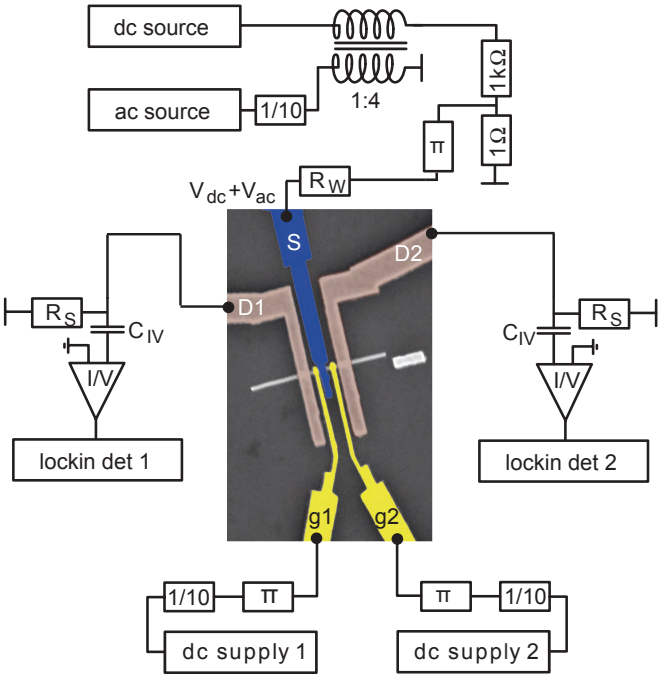

Figure 6.4: *An SEM image of a typical device with the details of the measurement circuit. The measurements were performed by standard lock-in technique in a dilution refrigerator at a base temperature of* 20 *mK. Two quantum dots (QD1 and QD2) are forming between the superconducting (S) source (blue) and the drain leads in the NW. They are individually tunable by dc gate voltage supplies (V_{g1} and V_{g2}). S is biased by both a dc and an ac voltage $V_{dc} + V_{ac}$. The dc source is used when measuring the non-linear differential conductances of the QDs. For the measurements of linear conductances, and in particular for the non-local measurements, the dc source is set to zero. The ac currents I_1 and I_2 through the two QDs are converted to an ac voltage by home-built capacitively coupled current-voltage converters and then amplified by two lock-in amplifiers.*

oxide layer. In order to form low-ohmic source and drain contacts, in-situ argon sputtering is used to remove this oxide layer (see appendix B for parameters). The width of S, the metallic drain contacts, and top-gates are respectively ≈ 150 nm, ≈ 300 nm and ≈ 100 nm. The spacing between source and drain contacts are ≈ 350 nm. QDs form in the wire segments between the contacts when the NW is depleted by an appropriate back-gate voltage. Thus, the structure leads to a beam splitter geometry, where a

superconducting source contact is coupled to two individually tunable QDs. Measurements were performed in a dilution refrigerator at a base temperature of $\approx 20\,\mathrm{mK}$ and the possibility to apply a magnetic field perpendicular to the wire axis. The detailed electronic setup is shown in Fig. 6.4. Standard lock-in techniques are used. An ac voltage source with a frequency in the range of $f = 127 - 400\,\mathrm{Hz}$ is applied to the S contact.[5] It is attenuated to an amplitude of $V_{ac} = 5 - 10\,\mu\mathrm{V}$ by passive voltage dividers and superimposed on a dc bias voltage V_{dc} by a transformer. The dc bias is used to characterize the behavior of the QDs at finite bias. Two home-built current-voltage (I/V) converters with a gain of 10^7 V/A and input impedance $R_{input} = 220\,\Omega$ are used as preamplifiers and connected to two separate lock-in amplifiers used to measure the ac currents through each QD separately (I_1 and I_2). These yield the differential conductance. The non-local measurement is however performed in linear response with $V_{dc} = 0$, so that $G_{1,2} = I_{1,2}/V_{ac}$. In order to eliminate a possible dc biasing from the I/V converters caused by the offset voltage of the input amplifiers, the I/V converters were capacitively coupled with $C_{IV} = 10\,\mu\mathrm{F}$. This also ensures that the two QDs are biased symmetrically. The two series resistors R_S serve to define the ground potential of the drain contacts. Values in the range of $100\,\mathrm{k}\Omega$ to $10\,\mathrm{M}\Omega$ were used. In order to ensure that the ac current flows through the I/V converter and not through R_S, the time constant $R_S C_{IV}$ has to be chosen much larger than the inverse frequency f of the ac excitation. This is already the case for $R_S \gg 125\,\Omega$. In non-linear measurements when a finite *dc* bias voltage V_{dc} is applied, the voltage drop over R_S is corrected afterwards.

6.3 Measurement principle

The investigation of Cooper pair splitting is not straight forward. To understand the results presented in the next section, here the details of the measurements are shown.

Fig. 6.5a is a schematic of the device: The two quantum dots (QD1 and QD2) formed in the NW segments between the S (blue) lead and the drains (light red contacts) are individually tunable with their respective topgates. To follow the description and ease the distinction of the QD systems, a color code is introduced. Red is assigned to everything connected to QD1 and green is attributed to the elements of QD2. The basic experiment is to apply an $V_{ac} = 5 - 10\ \mu V$ to the superconductor and to measure simultaneously the currents I_1 and I_2 through the respective QDs. The independent tunability of the two QDs allows now to explore correlations in the *linear*

[5] Testing the measurements at different frequencies allows to exclude certain artifacts as the source of the observed signal.

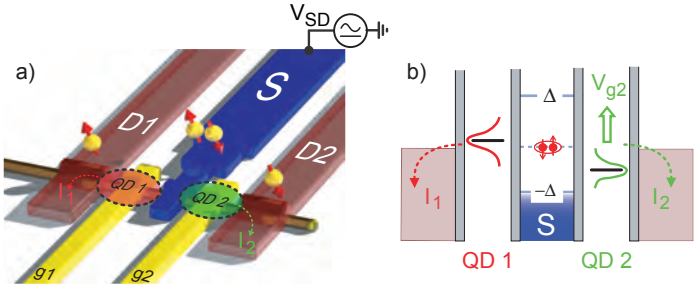

Figure 6.5: *a) The schematics of the lithographically defined structure of the Cooper pair splitter device. b) In the non-local measurement V_{g1} is first set, positioning the eigenstate in QD1 at a fixed value. Then, the change ΔG_1 of the linear conductance through QD1 is measured, while varying the position of the eigenstate in the other quantum dot, QD2, through V_{g2}.*

conductances $G_{1,2} = I_{1,2}/V_{ac}$ between the two QDs. Specifically, it is studied how G_1 of QD1 responds when the level position of the *other* quantum dot, QD2, is varied by the gate voltage V_{g2} (see Fig. 6.5b).

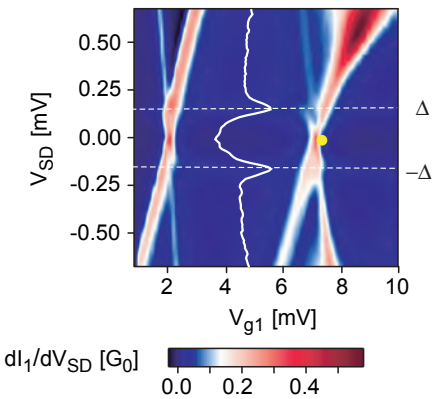

Figure 6.6: *Color plot of the non-linear differential conductance dI_1/dV_{SD} as a function of a dc source drain voltage V_{SD} and gate voltage V_{g1} of QD1, displaying the features expected for a QD in the Coulomb blockade regime. The dashed line is a guide to the eye for the gap energy $\Delta \approx 150\,\mu eV$ of the superconductor. The suppressed electron density-of-state due to the superconductor is clearly visible in the cross-section (white curve) taken in the middle of the Coulomb blockade region.*

Before this "non-local" signal can be measured, the device under investigation needs to be characterized. With the two gate "knobs" (V_{BG} and $V_{g1,2}$) the QDs need to be tuned into a stable Coulomb blockade region. Evidently, superconductivity needs to be present in the chosen region. This can be confirmed by a $G(V_g, V_{SD})$ measurement. If S is present, two distinct peaks at the gap energy $\pm\Delta$ of the S lead should be seen. A typical example of such a measurement is shown in Fig. 6.6. The gap energy is visible (see horizontal dashed lines serving as guides to the eye) at $\Delta \approx 150$ μeV and in the cross-section the suppressed electron DOS due to the superconductor can be seen. From such a measurement, the charging energy can be obtained, being here in the order of $U \approx 2-4$ meV. Furthermore, the tunnel coupling Γ can be deduced. In this specific charge state $\Gamma \approx 0.5$ meV. This state is used to describe the measurement principle in more detail. V_{g1} is adjusted on the resonance with the yellow point in Fig. 6.6 at a stable position. Sweeping TG2 through several resonances the non-local response $G_1(V_{g2})$ in QD1 is obtained. Note, that here the term non-local is used since a change in V_{g2} induces a signal in G_1. This TG2 sweep is repeated several times in order to increase the statistics. E.g. the black squares in Fig. 6.7 correspond to 143 consecutive measurements of $G_1(V_{g2})$. It is done, because the non-local conductance change is only a few percent compared to the background. A

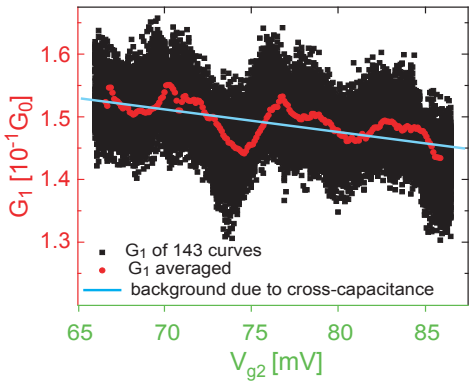

Figure 6.7: *A typical measurement of $G_1(V_{g2})$ is shown when QD2 is swept through 6 successive Coulomb peaks. Here 143 sweeps were performed. If the raw data (black squares) is averaged, a clear signal appears (red dots). The slope originates from a small capacitive coupling between the top-gates of the two QDs. To obtain the final non-local signal (see next section) this background is subtracted from the average of the G_1 measurements.*

single gate-sweep takes typically 100 s. The red curve in Fig. 6.7 is the signal after averaging. A clear non-local signal appears which adds up from the background with a linear slope (defined as $< G_1 >$, blue line) and oscillations around it. This slope originates from a cross-capacitive coupling[6] between the two top-gates of the two QDs. By comparing the linear slope in G_1 vs. V_{g2} with the derivative $\delta G_1/\delta V_{g1}$, the cross-capacitance can be determined quantitatively. It turns out, that the gate-coupling between the two QDs is 1000 times less efficient than the direct coupling. Besides the good leverarm of the top gates due to the vicinity to the respective QDs, it can be assumed that the middle superconductor screens the cross-gating efficiently. After subtracting the background $< G_1 >$ from the averaged signal, the non-local oscillations $\Delta G_1(V_{g2}) = G_1(V_{g2}) - < G_1 >$ become even better visible. ΔG_1 obtained by the above recipe is the subject of the next section.

6.4 Observation of Cooper pair splitting

The data in this section stem from two Cooper pair splitter devices. In the first the QDs are relatively strongly coupled to the contacts, yielding QD levels with a broadening of $\Gamma \approx 0.5\,\text{meV}$ (data presented in Figs. 6.8 and 6.9). In the second the coupling is weaker with $\Gamma \approx 100\ \mu\text{eV}$ (data in Figs. 6.10 and 6.12).

6.4.1 Main results

The main results of such non-local measurements are presented in Fig. 6.8. QD1 is adjusted with V_{g1} to a position off resonance (yellow dot in Fig. 6.6). QD2 is then tuned with V_{g2} through six subsequent charge states, showing Coulomb blockade peaks when a QD level is in resonance (green curves). Simultaneously, the non-local conductance $G_1(V_{g2})$ through QD1 is measured. To better see the change in G_1, $\Delta G_1 = G_1 - < G_1 >$ (red dots) is shown (see section 6.3). When the superconducting contact is driven into the normal state with a magnetic field larger than the critical field, Fig. 6.8a, a small non-local signal is present. For an ideally voltage bias device this is unexpected, since the source acts as a reservoir which injects electrons to both sides independently. Consequently, there should be no non-local correlations. However, the two arms of the Cooper pair splitter are not perfectly voltage biased. The measurement lines have an approximate resistance of

[6] While sweeping TG2, it not only influences the levels of QD2 but to some extent (depending on the *cross-capacitance* between TG2 and QD1) also the ones from QD1.

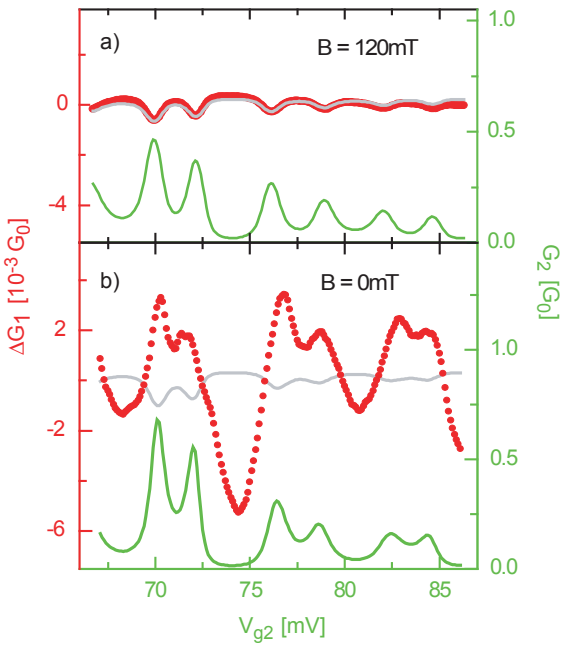

Figure 6.8: *Non-local signal of Cooper pair splitting. Simultaneous measurements of the linear local conductance G_2 of QD2 (green curves) and the linear* non-local *conductance change ΔG_1 of QD1 (red dots) as a function of the gate voltage V_{g2} of QD2 (all conductances are in units of the quantum conductance $G_0 = 2e^2/h$). In the non-local conductance change $\Delta G_1(V_{g2})$ the average conductance of QD1 is subtracted and the signal had to be corrected for a capacitive cross-talk (see section 6.3). The measurements were performed in a magnet cryostat at the base temperature of $T = 20\,mK$. a) In the normal state with a magnetic field $B = 120\,mT$ applied a small negative non-local signal is seen as QD2 is driven through six Coulomb-peaks. This signal is in complete agreement with the expected resistive cross-talk of the measurement configuration (gray line). b) In the superconducting state with $B = 0\,mT$, an order of magnitude higher non-local signal $\Delta G_1(V_{g2})$ is observed. This correlation between the conductances through the two quantum dots is induced by the the superconductor and is due to Cooper pair splitting.*

$R_W \approx 200\,\Omega$[7]. Therefore, in the normal state (resistive) correlations appear: An increase in the current I_2 through QD2 corresponds to a conductance

[7] This resistance is mainly due to the high frequency filtering. For the presented experiment here, only the resistance to the superconductor is of importance (specifically shown in Fig. 6.4).

increase δG_2. Because the larger current I_2 also has to flow through R_W, the voltage at the superconducting source contact has to decrease. This reduces the current I_1, which is then interpreted as a *negative* non-local conductance change δG_1 in QD1. Simple circuit analysis leads to $\delta G_1 \approx -\delta G_2 R_W G_1$, assuming small changes and $R_W << 1/G_1$. The latter condition is easily met, because $1/R_W$ is on the order of $50\,\mathrm{G}_0$, whereas the conductance through the QDs is always smaller than the quantum conductance G_0. These classical correlations contribute always with a *negative* non-local signal[8]. The gray curve in Fig. 6.8a (and in all the other Figures) is the calculated resisitve cross-talk if the two QDs are modeled as resistors and by taking the measurement setup into account. It is in full agreement with the signal in the normal state (red curve).
In contrast, in the superconducting state correlations can appear due to the large coherence length ξ of Cooper pairs, which can exceed the width of the superconducting source contact. Assume that to begin with, the eigenstate in QD1 is near resonance and the one of QD2 is off resonance as for the measurement presented in Fig. 6.8. If the state in QD2 is moved with the gate voltage V_{g2} upwards closer to resonance, not only will pair tunneling through QD2 increase, but also the probability for Cooper pair splitting. The latter induces an increase in G_1. Here, the sign of this non-local correlation is defined *positive* if G_1 shows a conductance increase δG_1 in response to a conductance increase δG_2 in QD2, i.e. $\delta G_1/\delta G_2 > 0$. Thus the signal in Fig. 6.8b is as expected for Cooper pair splitting. This process leads to a ΔG_1 swing of $9 \cdot 10^{-3}\,\mathrm{G}_0$, which corresponds to $6.5\,\%$ relative to the mean G_1 value. Control experiments, like varying the ac frequency in the range of $127 - 400$Hz or detecting the non-local signal in I_2 vs. V_{g1}, yield the same results.

6.4.2 Gate dependence of the Cooper pair splitting

The separate tunability of the two QDs allows to study Cooper pair splitting for different settings of QD1 (Fig. 6.9). As before, first the level of QD1 is positioned. Level positions that are strongly off resonant, intermediate, and on resonance are used. These positions are highlighted by differently colored dots in panel c). To obtain the non-local signal (panel a)), QD2 is swept through two Coulomb resonances (panel b)), while measuring the change ΔG_1. The non-local signal $\Delta G_1(V_{g2})$ strongly depends on the level position of QD1. Away from resonance condition at the side of a Coulomb resonance, the obtained non-local signal is positive (brown and green curves) in agreement with the measurement in Fig. 6.8. However, if the level of QD1

[8] As additional terminology "resisitve cross-talk" is used.

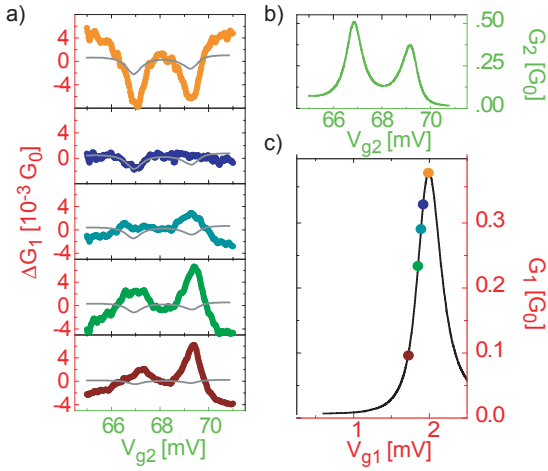

Figure 6.9: *a) The non-local signal $\Delta G_1(V_{g2})$ strongly depends on the level position of QD1 (compare the QD1 position c) and the signal a) with the color code). A transition from a positive to a negative signal is found when QD1 is moved closer to resonance. The gray curves always indicate the expected classical resistive cross-talk. Panel b) shows the two Coulomb peaks through which QD2 was swept while measuring the conductance of QD1.*

is tuned towards a resonance condition, the size of the non-local signal first decreases, then changes sign, becoming maximally negative when QD1 is set exactly to the Coulomb resonance peak (orange curve). Similar results are obtained for different charge states of QD1 and QD2 in several different samples.

6.4.3 Temperature and magnetic field dependence

Fig. 6.10 shows the non-local signal as a function of temperature. Here, QD2 is swept through one Coulomb resonance (lower inset: green curve) and the non-local conductance $\Delta G_1(V_{g2})$ is determined (red squares). The maximum change in $\Delta G_1(V_{g2})$ is normalized to the mean-value of G_1 (grey bar). The temperature dependence of the normalized non-local signal is plotted for QD1 tuned to the left, top, and right side of a Coulomb peak (see upper inset). The non-local signal can be as large as 12 % relative to the mean G_1 value or 2 % relative to the total current at the lowest temperature. With increasing temperature the signal decreases and disappears at around 200 mK independent of the tuning of QD1. This temperature scale is smaller than

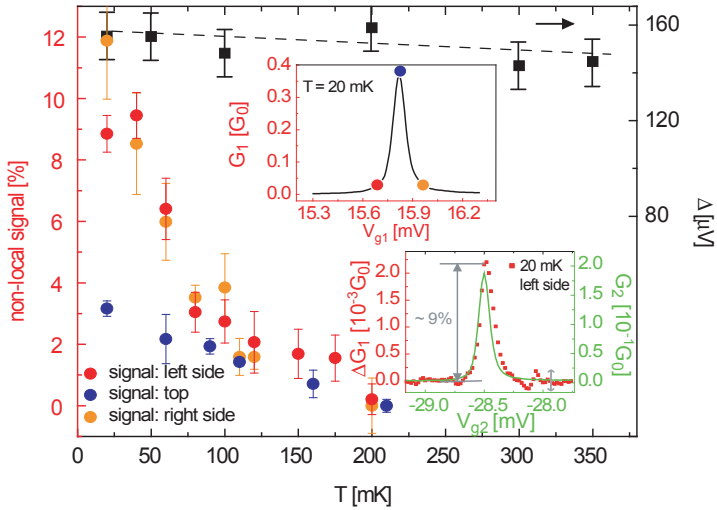

Figure 6.10: *Temperature dependence of the non-local signal for three different settings of QD1(see upper inset). The error bars estimate the read-off error due to fluctuations around the baseline. Independent of the setting of QD1, the non-local signal vanishes around 200 mK, which is well below the superconducting transition temperature $T_C \approx 850$ mK. The evolution of the superconducting gap Δ is shown (black squares) in addition in the main panel (right axis). It is determined from the non-linear differential conductance similar to Fig. 6.6. Lower inset: determination of the non-local signal. As QD2 is driven through a Coulomb-peak (green curve), the height of the peak in ΔG_1 (red squares) is measured (see gray arrow) and normalized by the average value of G_1.*

the critical temperature of the superconductor, $T_C \approx 850$ mK. The superconducting gap $\Delta(T)$ remains approximately constant in this temperature window (black squares in Fig. 6.10). The markedly different temperature dependencies show that the non-local signal is not controlled by the bulk Δ alone. Similar to the temperature dependence is the observed magnetic field behavior of the Cooper pair splitting signal (Fig. 6.11). The non-local signal vanishes at ≈ 45 mT, roughly 30 mT before the superconducting gap vanishes (Fig. 6.11 a,b,c). The observed behavior, as for the temperature dependence, seems independent on the level position of QD1, the QD through which the non-local current was measured. Also at different gate positions (i.e. different QD1 and QD2 resonances) or for different samples the observations were similar. In Fig. 6.11 the same resonance for positioning QD1 is used as for the data of Fig. 6.10. Therefore, it is not surprising that posi-

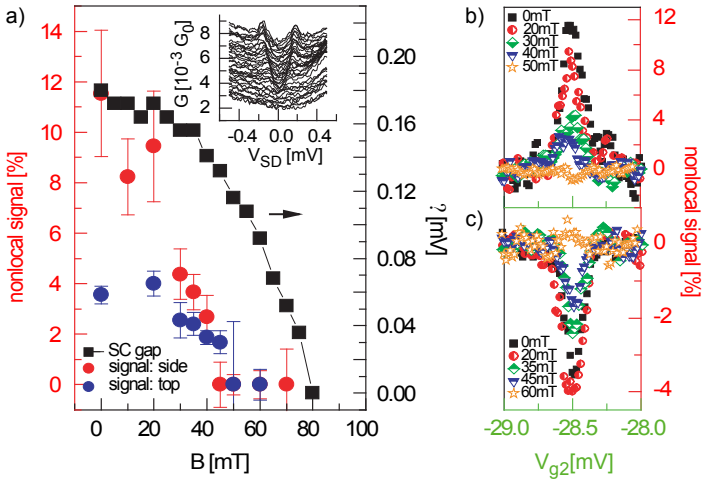

Figure 6.11: *With increasing magnetic field the non-local signal vanishes in non-BCS manner at around 45mT. This behavior is largely independent of the sensor position relative to the resonance and the original size of the signal (side $\cong$ 12 %, top $\cong$ 4 %) as can be seen either in the panel a) where the size of the signal as a function of magnetic field is plotted or in panel b) & c), where single curves of measurements on the side b) and the top c) of a QD1 resonance are shown.*

tioning QD1 at the side of the Coulomb peak (red circles in panel a)) at an average conductance of $\approx 0.02G_0$ the normalized non-local signal at 0 mT was ≈ 12 % (relative to the mean G_1). Additionally, QD1 was also positioned in resonance (blue circles in panel a)), where the normalized non-local signal at 0 mT was ≈ 3.5 % for a G_1 peak conductance of $\approx 0.375G_0$. As can be seen in Fig. 6.11a, the size of the signal diminishes with increasing magnetic field and crosses over into the classical circuit response at $B = 45 - 50$ mT. The observed non-monotonicity, might result from the uncertainty in the measurement, since extensive averaging was needed to obtain the signal (see section 6.3). This is underlined by the big error bars[9]. To further illustrate the magnetic field behavior, in Fig. 6.11b,c, a selection of non-local signals for both QD1 positions (side of resonance in panel b), top in panel c)), at different magnetic fields, are shown. The magnetic field data are consistent with the temperature dependence of the Cooper pair splitting: the bulk superconducting gap is not the dominant term for the observed non-local

[9] As shown in the lower inset of Fig. 6.10 by the light gray arrow, the error bars are determined from the baseline fluctuations of the QD1 measurement.

signal.

6.5 Discussion

The data can be understood qualitatively in a picture of non-interacting particles where the QDs are described by the transmission probabilities T_1 and T_2. The validity of this model is restricted to $T_i \ll 1$ [135]. In this case Cooper pair splitting is proportional to $p(\delta r)T_1T_2$, where $p(\delta r)$ accounts for the probability of finding the two electrons of a Cooper pair at the opposite sides of the superconducting source contact (see section 6.1). The direct Cooper pair tunneling through QD1 or QD2, on the other hand, is proportional to T_1^2 or T_2^2. Thus, the total conductance through QD1 is given by $G_1 \propto \alpha_1 \cdot T_1^2 + p(\delta r) \cdot T_1T_2$ and through QD2 by $G_2 \propto \alpha_2 \cdot T_2^2 + p(\delta r) \cdot T_1T_2$. Since $p(\delta r) << 1$, in a very good approximation, T_2 can be expressed by G_2, i.e. $T_2 \propto G_2^{1/2}$. Consequently, the Cooper pair splitting induced non-local

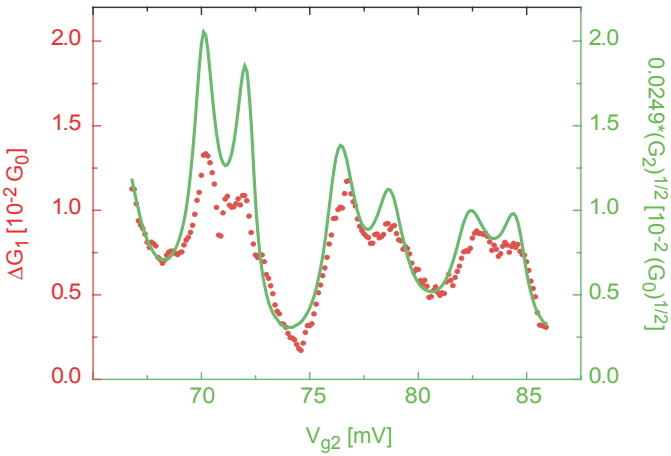

Figure 6.12: *In this figure the validity of the proposed non-interacting picture is analyzed. Assuming low transmission probabilities for electron tunneling through both QDs, the non-local signal $\Delta G_1(V_{g2})$ (red dots) is solely due to Cooper pair splitting and should scale proportional to $G_2^{1/2}(V_{g2})$ (green curve). The good agreement demonstrates that Cooper pair splitting indeed dominates the non-local signal provided the conductance values through the QDs are not too large ($G_{1,avg} \approx 0.149\ G_0$ and $G_{2,min} \approx 0.015\ G_0$).*

signal, $\Delta G_1 \propto T_2$ is proportional to $G_2^{1/2}$. In Fig. 6.12, the gate dependencies of ΔG_1 (red dots) with a scaled $G_2^{1/2}$ (green curve) is compared. The

two curves show a very good agreement for low conductance values supporting the validity of this simple argument. Discrepancies at high conductance values demonstrate, that more elaborate model calculations are required to describe the physics close to the resonance situation of the QDs. This is further underlined by the measurement shown in Fig. 6.9. The non-local conductance in a simplified model is proportional to $p(\delta r) \cdot T_1 T_2$. Thus, the signal is expected to be positive. However, as seen in Fig. 6.9, the non-local signal strongly depends on the level position of QD1. Even negative signals have been observed. This is less surprising than at first sight. On resonance the conductance is large, thus the sign change emerges from a competition of pair tunneling and pair splitting in a regime which is beyond existing theories. The measurements close to resonance strongly contrast the ones off resonance where the measured non-local signal has the expected positive sign in agreement with Cooper pair splitting.

So far the splitting efficiency has been neglected in the discussion of the results. Although the observed Cooper pair splitting can be described to a good extent by this simple model, it can not account for the relatively large signal. As described in section 6.1, $p(\delta r)$ depends on the separation of the two tunneling points δr[10], on the coherence length ξ, the Fermi wavevector k_F and the mean free path l and is in the here presented devices in the order of $\approx 5 \cdot 10^{-6}$. In order to reconcile the very small predicted Cooper pair splitting with the experimental observation, the following explanation is proposed: The tunneling into the two QDs does not occur at the periphery of the superconducting contact. The Cooper pairs rather tunnel into the segment of the semiconducting nanowire underneath the superconducting contact. Because of the low carrier density and correspondingly low k_F, the term $p(\delta r)$ can become much larger, which might be further enhanced by the confined geometry, as described in section 6.1. Such an explanation could account for the remarkable contribution of split Cooper pairs found in the measured samples, considering the macroscopic width of the superconducting contact. It should be noted that in other experiments the expected suppression due to the small value of $p(\delta r)$ seems inactive as well [88, 132, 134, 108]. In none of these works is this issue addressed directly. For the metallic structures used by Ref. [88, 132, 134] a strong decay of the Cooper pair splitting with increasing width w (a factor 20 from $w = 15\ nm$ to $w = 50\ nm$) of the superconducting contact has been observed [132]. However, the behavior of the suppression of the non-local signal in these devices is not in agreement with the predictions of Ref. [9, 58] (see section 6.1). Moreover, it seems that for these experiments the only relevant term in

[10] For an estimate of $p(\delta r)$, the width of S is used for δr. However, this only an upper bound, since the exact tunneling points are not known.

$p(\delta r) \sim 1/(k_F \delta r)^2 exp(-2\delta r/\pi\xi)$ is the exponential decay as a function of δr. In the same geometry as the experiments presented in this chapter, but with carbon nanotubes instead of InAs NWs, Herrmann *et al.* [108] have found a Cooper pair splitting efficiency of up to ≈ 50 %. In their work the splitting was not directly measurable. Instead, due to the rather strong inter-dot coupling, they were able to compare the transport through an anti-crossing in the normal state to the one in the superconducting state. By fitting the data to an elaborate model, which accounts for the different possible tranport channels, the amount of Cooper pair splitting was deduced. In their experiment, the largest tunnel coupling was Γ_{12}. Therefore, probably not $p(\delta r)$ was determining the limit of the splitting efficiency but the interdot coupling. Nevertheless, all the experiments (including the one shown in this chapter) suggest, that the prefactor $p(\delta r)$ is inactive or has to be modified to account for the measurement outcomes.
If this prefactor is not active, it is valid to ask why the splitting efficiency has not been higher in the presented experiments. First of all, it should be noted that although in Cooper pair splitter devices based on two quantum dots, the efficiency can in principle be as high as 100 %, already the here shown efficiencies of a few percent is many orders of magnitude higher than what is achieved in the most efficient production of entangled photon pairs by parametric down conversion (PDC). There an efficiency of only $\approx 10^{-12}$ could be reached [136]. Furthermore, the tunnel coupling Γ of the measured devices was in the order of the superconducting gap Δ. As pointed out in section 6.1, in particular by inequality 6.3, the main conditions for the most efficient Cooper pair splitter is $U \gg \Gamma$ and $\Delta \gg \Gamma$. In the here presented devices $U \gg \Gamma \sim \Delta$. Thus only the first condition is fulfilled. This shows the potential to further improve the efficiency of such devices by using more opaque tunneling barriers, which is the subject of the next section.

6.6 Approaches to optimize the splitting efficiency

A major drawback of the presented devices is the rather large values of Γ. With the achieved minimal coupling of the measured devices, i.e. $\Gamma \approx 100 - 150\mu$V, it is impossible to fulfill $\Delta \gg \Gamma$ (see inequality 6.3). However, for efficient CPS splitting this is a necessary condition. In this section, this issue is addressed in more detail, by providing possible solutions and first experimental results to optimize the device parameters towards $\Delta \gg \Gamma$.

6.6.1 Replacing aluminum by niobium

A simple workaround the problem of rather small tunnel barriers is to increase Δ[11]. A natural choice is niobium with its bulk gap of $\approx$ 1.5 meV [137] roughly ten times larger than the aluminum one. This would open a broad range of suitable and experimentally attainable Γ's. Additionally, Nb is available in an in-house sputtering machine. Two terminal devices were fabricated with standard e-beam technology. In contrast to most other experiments, the native oxide on the nanowires was removed by NH_4S_x passivation before the contact material (Ti (5 nm)/ Nb (90 nm)) was deposited. Although QD behavior was observed in most of the devices, no signatures

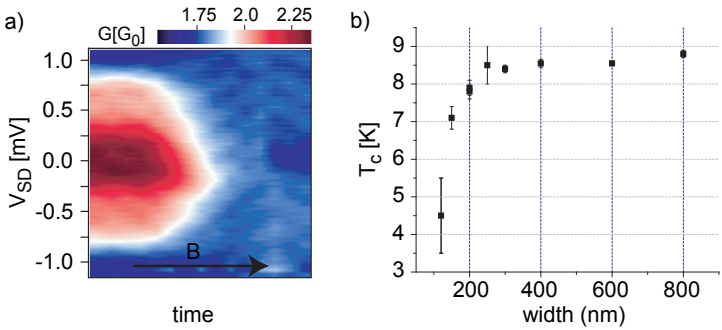

Figure 6.13: *a) A $G(V_{SD}, B)$ measurement on a NW contacted with two niobium contacts ($w \approx 280$ nm) separated around 300 nm. A conductance increase in a bias window of ≈ 1.6 mV at $B = 0$ mT is observed, which diminishes with increasing field (at $\approx 250 - 300$ mT). The feature can be viewed as a possible signature of superconductivity. b) Four-point measurements of the critical temperature T_c of niobium stripes with various width. For wide stripes the measured T_c is roughly in agreement with the literature value of $T_c = 9.2$ K [137]. However, below 200 nm, a drastic decrease is observed.*

of the superconducting proximity effect was seen in the Coulomb blockade regime. However, as visible in Fig. 6.13a, a signature of superconductivity was observed in the regime where conductance fluctuations dominate the transport behavior (i.e. $G \geq G_0$). In the $G(V_{SD}, B)$ measurement an increase in conductance is observed within a bias window of $\approx$ 1.6 mV, as expected from the BTK model for transparent tunnel barriers [57]. The estimated Δ is ≈ 400 μeV. This discrepancy with the bulk value might result from the small width of the contacts ($w \approx 280$ nm) and how the supercon-

[11] The downside one has to be aware of, is a decrease of the coherence length ξ in S with larger Δ.

ductor couples to the nanowire. Supporting measurements are presented in Fig. 6.13b. Measuring the transition temperature of niobium strips with various width, a strong decrease of the critical temperature with decreasing contact width is observed. The width of the contact should be smaller than ξ, otherwise Cooper pair splitting becomes strongly suppressed [9]. In this contact width range, Δ was not as large as expected in the regime of conductance fluctuations and in the closed QD no signatures of the proximity effect were seen. Therefore, this approach has not been pursued further .

6.6.2 Tuning the tunnel barriers

Another possibility to achieve $\Delta \gg \Gamma$ is to increase the tunnel barriers. The tunnel barriers were thought to depend strongly on the thickness of the native oxide layer on the InAs NWs. However, the argon sputtering time does unexpectedly not influence the coupling to the QDs. This indicates that not the metal-oxide interface is responsible for the tunnel barriers. Therefore other approaches were investigated to define controllably the tunnel barriers and the therewith connected QD formation in InAs NWs.

Electrostatic tuning of the tunnel barriers

A possibile approach is to use topgates to define electrostatically the confinement potential in the nanowire[12] [34, 27]. This is illustrated in Fig. 6.14a. The yellow stripes indicate the topgates, enclosed by the Ohmic contacts. By applying appropriate gate voltages $V_{g1,g2}$, the tunnel couplings $\Gamma_{1,2}$ can be tuned. To decouple the topgates from the NWs two methods exist: Either one uses the native oxide of the nanowires or deposits an additional oxide layer (e.g by atomic layer deposition). It is easier to use the native oxide. However, for the Cooper pair splitter devices it is favorable to have the QDs close to the superconducting contact[13]. This is problematic, since placing the topgates as close to the ohmic contacts as possible comprises delicate alignment steps during e-beam lithography. Although improvements were made, the alignment precision remains in the order of 30 nm, which is often insufficient. A shift away from the contact may lead to unwanted QD formation between the ohmic contacts and the topgate. In the other extreme it may happen that the topgates and the contacts touch each other, giving rise to shorts. Therefore an additional fabrication step is introduced to isolate the ohmic contacts from the topgates. Using atomic layer deposition

[12] Most of the here presented work on the use of topgates for barrier tuning has been performed by S. d'Hollosy during his masterthesis [27], supervised by the author.

[13] This can be important for CPS since superconducting correlations do not enter into the NW for distances longer than ξ. In addition, for generated EPR pairs the ´´long-distance" transport within the nanowires might spoil the desired correlation.

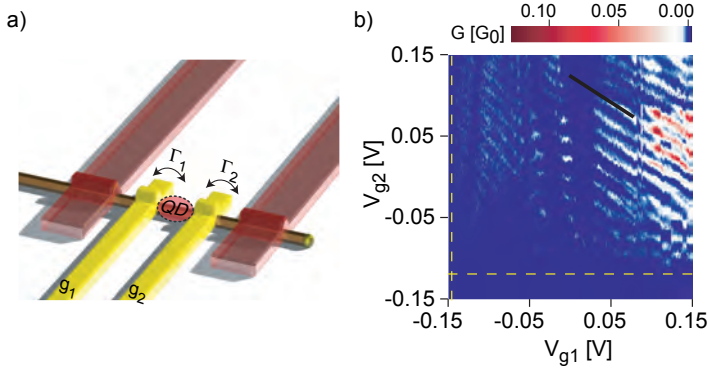

Figure 6.14: *a) Illustration of a two-terminal device with two topgates (yellow stripes). The topgates can be used to define the confinement potential in the nanowire for the controlled formation of a QD. b) $G(V_{g1}, V_{g2})$ measurement on a device as illustrated in panel a). The dashed yellow lines indicate the pinch-off voltage for each topgate. Taken from [27].*

(ALD), thin reliable Al_2O_3 layers can be deposited [27]. Depositing 5 nm Al_2O_3 after contact evaporation, allows an overlap of the topgates with the contacts, in contrast to the topgate fabrication with the native oxide layer. The breakdown voltage of these layers was tested to be on the order of 8 V. But also with the additional isolation layer it is necessary to have a good alignment during lithography. Again, placing the topgates too far from the contacts can lead to QD formation and the topgates get too well screened if most of the surface is over the ohmic contacts. The ALD layers also seem to induce lots of noise.

Nevertheless, measurements have been preformed proving the basic functionality of the topgate approach. In Fig. 6.14b a $G(V_{g1}, V_{g2})$ scan on a topgated NW device is shown. At adequate V_{BG} and topgate voltages, a quantum dot forms between the topgates[14]. The associated charge states are visible as diagonal lines. Additionally, a superimposed modulation on the V_{g1} axis is visible, probably due to unwanted resonances between a lead and gate g_1. More importantly, a clear pinch-off voltage for both topgates is observed (see dashed yellow lines), similar to the findings of [138], indicating tunnel coupling tuning by the topgates.

[14] A leverarm ratio close to 1 of the two topgates (see black line in Fig. 6.14b) allows to construe a QD formation between the two topgates as expected.

Reducing the tunnel coupling by etching

The other method investigated to define controllable tunnel barriers is based on etching. The mobility of InAs NWs decreases drastically for NW diameters below 40 nm [12]. Therefore, by reducing locally the NW diameter, tunnel barriers can be fabricated [32, 33]. In contrast to the topgate approach the barriers strength would have a fix value unless combined with side-/topgates. For the Cooper pair splitter this is not a significant constraint as long the desired regime ($\Delta \gg \Gamma$) is achieved.

Fabrication processes Having the generation of EPR pairs in mind, it seems favorable to have the etched nanowire piece as close to the contacts as possible. In Fig. 6.15 the two investigated fabrication approaches (process I and II) are illustrated[15]. After NW deposition, they are sulfur passivated and a PMMA mask was defined for etching by e-beam lithography (panel a). It turned out that the etching was only following the PMMA-mask, if sulfur passivation was used. Based on experience, passivating the NW with the NH_4S_x slows the NW etching down, compared to the case where the NW still has its natural oxide layer. Therefore, by removing the passivated layer with RIE after development on the areas exposed during e-beam lithography, etching can be performed at predefined regions. This initial preparation is identical for both etching processes. Afterwards, for process I, the NW gets etched as shown in panel I.b). Etching is done with a diluted piranha solution (see appendix B). However, if the NW has prior to the etching already been contacted (e.g. from a different fabrication step) etching rates differ drastically (it is faster with a factor of 3 or more). After etching, without further processing, the contact material is deposited (panel I.c)). In this manner, perfect alignment between the contacts and the diameter reduced NW segments is achieved. This is illustrated in panel I.d) with the schematic of a complete device. The etched parts are close to the contacts as desired. During the testing phase, process I has been slightly modified. After the etching, the PMMA is removed and the devices are checked in the SEM. Improper etched devices were screened out, avoiding unnecessary time losses. Furthermore, this additional step allowed to create devices with four contacts, two evaporated on etched, respectively unetched NW parts. Such device geometry allows to compare the modification induced by the etching, with an unmodified nanowire segment on the same sample. A drawback of this additional lithography step is the loss of the self-alignment mechanism. However, for testing reasons it is the better choice.
In process II, the material for the contacts is evaporated (panel II.b)) directly following the initial preparation steps (panel a)). After evaporation

[15] For the details of the individual fabrication setups consult chapter 3 and appendix B

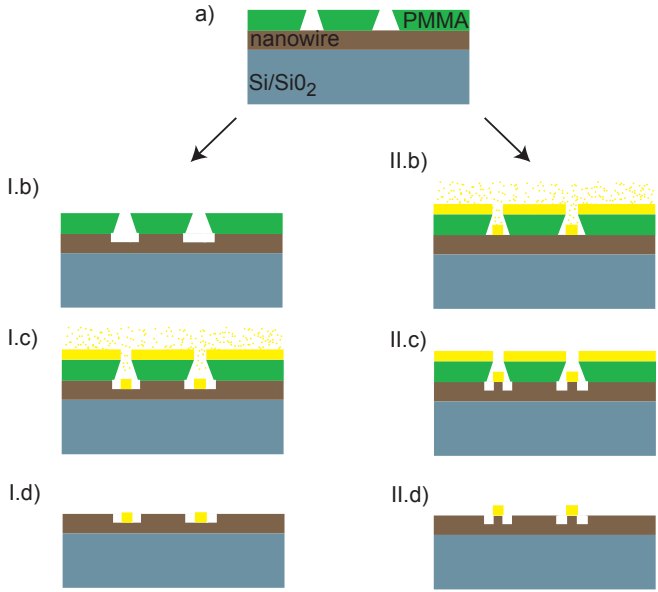

Figure 6.15: *Illustration of the two etching processes I and II approaches to define QD with large tunnel barriers. a) After sulfur passivating the entire NW, standard e-beam lithography is used to define the mask for the etching/contacts. In process I first the NW is etched with piranha solution (b) before evaporating the contact materials into the etched NW segments (c). At the end the lift-off is performed (d). In process II the order of the etching and evaporation process are reversed compared to process I. This is more elegant and has the advantage that the contacts are placed on unetched parts of the NW.*

the sample is put into the RIE to remove the sulfur bonds in the undercut from the earlier performed NH_4S_x passivation. Before the lift-off is done, the etching is made with the same piranha solution settings as for process I. It is expected that the piranha penetrates into the undercut and etches the nanowire therefore self-aligned around the contact as illustrated in Fig. 6.15 II.c). Afterwards the lift-off is made to finalize the self-aligned barrier etching process. The advantage of process II over I is that the contacts are placed on unetched NW parts. This ensures better contacts and defines the barrier only to a short segment. SEM images from process I and II are shown in Fig. 6.16a,b and c,d, respectively.

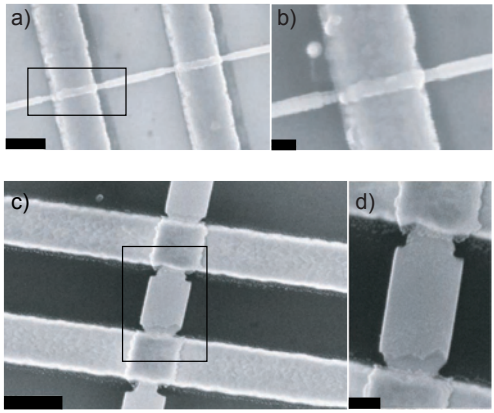

Figure 6.16: *Exemplary SEM images of etched nanowire QD devices fabricated after the two processes presented in Fig. 6.15. The devices in panel a) & b) are fabricated after process I, whereas pictures c) & d) show results from devices made after process II. The black boxes indicate the approximate position of the two zoom-in's in panel b) and d). Scale bars: a) and c) 300 nm, b) and d) 100 nm*

Measurements Unfortunately, fabrication process II has only worked very recently and to-date there are no measurements available. A bit more information is available for measurements on devices fabricated after process I. At room temperature differences between etched and unetched devices are observed. The 2-point resistance is usually higher for the NW segments which are etched than the unetched counterparts on the same NW and strongly varying between different NW samples. At T= 4.2 K the samples often become too resistive to be measured with the used setups. This might be a signature of large tunnel barriers. However, more elaborate samples would be needed to verify this explanation (e.g. similar to Choi *et al.* who uses QPC as charge sensors to observe transport through InAs NW QDs with extreme low tunnel coupling [33]).
Nevertheless, sometimes almost "text-book" quantum dot behavior is observed in etched NW QD systems as shown in Fig. 6.17. In this $G(V_{SD}, V_{BG})$ measurement at T = 4.2 K even the orbital level filling (even-odd effect) was seen. The relatively large charging energy U $\approx$ 4.5 meV and orbital energy of $\delta E \approx$ 5 meV indicate a smaller QD as usually observed for a contact spacings of $\approx$ 270 nm (U $\approx$ 3 meV). In agreement with this considerations is the measured length of the unetched NW piece between the two etched segments ($\approx$ 150 nm is obtained, the diameter is $\approx$ 60 nm which is in the usual range of these NWs). At T= 4.2 K the tunnel barrier was dominated

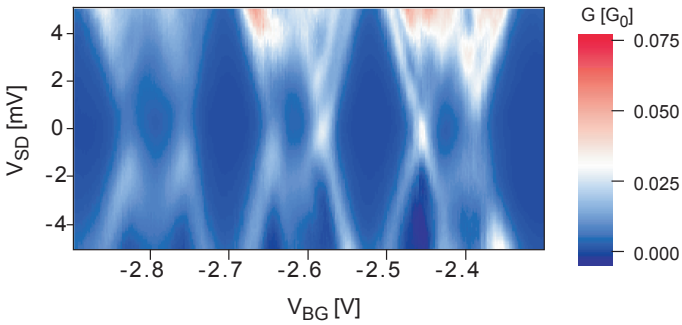

Figure 6.17: *A $G(V_{SD}, V_{BG})$ measurement at $T = 4.2$ K of a QD fabricated after process I. Even-odd behavior is observed. The large charging- and orbital energy indicate a smaller QD system than the contact separation in agreement with SEM images of the device.*

by the temperature, i.e. $\Gamma \simeq k_B T$. This is in agreement with measurements on other devices. To determine Γ in these devices, they should be cooled down to $k_B T << \Gamma$. So far, only one device was successfully cooled down below T= 4.2 K. The sample geometry discussed above allowed the direct comparison between QDs with etched and unetched NW segments on the same NW. In the performed cooldown no significant difference of the tunnel barriers was observed. In both cases Γ/k_B was in the order of ≈ 6 K. However, the indistinguishability between the non-etched and the etched QD show that further optimizations are necessary and the device probably did not work as desired. In addition, more statistics are necessary to make conclusive statements and measurements on "process II" samples need to be performed.

Etching with focused ion-beam A different method to etch trenches into the NW at well specified locations to define controlled tunnel barriers and quantum dots can be accessed by using a highly focused Gallium ion-beam (FIB)[16]. Originally the FIB was considered as effective method to cut the NW into two pieces. Evaporating the superconductor from the Cooper pair splitter devices onto this trench should eliminate the interdot coupling (see section 6.1), another possible disruptive factor for efficient pair splitting. Although not expected, a weak interdot coupling for the Cooper pair splitter devices presented in this chapter, can not fully be excluded. Complete

[16]The milling with the FIB is done in Budapest by collaborators in the group of Sz. Csonka.

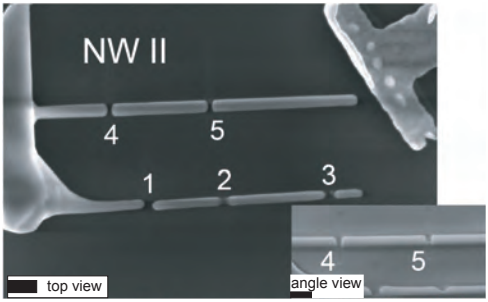

Figure 6.18: *InAs NW milled with a focused Ga ion beam. The NW can be completely cut (1,3,4,5) or only partially (2). Both have application possibilities within the framework of optimizing the Cooper pair splitter devices. Cutting the NW completely below the superconducting electrode allows to overcome the drawbacks of possible interdot coupling. By only reducing the NW diameter at specific locations it might be possible to define QDs with fix large tunnel barriers. Scale bar for both images: 200 nm.*

decoupling is desirable. To date no measurements have been performed with Cooper pair splitters where the two QDs have been fully decoupled or on two terminal QD systems with FIB milled tunnel barriers. But recent fabrication progress (see Fig. 6.18) indicate that probably soon experimental results on FIB cut NWs will be available.

6.7 Summary and outlook

In conclusion, tunable Cooper pair splitter devices, based on an InAs NW two-quantum dot Y-junction, are demonstrated. This device geometry allows a direct observation of Cooper pair splitting in non-local current measurements and is a first important step towards studying entanglement of spatially separated mobile electrons. If further measurements prove the entanglement of such split Cooper pairs in these devices, they can be used as source of on-chip generated entanglement, e.g. for quantum computation.
In section 6.4 the main results are presented. From these measurements the deduced contribution of split Cooper pairs to the entire current is a few percent. However, as mentioned in section 6.5, in comparison to the production of entangled photon pairs by parametric down conversion (PDC), the efficiency is magnitudes higher [136] in the here presented devices. And considering theoretical predictions [9], the observed efficiency is quite re-

markable, as discussed in section 6.5. Nevertheless, for an useful EPR source an efficiency close to unity is desirable e.g. for a Bell inequality test. This is possible if the theoretically proposed prefactor for the splitting efficiency (see sections 6.1, 6.4 & 6.5) is inactive as recent experiments seem to indicate [88, 132, 134, 108, 107]. In the devices based on Coulomb interaction in quantum dots and superconductivity, such as [108] and [107], two major problems exist. As discussed in sections 6.1 & 6.5, one is the fact that the lifetime broadening of the QDs, $\Gamma_{1,2}$, can be in the order of the superconducting gap Δ, i.e. $\Gamma \geq \Delta$. In this case, direct pair tunneling is not sufficiently suppressed. The other one is the interdot coupling, limiting the efficiency to a maximum value of 50 % [108]. For both issues, possible solutions and first advances into their realization are presented in section 6.6. A schematic of an optimized Cooper pair splitter is presented in Fig. 6.19. However, there

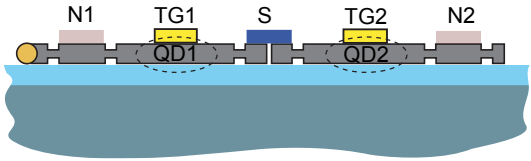

Figure 6.19: *Illustration of an optimized device. Etched trenches next to contacts lower the tunnel coupling* Γ *to values well below the superconducting gap. In addition the NW is cut into two pieces below the superconductor to eliminate possible interdot coupling. By courtesy of G. Fülöp*

are still open questions. One is the missing experimental evidence of the probability factor for Cooper pair splitting. This aspect is already treated in section 6.5. Additionally, the strong suppression of the non-local signal with temperature (Fig. 6.10) and magnetic field (Fig. 6.11), well before any significant effect on the superconducting gap is observed, is still puzzling and needs further investigation. Furthermore, a negative signal is measured if the QD which is held fix, is positioned on resonance (Fig. 6.9). This negative signal emerges from a competition of pair tunneling and pair splitting in a regime which is beyond existing theories. Thus, further theoretical work is needed to account for it.

Only the very first step has been achieved in the recent experiments on Cooper pair splitting [108, 107] towards an efficient EPR pair source. Thus, in the remaining part of this section an outlook on the needs to realize such an EPR source, is given. One of the major requirements for all experiments (independent of the device material) will be the ability to increase the efficiency. Possible approaches have been outlined in section 6.6, including Γ tuning, eliminating the interdot coupling and the use of superconductors

with large Δ. In parallel, means of assessing the Cooper pair splitting have to be developed further. In the presented InAs NW based experiments it has been done directly by measuring the non-local correlations in the linear conductance of the two QDs. Herrmann *et al.* have used an indirect approach in the carbon nanotube experiments by fitting the experimental data to a model, allowing to extract the amount of Cooper pair splitting in respect to other processes [108]. Another method is accessible if the requirements for small level broadening of the QDs has already been achieved. In this case an energy filtering for the Cooper pair splitting can be obtained by applying a small dc bias voltage $\Delta\mu$, with $\Delta > \Delta\mu > k_B T$ (see also section 6.1.2). If the energy levels of the QD are equal but opposite ($\epsilon_{d1} = -\epsilon_{d2}$) Cooper pair splitting is allowed whereas for other QD level configurations it can be suppressed. For such experiments, the setup shown in Fig. 6.5 would have to be expanded so that each QD could be biased separately. First measurements with a setup allowing for this individual bias tunability are presented in chapter 7.

An alternative approach is to measure the correlation of the current fluctuations, i.e. noise, between the two leads [139, 121, 140]. It is apparent that there could be processes (e.g. Cooper pair splitting) which enter in the timeframe of the measurement simultaneously in each contact, giving raise to positive cross-correlation. Similarly, if a Cooper pair tunnels through the same contact, negative cross-correlations are expected. Thus, detecting positive noise cross-correlation between the two arms would be a proof for charge correlations between the two leads [121]. However, detecting a positive signal in such noise measurements is not a proof of entanglement. For this, a beam-splitter geometry would be required, where two possible electron path's are interfered in a "beam-mixer" and afterwards the noise correlation is detected [141]. Since a Cooper pair is a spin-singlet, the orbital wavefunction is symmetric under exchange of the particles. This makes the two electrons "bunch" together upon leaving the beam-mixer if their correlation is preserved. This simultaneous leaving into the same lead can be observed in the noise-correlation measurement which accesses the spatial part of the wavefunction [142]. However, in the rather rigid InAs NWs such an interference experiment seems not feasible and is therefore not further discussed. Another possible proof of entanglement is obtained by violating Bell's inequality (Eq. 6.2). In theoretical proposals the combination of tunable ferromagnetic contacts with noise correlation measurements is put forward as possible realizations of Bell state measurements in Cooper pair splitters [143, 144, 120, 145]. Besides the difficulties considering noise measurements, to be able to measure the Bell inequalities, several fabrication challenges arise. For the required spin-projections, reliable ferromagnetic single domain contacts need to be fabricated. Considering the large diam-

eter of InAs the arising challenge is obvious. For this purpose CNTs are more promising (see e.g. recent tunnel-magneto-resistance measurements in CNTs [146, 147]). Yet, for Bell tests not only collinear alignment between the different contacts are needed. A possible solution is to use disk shaped synthetic antiferromagnets which can be aligned in any direction. Another possibility is to exploit the spin-orbit interaction, similar to the Datta-Das proposal [148]. Gate-tunable spin-orbit interaction would allow to rotate the spins into a certain orientation, making the need of non-collinear F contacts obsolete [141]. This is a promising approach for InAs NW structures with their strong intrinsic spin-orbit coupling. Recently it has even been put forward that noise correlations are not sufficient to prove entanglement. Instead fourth order cumulants need to be recorded [149]. A challenging goal!

CHAPTER 7

Finite bias Cooper pair splitting

Having realized a Cooper pair splitter and exploited the possibilities of the linear conductance regime (chapter 6) it is only natural to take advantage of additionally available parameters. This is the subject of the present chapter. The non-local conductance in one quantum dot (QD) of an InAs nanowire based Cooper pair splitter is investigated, while the other is biased by a finite voltage on the normal metal contact. In a superconductor coupled to two QDs in parallel, the bias on one lead provides an additional parameter that allows to perform spectroscopy and gain more control over the relevant higher order tunneling processes detected on the other QD. The electrical transport through the device can be dominated either by Cooper pair splitting (CPS) or by elastic co-tunneling (EC). In this chapter preliminary results indicate that if the device is operated at finite bias the relative rates of these non-local processes can be tuned by exploiting the gate dependence of the level energy and the density of states at the relevant energies.

7.1 Introduction

The electrons in a Cooper pair of a conventional superconductor form a spin singlet. If the electrons can be separated coherently, this might be exploited as a naturally occurring on-chip source of entangled Einstein-Podolsky-Rosen (EPR) pairs [10] of electrons. This Cooper pair splitting (CPS) process can be understood as inverse crossed Andreev reflection and

was initially searched for in metallic nanostructures with tunnel contacts [88, 132, 150, 134]. However, other higher order processes like elastic co-tunneling (EC) make the detection of CPS difficult. Electron-electron interactions are crucial to discriminate between theses processes, but in these metallic structures such interactions can not be tuned by external means. It has been suggested to use electrically tunable quantum dots (QDs) coupled to a superconducting lead to obtain such tunability [9, 125] which has recently been realized in zero bias transport measurements on InAs NWs (see chapter 6) and carbon nanotube QD devices [107, 108].
In metallic structures, possible signatures of CPS at finite bias were attributed to the excitation of different modes of the electromagnetic environment by the tunneling electrons [132, 151, 134]. This mechanism, however, is difficult to control experimentally. Using similar InAs nanowire devices as in chapter 6, measurements are shown which indicate that the finite bias differential conductance through one QD is not completely due to local processes, but also contains non-local higher order tunneling processes, like CPS and EC. The latter will be analyzed in more detail.

7.2 Device fabrication and measurement setup

First, high quality molecular-beam epitaxy grown InAs nanowires (NWs) are deposited from an isopropanol solution on highly doped Si wafers with a 400 nm insulating SiO_2 barrier layer. After localization with an optical microscope the device is further processed by standard e-beam lithography techniques. A superconducting (S) contact (blue stripe in Fig. 7.1) with an width of $\approx$ 200 nm is fabricated on the NW. It is made such, that the S lead could be contacted from both sides. This allows, by performing 4-point measurements, to exclude material issues as possible error source if no S correlations are visible in transport experiments. In addition to the superconducting source, Ohmic drain contacts (light red, w $\approx$ 300 nm) as well as top-gates (yellow stripes, w $\approx$ 150 nm) are put on the NW. The top-gates are isolated from the NWs by their native surface oxide layer. In-situ argon sputtering is used to remove the oxide layer (see appendix B for parameters) for the source and drain contacts.
Measurements are performed in a dilution refrigerator at a base temperature of $\approx$ 20 mK with the option of applying a magnetic field perpendicular to the wire axis. The detailed electronic setup is shown in Fig. 7.1. An ac voltage source with a frequency of $f = 77\,\mathrm{Hz}$ is applied to the S contact. It is attenuated to an amplitude of $V_{ac} = 10\,\mu\mathrm{V}$ by passive voltage dividers. Lock-in techniques are used to measure the differential conductance $dI_{1,2}/dV$ through each QD separately. On both leads a dc bias can

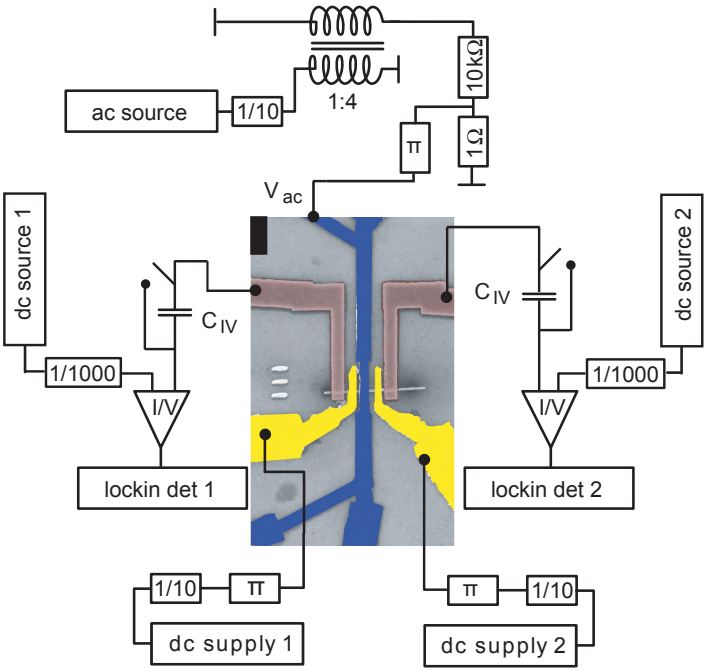

Figure 7.1: *An SEM image of a device with the details of the measurement circuit. The measurements were performed a dilution refrigerator at a base temperature of* 20 *mK. Two confinement potentials (i.e. QDs) are forming between the superconducting (S) source (blue) and the drain leads (light red). They are individually tunable by dc gate voltage supplies (V_{g1} and V_{g2}). S is ac biased whereas the dc voltage was superimposed by applying voltages at the offset input of the I/V converters for each QD separately. If only the linear conductance was assessed, a capacitor C_{IV} was switched to the I/V input. For the ac measurements standard lock-in techniques were used. The measured ac currents I_1 and I_2 through the two QDs are converted to voltages by home-built I/V converters (gain* 10^8 *V/A) and then detected with lock-in amplifiers. Scalebar corresponds to 1 μm.*

be applied at the offset input of the home-built current-voltage I/V (gain of 10^8 V/A) converters. If necessary, dc biasing from the I/V converters can be eliminated by coupling a capacitor $C_{IV} = 10\ \mu F$ to the I/V converter input at both Ohmic contacts.

7.3 Measurement principle

In Fig. 7.2a a close-up of the device and the measurement scheme is shown. Between the superconducting (S, blue) contact and the metal leads (N_1, N_2, red) two quantum dots QD1 and QD2 are formed. The two top-gates (g_1, g_2, yellow) are strongly decoupled from each other so that the QD levels can be tuned individually, while the highly-doped Si wafer separated from the device by 400 nm thermal oxide serves as a global back-gate.
An ac voltage $V_{ac} = 10\ \mu$V is applied to S at zero dc potential. A dc voltage V_{N2} is applied to contact N2 of QD2, while measuring the differential conductance $G_1(V_{\mathrm{N2}}, V_{\mathrm{g1}})$ through QD1. QD1 is held at $V_{\mathrm{N1}} = 0$ mV. In order to eliminate a possible V_{N1} biasing induced by the offset voltage from the input amplifier of the I/V converter, the latter is capacitively coupled. Fig. 7.2b shows the corresponding energy diagram. QD1 exhibits clear Coulomb peak

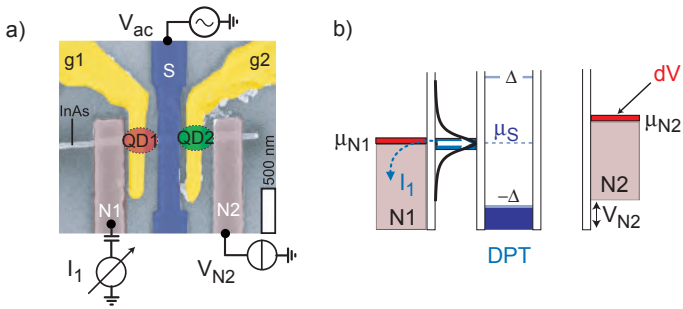

Figure 7.2: a) Illustration of the non-local measurement scheme, placed on an SEM image close-up of a typical device. b) Schematic of direct Cooper pair tunneling with an ac voltage V_{ac} imposed on QD1 and QD2 and a finite bias V_{N2} on QD2.

structures (see below). Therefore the density of states (DOS) of QD1 is represented by a resonant level. For QD2 a constant DOS is assumed (not shown in Fig. 7.2b). In the performed measurements V_{g2} is held fix at a specific voltage and only V_{N2} is varied. At the chosen V_{g2} value, G_2 is only weakly dependent on V_{N2}[1] justifying the used approximation. Furthermore, it is used that adding the ac modulation V_{ac} on the superconductor is equivalent to periodically lowering the voltage on both leads, N_1 and N_2, if we take the chemical potential μ_S of the Cooper pair condensate as reference. This ac modulation is illustrated in Fig. 7.2b by the red areas labeled dV in the leads N_1 and N_2, respectively.

[1] In the voltage range of the measurements the conductance of QD2 changes between $G_2 = 0.05G_0$ at $V_{\mathrm{N2}} = 1$ mV and $G_2 = 0.135G_0$ at $V_{\mathrm{N2}} = -1$ mV.

The largest component of $G_1 = dI_1/dV$ is due to local transport between S and N_1, i.e. direct Cooper pair tunneling (CPT) as shown schematically in Fig. 7.2b. In CPT the two electrons of a Cooper pair tunnel through the same QD into a single lead. Due to time-reversal symmetry this is ("loosely speaking") equivalent to two electrons tunneling from the normal lead into S and forming a Cooper pair[2]. In addition, also electrons thermally excited above the superconductor gap Δ contribute to the local conductance. Because S and N_1 are virtually at the same dc potential, all local transport processes are independent of the bias, V_{N2}. Therefore, only "non-local" transport processes like EC and CPS, which comprise almost simultaneous coherent tunneling of an electron through QD1 and QD2, can exhibit a dependence on the bias applied to N_2 (see below).

7.4 Observation of "non-local" signals at finite bias

Fig. 7.3a shows the differential conductance G_1 of QD1 as a function of the gate voltage V_{g1} of QD1 and the bias applied to QD1, V_{N1}. Clear Coulomb blockade behavior is seen. Superconductivity is present with a gap energy $\Delta \approx 130\,\mu$eV (see horizontal dashed line). Additionally, the tunnel coupling $\Gamma \approx 500\,\mu$eV and the addition energy $E_{add} \approx 3\,$meV can be estimated. The rather large coupling allows for the formation of a Kondo resonance [43] around $V_{\mathrm{g1}} = -0.152$ V. Fig. 7.3b shows $G_1(V_{\mathrm{N2}}, V_{\mathrm{g1}})$ measurement through the same charge states as shown in panel a). Three well-defined peaks (labeled as $1-3$) are observed at the V_{g1} positions corresponding to resonant situations in QD1. The first one is made up of two Coulomb peaks with a Kondo resonance between. Therefore, only the electronic states in-between 1-2 (A) and 2-3 (B) are labeled. Note that on this conductance scale the peaks seem independent of V_{N2}.
Since at a bias well above Δ/e it is expected that all non-local processes become ineffective, $\Delta G_1 = G_1(V_{\mathrm{N2}}, V_{\mathrm{g1}}) - G_1(V_{\mathrm{N2}} = -1\,\mathrm{mV}, \mathrm{V_{g1}})$ is plotted in Fig. 7.3c. Any features in this plot are due to non-local higher order tunneling processes related to the superconductor or its gap (see section 7.3). The colorscale is adjusted so that white is $\Delta G_1 = 0$. For the gate voltage V_{g1} tuned to a resonance in the DOS of QD1 a strong positive non-local conductance is observed with a strength of $\Delta G_1/G_1 \approx 18\%$ on peak 1, $\approx 8\%$ on peak 2 and $\approx 15\%$ on peak 3. Though these maxima are well-localized around zero bias to within about $eV_{\mathrm{N2}} \approx \Delta$, a weak positive signal is still visible at larger bias, possibly resulting from imperfect subtraction of the local

[2]Correctly this process is termed Andreev reflection, where an electron impinges on S and a hole gets retroflected. To conserve charge and momentum, a Cooper pair forms.

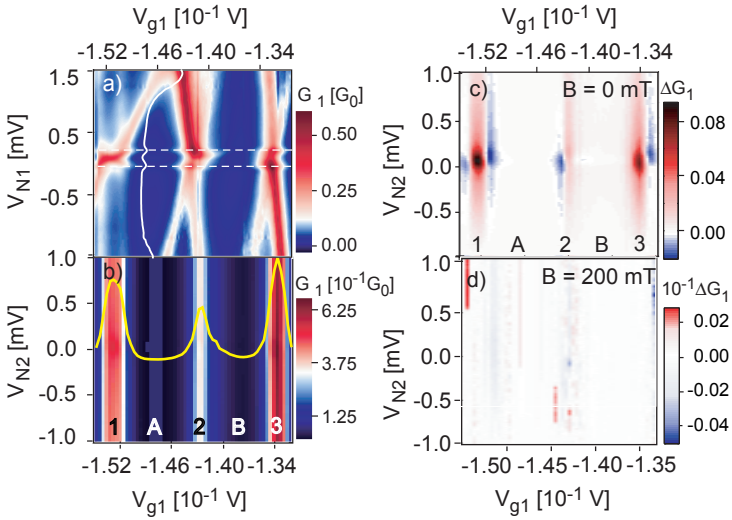

Figure 7.3: a)A $G_1(V_{\mathrm{N1}}, V_{\mathrm{g1}})$ measurement at B= 0 mT. The dashed white (horizontal) line highlight the gap energy Δ. Also a $G_1(V_{\mathrm{N1}})$ cut is shown (white line) where the reduced DOS is visible. b)$G_1(V_{\mathrm{N2}}, V_{\mathrm{g1}})$ at B= 0 mT. A cross section at constant $V_{\mathrm{N2}} = 0$ V is shown in yellow. c) $\Delta G_1 = G_1(V_{\mathrm{N2}}, V_{\mathrm{g1}}) - G_1(V_{\mathrm{N2}} = -1\,\mathrm{mV}, \mathrm{V_{g1}})$ derived from the data in b) for the same parameter range. d) Same plot as in panel c) but derived from $G_1(V_{\mathrm{N2}}, V_{\mathrm{g1}})$ measurements performed at $B = 200\,\mathrm{mT}$. Graphs are slightly off-set from zero $V_{\mathrm{N1,N2}} = 0$ due to an I/V converter induced voltage offset.

conductance or not fully suppressed non-local processes. With V_{g1} slightly off-peak, a well-defined dip in ΔG_1 is observed on both sides of peak 1 and to the left of peak 2 and to the right of peak 3 (see blue regions). Further away in the gate voltage from the peaks, small zero-bias dips in ΔG_1 can be observed in the entire V_{g1} range (see e.g. Fig. 7.4g). In Fig. 7.3c these features are not clearly visible because they are much smaller than the main structures in the plot. The strength of these dips depend on V_{g1} and can be as large as $\Delta G_1/G_1 \approx 10\%$.

As a control experiment superconductivity is suppressed by an external magnetic field of 200 mT applied parallel to the Al strip. The corresponding plot of ΔG_1 is shown in Fig. 7.3d. Even on the considerably smaller scale of Fig. 7.3d no features comparable to the ones observed in Fig. 7.3c can be discriminated. Therefore, it can be concluded that the features in Fig. 7.3c are due to the superconductor and non-local transport processes.

Fig. 7.4 shows $\Delta G_1(V_{\mathrm{N2}})$ cross sections of Fig. 7.3c at a series of constant

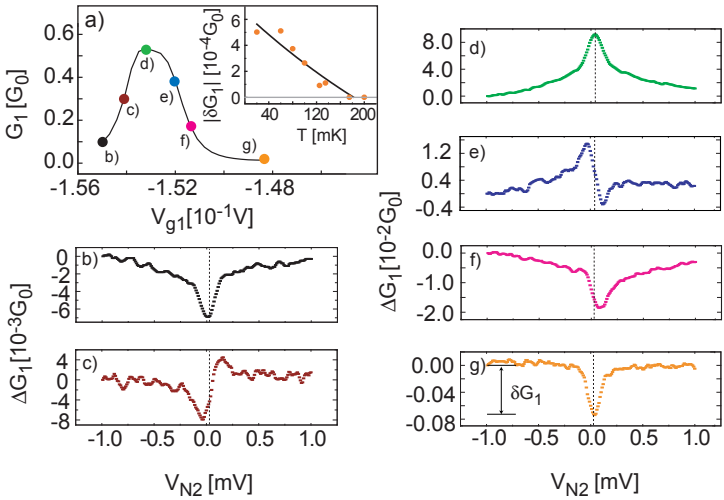

Figure 7.4: a) $G_1(V_{\mathrm{N2}} = 0\ \mathrm{mV}, V_{\mathrm{g1}})$ scan over the first resonance with $\Delta G_1(V_{\mathrm{N2}})$ slices (b-g) marked by colored spots. Clear non-local signal is observed. The dashed line in the $\Delta G_1(V_{\mathrm{N2}})$ corresponds to $V_{\mathrm{N2}} = 0$ if the I/V converter induced voltage offset is taken into account. Inset: Temperature dependence of the non-local signal, measured close to the orange spot. See the corresponding $\Delta G_1(V_{\mathrm{N2}})$ slice on how the signal is deduced. It is strongly decaying with T, vanishing completely for T = 175 mK. The black line serves as guide to the eye. In this temperature window no significant changes in the superconducting gap are observed.

V_{g1} voltages near peak 1, as illustrated on a $G_1(V_{\mathrm{g1}})$ sweep in Fig. 7.4a. The bias dependence of ΔG_1 shows a pronounced dip at zero bias on both sides of the resonance, as shown in Figs. 7.4b and g, while on resonance a strong peak is observed, see Fig. 7.4d. Zero bias on the device is indicated by a dashed vertical line in all plots. Having the QD1 DOS near, but not completely in resonance the bias dependence is *asymmetric* with respect to zero bias: at the gate voltage of Fig. 7.4c the V_{N2} dependence of ΔG_1 exhibits a minimum at negative and a maximum at positive bias, while on the other side of the resonance, at the gate voltages of Figs. 7.4e and f, a maximum can be found at negative and a minimum at positive bias. This asymmetry in ΔG_1 is also found on the left side of peak 2 and on the right side of peak 3.

The non-local signals decay strongly with increasing temperature as shown for the dip in Fig. 7.4g in the inset of Fig. 7.4a, similar to the dependence observed in section 6.4.3 for zero-bias CPS. Here, the temperature depen-

dence of $\delta G = |\Delta G_1(V_{\mathrm{N2}} = -1\,\mathrm{mV}) - \Delta \mathrm{G}_1(\mathrm{V}_{\mathrm{N2}} = 0\,\mathrm{mV})|$ measured at $V_{g1} = -0.1485$ V (close to the orange spot in Fig. 7.4a) is shown. At $T \approx 175\,\mathrm{mK}$ no signal in ΔG_1 can be discriminated anymore. Within the temperature window where the non-local signal vanishes, no significant changes of the superconductor Δ of the Al strip is seen. Therefore, it is concluded that Δ is not the limiting energy scale in this problem, in agreement with the findings in section 6.4.3.

7.5 Discussion

The observed features can qualitatively be understood, by considering the simplest case where only the higher order tunneling processes CPT (Fig. 7.2b), CPS[3] (Fig. 7.5a) and EC (Fig. 7.5b) contribute. In this case the current I_1 through QD1 can be written as [127]:

$$I_1 = (G_{CPT1} + G_{CPS} + G_{EC})V_{\mathrm{N1}} + (G_{CPS} - G_{EC})V_{\mathrm{N2}} \tag{7.1}$$

with G_x being the conductance for the specific transport mechanism. In the experiment the differential conductance $G_1 = dI_1/dV$ ($dV = dV_{\mathrm{N1}} = dV_{\mathrm{N2}}$) for different V_{N2} and $V_{\mathrm{N1}} = 0$ is measured. Thus Eq. 7.1 can be rewritten as

$$I_1 = (G_{CPT1} + G_{CPS} + G_{EC})dV + (G_{CPS} - G_{EC})(V_{\mathrm{N2}} + dV) \tag{7.2}$$

G_{CPT1} does not depend on V_{N2}. Since the experiment focuses on non-local processes, G_{CPT1} is subtracted and $\Delta G_1 = G_{1,\mathrm{CPS}} + G_{1,\mathrm{EC}} = dI_{1,\mathrm{CPS}}/dV + dI_{1,\mathrm{EC}}/dV$ is presented. The non-local ($n.l.$) current can be expressed using Eq. 7.2:

$$I_{1,\mathrm{n.l}} = I_{1,\mathrm{CPS}} + I_{1,\mathrm{EC}} = (G_{CPS} + G_{EC})dV + (G_{CPS} - G_{EC})(V_{\mathrm{N2}} + dV) \tag{7.3}$$

Obviously, for $V_{\mathrm{N2}} = 0$ only CPS contributes to $\Delta G1 = dI_{1,\mathrm{n.l.}}/dV$. For constant DOS this remains true even for $V_{\mathrm{N2}} \neq 0$ (Eq. 7.3). However, the situation is different if the DOS is not constant anymore since G_{CPS} and G_{EC} are energy dependent. The therefore expected modifications are subject of the subsequent part of this section.
First, the situation is considered when the DOS maximum of QD1 is in resonance with μ_{N1} (Figs. 7.5a and b). The DOS in QD2 is assumed to be constant over the relevant energies (section 7.3). Furthermore, any changes in the effective DOS due to the proximity effect are here neglected and it is referred to Ref. [152] for a detailed description of the involved processes. In Fig. 7.5a CPS induced by dV is outlined in red. One can intuitively

[3] CPS is equivalent to the crossed Andreev process (CAR). In the following discussion, it can be helpful to think of CAR instead of CPS.

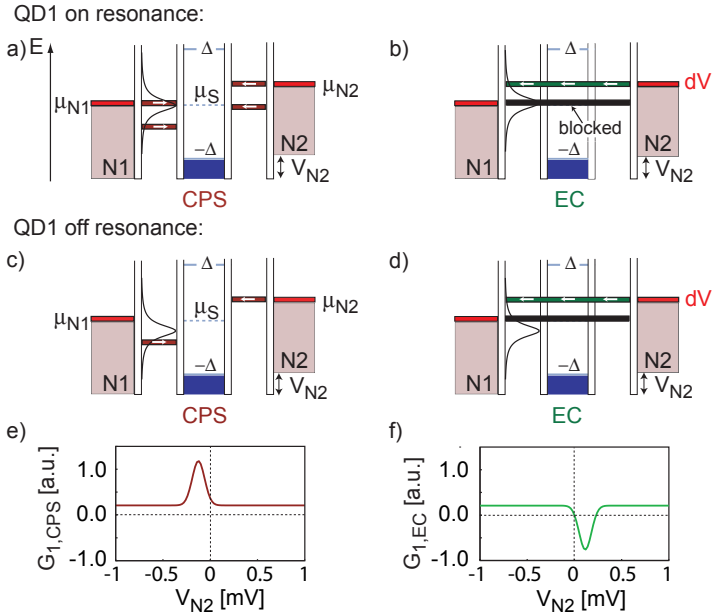

Figure 7.5: Schematics of a) $G_{1,\mathrm{CPS}}$ and b) $G_{1,\mathrm{EC}}$ at finite bias V_2 on QD2 and an ac voltage dV imposed on both QDs if QD1 is positioned on resonance. c) and d) illustrate the pendent of panels a) and b) if QD1 is positioned slightly off resonance. e) and f) are plots of numerically calculated $G_{1,\mathrm{CPS}}$ and $G_{1,\mathrm{EC}}$ for a single resonant level in QD1 and a constant DOS in QD2, to illustrate the off-resonance situation shown in c) and d).

understand that $G_{1,\mathrm{CPS}}$ is positive[4], but decreases with applying V_{N2} since the relevant DOS of QD1 for $G_{1,CPS}$ decreases. Thus, for QD1 being on resonance $G_{1,CPS}$ exhibits a maximum in at $V_{\mathrm{N2}} = 0$ and decreases if μ_{N2} is moved away from the equilibrium situation ($\mu_{N2} = \mu_S$). Please note the constant $G_{1,CPS}$ contribution from CPS processes in an energy window $|2edV|$ around $V_{N1} = 0$ (see Eq. 7.3). The situation is different for elastic co-tunneling (EC) as depicted schematically in Fig. 7.5b. In contrast to CPS, $G_{1,\mathrm{EC}}$ is zero for $V_{\mathrm{N2}} = 0$ V (see Eq. 7.1) and increases with a changing V_{N2} voltage. That $G_{1,\mathrm{EC}} \neq 0$ at finite dc bias is due to the energy dependence of the DOS of QD1: By applying dV, parts of the high DOS in QD1 do not

[4]Note, to deduce the sign of $G_1 = dI_1/dV$ of the individual processes, it needs to be considered that the I_1 is the technical current direction. Furthermore, dV in the experiment is applied on S, not symmetrically on the contacts $N1$ and $N2$.

contribute to the transport anymore (black region in Fig. 7.5b) whereas a smaller QD1 DOS enters the transport window (green region). As visible in Fig. 7.3c (e.g. peak 1), if the DOS of QD1 is in resonance with μ_{N1}, a positive signal in ΔG_1 is measured, which decreases with $|V_{\mathrm{N2}}|$. Thus, from the above reasoning it follows that here CPS dominates over EC.
In Figs. 7.4c, e and f, it is shown that the non-local signal $\Delta G_1(V_{\mathrm{N2}})$ is asymmetric with respect to the equilibrium situation $\mu_{\mathrm{N1}} = \mu_{\mathrm{N2}} = \mu_S$. This can be qualitatively understood by considering Figs. 7.5c and d. There the situation where the DOS of QD1 is off-resonance is depicted (corresponding e.g. to the V_{g1} position of the blue point in Fig. 7.4a). In addition to the dc voltage V_{N2}, a small ac modulation dV is applied on both leads symmetrically. First CPS is considered. Starting from $V_{\mathrm{N2}} = 0$ V, it is intuitively clear that by applying a negative V_{N2} voltage [5], $G_{1,\mathrm{CPS}}$ increases until μ_{N2} is aligned with the DOS resonance in QD1 and decreases afterwards again (see also Fig. 7.5e). Going into the opposite direction, by applying a positive V_{N2} voltage the relevant QD1 DOS for CPS decreases. Thus, it follows that $G_{1,\mathrm{CPS}}$ decreases as well. For comparison, a plot of a numerically calculated $G_{1,\mathrm{CPS}}$ is shown in Fig. 7.5e. It is obtained by using a single resonant level for QD1 and a constant DOS in QD2. In the case of EC, the expected signal is best understood by starting with the $V_{\mathrm{N2}} = 0$ V situation. There $G_{1,\mathrm{EC}}$ is zero (see above). Applying now a negative V_{N2} (see Figs. 7.5d and f), $G_{1,\mathrm{EC}} > 0$ and increases until V_{N2} is entering a voltage regime, where the DOS of QD1 does not change anymore. At the other hand, if a positive V_{N2} voltage is applied, $G_{1,\mathrm{EC}}$ is becoming negative until μ_{N2} is aligned with the QD1 resonance where G_{EC} is maximally negative. Increasing V_{N2} even further, $G_{1,\mathrm{EC}}$ starts to increase (towards a positive value) again. To summarize, EC creates a dip in ΔG_1 at the positive V_{N2} voltage where μ_{N2} is in resonance with the maximum DOS of QD1, whereas CPS is responsible for a peak in ΔG_1 at the corresponding negative V_{N2} voltage. This peak/dip asymmetry is in agreement with the findings e.g. shown in Fig. 7.4e. The asymmetry observed in Fig. 7.4c is opposite than in panel e). This can be explained with the above reasoning, taking the correct position of the DOS of QD1 into account. In the V_{g1} regime where the well defined dips are visible in Fig. 7.3c, EC probably dominates over CPS.
The fact that this model captures all essential features observed in the experiments, allows to attribute the maxima and minima in the differential conductance to either CPS or EC dominating the transport properties. Thus, by applying appropriate voltages they can be separated. In addition, note that the model does not account for the zero-bias features (e.g. Fig 7.4g) in the Coulomb blockade regions. This might be due to used simplification that

[5] This corresponds to an increase of μ_{N2}.

the DOS of QD2 is constant, or it is induced by interactions. Interactions may change the relative rates of CPS and EC and obscure the simple model derived from Eq. 7.1. However, the effects of interactions will have to be studied in more detail to fully understand the involved mechanisms.

7.6 Summary

In summary, preliminary results on finite bias measurements on an InAs nanowire based double quantum dot system coupled strongly to a superconducting lead have been shown. The measurement indicate that the finite bias conductance through one QD depends not only on local processes but contains also signatures of the non-local processes Cooper pair splitting (CPS) and elastic cotunneling (EC). This is substantiated with a simple picture of CPS and EC at finite bias. The experiments establish an additional parameter and a procedure to characterize a CPS device and show that the different higher-order processes obstructing the investigation of CPS depend differently on the bias so that the relative rates can be tuned by external means. In particular, it is shown that a variation of the DOS as a function of energy due to the QD levels, rather than the electromagnetic environment, can be used to favor CPS over EC.
Furthermore, it should be mentioned that the used measurement setup in principle also allows to provide further evidence of Cooper pair splitting. As shown by Recher *et al.* the resonance condition for Cooper pair splitting follows a Breit-Wigner curve, peaking at $\epsilon_{d1} = -\epsilon_{d2} \neq 0$, with $\epsilon_{d1,2}$ being the level position of the two QDs [9]. Thus, applying a small symmetric dc bias on both sides and tuning the energy levels into and out of resonance condition should allow for the detection of Cooper pair splitting. Therefore, control and knowledge over the different higher order tunneling processes at finite bias is essential.

Bibliography

[1] C. Lieber and Z. Wang, MRS Bull. **32**, 99 (2007).

[2] S. D. Franceschi, J. van Dam, E. Bakkers, L. Feiner, L. Gurevich, and L. P. Kouwenhoven, Appl. Phys. Lett. **83**, 344 (2003).

[3] D. Loss and D. P. DiVincenzo, Phys. Rev. A **57**, 120 (1998).

[4] P. Caroff, K. A. Dick, J. Johansson, M. E. Messing, K. Deppert, and L. Samuelson, Nature Nanotechnolgy **4**, 50 (2009).

[5] K. A. Dick, C. Thelander, L. Samuelson, and P. Caroff, Nano Lett. **10**, 3494 (2010).

[6] S. Jin, D. Whang, M. C. McAlpine, R. S. Friedman, Y. Wu, and C. M. Lieber, Nano Lett. **4**, 915 (2004).

[7] S. Nadj-Perge, S. M. Frolov, E. P. A. M. Bakkers, and L. P. Kouwenhoven, Nature **468**, 1084 (2010).

[8] J. Bardeen, L. N. Cooper, and J. R. Schrieffer, Phys. Rev. **108**, 1175 (1957).

[9] P. Recher, E. V. Sukhorukov, and D. Loss, Phys. Rev. B **63**, 165314 (2001).

[10] A. Einstein, B. Podolsky, and N. Rosen, Phys. Rev. **47**, 0777 (1935).

[11] T. S. Jespersen, Ph.D. thesis, Niels Bohr Institute, University of Copenhagen (2007).

[12] M. Scheffler, S. Nadji-Perge, L. P. Kouwenhoven, M. T. Borgström, and E. P. A. M. Bakkers, J. Appl. Phys. **106**, 124303 (2009).

[13] A. E. Hansen, M. T. Bjork, C. Fasth, C. Thelander, and L. Samuelson, Phys. Rev. B **71**, 205328 (2005).

[14] J. Alicea, Phys. Rev. B **81**, 125318 (2010).

[15] M. Koguchi, H. Kakibayashi, M. Yazawa, K. Hiruma, and T. Katsuyama, Jpn. J. Appl. Phys. **31**, 2061 (1992).

[16] M. T. Bjork, A. Fuhrer, A. E. Hansen, M. W. Larsson, L. E. Froberg, and L. Samuelson, Phys. Rev. B **72**, 201307 (2005).

[17] M. W. Larrson, J. B. Wagner, M. Wallin, P. Håkansson, L. E. Fröberg, L. Samuelson, and L. R. Wallenberg, Nanotechnology **18**, 015504 (2007).

[18] J. Trägårdh, A. I. Persson, J. B. Wagner, D. Hessman, and L. Samuelson, Appl. Phys. Lett. **101**, 123701 (2007).

[19] J. Bao, D. C. Bell, F. Capasso, N. Erdman, D. Wei, L. Fröberg, T. Mårtensson, and L. Samuelson, Adv. Mater. **27**, 3654 (2009).

[20] Z. Zanolli, F. Fuchs, J. Furthmüller, U. von Barth, and F. Bechstedt, Phys. Rev. B **75**, 245121 (2007).

[21] A. De and C. E. Pryor, Phys. Rev. B **81**, 155210 (2010).

[22] S. E. Hernández, M. Akabori, K. Sladek, C. Volk, S. Alagha, H. Hardtdegen, N. D. D. Gützmacher, T. Schäpers, and M. G. Pala, cond-mat **1011.1556v1** (2010).

[23] S. Bhargava, H.-R. Blank, V. Narayanamurti, and H. Kroemer, Appl. Phys. Lett. **70**, 759 (1997).

[24] Y.-J. Doh, J. A. van Dam, A. L. Roest, E. P. A. M. Pakkers, L. P. Kouwenhoven, and S. D. Franceschi, Science **309**, 272 (2005).

[25] S. d'Hollosy, *Characterization of ferromagnetic contacts on inas nanowires*, Project work (2009).

[26] L. Hofstetter, A. Geresdi, M. Aagesen, J. Nygård, C. Schönenberger, and S. Csonka, Phys. Rev. Lett. **104**, 246804 (2010).

[27] S. d'Hollosy, Master's thesis, University of Basel (2010).

[28] T. S. Jespersen, M. Aagesen, C. Sorensen, P. E. Lindelof, and J. Nygard, Phys. Rev. B **74**, 233304 (2006).

[29] M. D. Schroer and J. R. Petta, Nano Lett. **10**, 1618 (2010).

[30] A. V. Kretinin, R. Popovitz-Biro, D. Mahalu, and H. Shtrikman, Nano Lett. **10**, 3439 (2010).

[31] S. d'Hollosy, L. Hofstetter, G. Fülop, S. Csonka, A. Baumgartner, and C. Schönenberger, unpublished.

[32] I. Shorubalko, R. Leturcq, A. Pfund, D. Tyndall, R. Krischek, and S. S. und K. Ensslin, Nano Lett. **8**, 382 (2008).

[33] T. Choi, I. Shorubalko, S. Gustavsson, S. Schön, and K. Ensslin, New J. Phys. **11**, 013005 (2009).

[34] A. Pfund, I. Shorubalko, R. Leturcq, and K. Ensslin, Appl. Phys. Lett. **89**, 252106 (2006).

[35] L. P. Kouwenhoven, C. M. Marcus, P. L. McEuen, S. Tarucha, R. M. Westervelt, and N. Wingreen, in *Proceedings of the NATO Advanced Study Institute on Mesoscopic Electron Transport*, edited by L. L. Sohn, L. P. Kouwenhoven, and G. Schön (1997), Kluwer Series E345, pp. 105–214.

[36] L. P. Kouwenhoven, D. G. Austing, and S. Tarucha, Rep. Prog. Phys. **64**, 701 (2001).

[37] T. Ihn, *Semiconductor Nanostructures: Quantum states and electronic transport* (Oxford University Press, 2010).

[38] J. A. van Dam, Ph.D. thesis, Delft University of Technology (2006).

[39] S. D. Franceschi, S. Sasaki, J. M. . Elzerman, W. G. van der Wiel, S. Tarucha, and L. P. Kouwenhoven, Phys. Rev. Lett. **86**, 878 (2001).

[40] J. Kondo, Progress of Theoretical Physics **32**, 37 (1964).

[41] S. M. Cronenwett, Ph.D. thesis, Stanford University (2001).

[42] L. I. Glazman and M. E. Raikh, JETP Lett. **47, No. 8**, 452 (1988).

[43] D. Goldhaber-Gordon, H. Shtrikman, D. Mahalu, D. Abusch-Magder, U. Meirav, and M. A. Kastner, Nature **391**, 156 (1998).

[44] S. M. Cronenwett, T. H. Oosterkamp, and L. P. Kouwenhoven, Science **281**, 5376 (1998).

[45] L. P. Kouwenhoven and L. I. Glazman, Physics World pp. 33–38 (January 2001).

[46] H. Bruus and K. Flensberg, *Many-Body Quantum Theory in Condensed Matter Physics* (Oxford University Press, 2004).

[47] D. Goldhaber-Gordon, J. Göres, M. A. Kastner, H. Shtrikman, D. Mahalu, and U. Meirav, Phys. Rev. Lett. **81**, 5225 (1998).

[48] Y. Meir, N. S. Wingreen, and P. A. Lee, Phys. Rev. Lett. **70**, 2601 (1993).

[49] M. Tinkham, *Introduction to Superconductivity (2nd edition)* (Dover, 2004).

[50] L. N. Cooper, Phys. Rev. **104**, 1189 (1956).

[51] H. Ibach and H. Lüth, *Festkörperphysik (6. Auflage)* (Springer, 2002).

[52] W. Meissner and R. Ochsenfeld, Naturwissenschaften **21**, 787 (1933).

[53] T. M. Klapwijk, Journal of Superconductivity: Incorporating Novel Magnetism **17**, 593 (2004).

[54] T. Heikkilä, Ph.D. thesis, Helsinki University of Technology (2002).

[55] `http://ocw.tudelft.nl/fileadmin/ocw/courses/MesoscopicPhysics/res00016/superconductivity-rev.pdf`.

[56] A. F. Andreev, Sov. Phys. JETP **19**, 1228 (1964).

[57] G. E. Blonder, M. Tinkham, and T. M. Klapwijk, Phys. Rev. B **25**, 4515 (1982).

[58] D. Feinberg, Eur. Phys. J. B **36**, 419 (2003).

[59] G. Deutscher and D. Feinberg, Appl. Phys. Lett. **76**, 487 (2000).

[60] A. Kleine, Ph.D. thesis, University of Basel (2009).

[61] M. J. M. de Jong and C. W. J. Beenakker, Phys. Rev. Lett. **74**, 1657 (1995).

[62] R. J. Soulen, J. M. Byers, M. S. Osofsky, B. Nadgorny, T. Ambrose, S. F. Cheng, P. R. Broussard, C. T. Tanaka, J. Nowak, J. S. Moodera, et al., Science **282**, 85 (1998).

[63] R. Grein, T. Löfwander, G. Metalidis, and M. Eschrig, Phys. Rev. B **81**, 094508 (2010).

[64] F. S. Bergeret, A. F. Volkov, and K. B. Efetov, Phys. Rev. Lett. **86**, 4096 (2001).

[65] K. Lee, M. Duchamp, G. Kulik, A. Magrez, J. W. Seo, S. Jeney, A. J. Kulik, L. Forro, R. S. Sundararn, and J. Brugger, Appl. Phys. Lett. **91**, 173112 (2007).

[66] D. B. Suyatin, C. Thelander, M. T. Bjork, I. Maximov, and L. Samuelson, Nanotechnology **18(10)**, 9361874 (2007).

[67] N. Craig and T. Lester, *Hitchhiker's guide to the dilution refrigerator*, `http://marcuslab.harvard.edu/how_to/Fridge.pdf` (2004).

[68] T. Heinzel, *Mesoscopic Electronics in Solid State Nanostructures* (WILEY-VCH, 2003).

[69] H. Bluhm and K. A. Moler, Rev. Sci. Instrum. **79**, 014703 (2008).

[70] `http://www.syfer.com/Capacitors_1.aspx?id=1:27343&id2=1:27323&id2=1:27297`.

[71] S. Csonka, L. Hofstetter, F. Freitag, S. Oberholzer, T. S. Jespersen, M. Aagesen, J. Nygård, and C. Schönenberger, Nano Lett. **8**, 3932 (2008).

[72] I. Shorubalko, A. Pfund, R. Leturcq, M. T. Borgstrom, F. Gramm, E. Müller, E. Gini, and K. Ensslin, Nanotechnology **18**, 044014 (2006).

[73] A. Kogan, S. Amasha, D. Goldhaber-Gordon, G. Granger, M. A. Kastner, and H. Shtrikman, Phys. Rev. Lett. **93**, 166602 (2004).

[74] J. Paaske, A. Rosch, and P. Wolfle, Phys. Rev. B **69**, 155330 (2004).

[75] J. A. Folk, C. M. Marcus, R. Berkovits, I. L. Kurland, I. L. Aleiner, and B. L. Altshuler, Physica Scripta **T90**, 26 (2001).

[76] R. Hanson, L. P. Kouwenhoven, J. R. Petta, S. Tarucha, and L. M. K. Vandersypen, Rev. Mod. Phys. **79**, 1217 (2007).

[77] H. A. Nilsson, P. Caroff, C. Thelander, M. Larsson, J. B. Wagner, L.-E. Wernersson, L. Samuelson, and H. Q. Xu, Nano Lett. **9**, 3151 (2009).

[78] A. A. Kiselev, E. L. Ivchenko, and U. Rossler, Phys. Rev. B **58**, 16353 (1998).

[79] C. E. Pryor and M. E. Flatte, Phys. Rev. Lett. **96**, 026804 (2006).

[80] C. Fasth, A. Fuhrer, L. Samuelson, V. N. Golovach, and D. Loss, Phys. Rev. Lett. **98**, 266801 (2007).

[81] J. R. Petta and D. C. Ralph, Phys. Rev. Lett. **87**, 266801 (2001).

[82] K. A. Matveev, L. I. Glazman, and A. I. Larkin, Phys. Rev. Lett. **85**, 2789 (2000).

[83] P. W. Brouwer, X. Waintal, and B. I. Halperin, Phys. Rev. Lett. **85**, 369 (2000).

[84] B. N. Murdin, K. Litvinenko, J. Allam, C. R. Pidgeon, M. Bird, K. Morrison, T. Zhang, S. K. Clowes, W. R. Branford, J. Harris, et al., Phys. Rev. B **72**, 85346 (2005).

[85] T. Kontos, M. Aprili, J. Lesueur, and X. Grison, Phys. Rev. Lett. **86**, 304 (2001).

[86] M. Zareyan, W. Belzig, and Y. V. Nazarov, Phys. Rev. Lett. **86**, 308 (2001).

[87] R. S. Keizer, S. T. B. Goennenwein, T. M. Klapwijk, G. Miao, and A. Gupta, Nature **439**, 825 (2006).

[88] D. Beckmann, H. B.Weber, and H. v. Lohneysen, Phys. Rev. Lett. **93**, 197003 (2004).

[89] J. Martinek, M. Sindel, L. Borda, J. Barnaś, J. König, G. Schön, and J. von Delft, Phys. Rev. Lett. **91**, 247202 (2003).

[90] M.-S. Choi, D. Sánchez, and R. López, Phys. Rev. Lett. **92**, 056601 (2004).

[91] J. Martinek, M. Sindel, L. Borda, J. Barna, R. Bulla, J. Koenig, G. Schoen, S. Maekawa, and J. von Delft, Phys. Rev. B **72**, 121302 (2005).

[92] M. Sindel, L. Borda, J. Martinek, R. Bullal, J. König, G. Schön, S. Maekawa, and J. von Delft, Phys. Rev. B **76**, 045321 (2007).

[93] A. N. Pasupathy, R. C. Bialczak, J. Martinek, J. E. Grose, L. A. K. Donev, and P. L. M. D. C. Ralph, Science **306**, 86 (2004).

[94] K. Hamaya, M. Kitabatake, K. Shibata, M. Jung, M. Kawamura, S. Ishida, T. Taniyama, K. Hirakawa, Y. Arakawa, and T. Machida, Phys. Rev. B **77**, 081302(R) (2008).

[95] J. R. Hauptmann, J. Paaske, and P. E. Lindelof, Nature Physics **4**, 373 (2008).

[96] Y. Utsumi, J. Martine, G. Schön, H. Imamura, and S. Maekawa, Phys. Rev. B **71**, 245116 (2005).

[97] I. I. Mazin, Phys. Rev. Lett. **83**, 1427 (1999).

[98] A. Cottet, T. Kontos, W. Belzig, C. Schönenberger, and C. Bruder, Europhys. Lett. **74**, 320 (2006).

[99] H. Soller, L. Hofstetter, S. Csonka, and A. Komnik (2010), unpublished.

[100] M. R. Buitelaar, T. Nussbaumer, and C. Schönenberger, Phys. Rev. Lett. **89**, 256801 (2002).

[101] M. R. Gräber, T. Nussbaumer, W. Belzig, and C. Schönenberger, Nanotechnology **15**, 479 (2004).

[102] J.-P. Cleuziou, W. Wernsdorfer, V. Bouchiat, T. Ondarçuhu, and M. Monthioux, Nature Nanotechnolgy **1**, 53 (2006).

[103] A. Eichler, M. Weiss, S. Oberholzer, C. Schoenenberger, A. L. Yeyati, J. C. Cuevas, and A. Martin-Rodero, Phys. Rev. Lett. **99**, 126602 (2007).

[104] T. Sand-Jespersen, J. Paaske, B. M. Andersen, K. Grove-Rasmussen, H. I. Jørgensen, M. Aagesen, C. Sørensen, P. E. Lindelof, K. Flensberg, and J. Nygard, Phys. Rev. Lett. **99**, 126603 (2007).

[105] T. Sand-Jespersen, M. Aagesen, C. B. Sorensen, P. E. Lindelof, and J. Nygård, J. Vac. Sci. Techn. B **26(4)**, 1609 (2008).

[106] F. Hübler, M. J. Wolf, D. Beckmann, and H. v. Löhneysen, cond-mat **1012.38671v1** (2010).

[107] L. Hofstetter, S. Csonka, J. Nygård, and C. Schönenberger, Nature **461**, 960 (2009).

[108] L. G. Herrmann, F. Portier, P. Roche, A. L. Yeyati, T. Kontos, and C. Strunk, Phys. Rev. Lett. **104**, 026801 (2010).

[109] A. Aspect, P. Grangier, and G. Roger, Phys. Rev. Lett. **49**, 91 (1982).

[110] L. Hardy, Contemporary Physics **39**, 419 (1998).

[111] J. S. Bell, Physics **1**, 195 (1964).

[112] A. Palacios-Laloy, F. Mallet, F. Nguyen, P. Bertet, D. Vion, D. Esteve, and A. N. Korotkov, Nature Physics **6**, 442 (2010).

[113] M. Ansmann, H. Wang, R. Bialczak, M. Hofheinz, E. Lucero, M. Neeley, A. O'Connell, D. Sank, M. Weides, J. Wenner, et al., Nature **461**, 504 (2009).

[114] M. A. Nielsen and I. L. Chuang, *Quantum Computation and Quantum Information* (Cambridge University Press, 2000).

[115] A. Steane, Rep. Prog. Phys. **61**, 117 (1998).

[116] D. Bouwmeester, J. W. Pan, M. Mattle, M. Eibl, H. Weinfurter, and A. Zeilinger, Nature **390**, 575 (1997).

[117] D. Loss and E. V. Sukhorukov, Phys. Rev. Lett. **84**, 1035 (2000).

[118] A. Crepieux, R. Guyon, P. Devillard, and T. Martin, Phys. Rev. B **67**, 205408 (2003).

[119] G. B. Lesovik, T. Martin, and G. Blatter, Eur. Phys. J. B **24**, 287 (2001).

[120] P. Samuelsson, E. V. Sukhorukov, and M. Büttiker, Phys. Rev. Lett. **91**, 157002 (2003).

[121] V. Bouchiat, N. Chtchelkatchev, D. Feinberg, G. B. Lesovik, T. Martin, and J. Torres, Nanotechnology **14**, 77 (2003).

[122] M.-S. Choi, C. Bruder, and D. Loss, Phys. Rev. B **62**, 13569 (2000).

[123] P. Recher and D. Loss, Phys. Rev. B **65**, 165327 (2002).

[124] C. Bena, S. Vishveshwara, L. Balents, and M. P. A. Fisher, Phys. Rev. Lett. **89**, 037901 (2002).

[125] O. Sauret, D. Feinberg, and T. Martin, Phys. Rev. B **70**, 245313 (2004).

[126] J. Torres and T. Martin, Eur. Phys. J. B **12**, 319 (1999).

[127] G. Falci, D. Feinberg, and F. W. J. Hekking, Europhys. Lett. **54**, 255 (2001).

[128] P. Samuelsson and M. Büttiker, Phys. Rev. Lett. **89**, 046601 (2002).

[129] G. Deutscher, J. Supercond. **15**, 43 (2002).

[130] J. P. Morten, A. Brataas, and W. Belzig, Phys. Rev. B **74**, 214510 (2006).

[131] D. S. Golubev and A. D. Zaikin, Phys. Rev. B **76**, 184510 (2007).

[132] S. Russo, M. Kroug, T. M. Klapwijk, and A. F. Morpurgo, Phys. Rev. Lett. **95**, 027002 (2005).

[133] S. Oh and J. Kim, Phys. Rev. B **71**, 144523 (2005).

[134] A. Kleine, B. Baumgartner, J. Trbovic, and C. Schönenberger, EPL **87**, 27011 (2009).

[135] C. W. J. Beenakker, Phys. Rev. B **46**, 12841 (1992).

[136] C. Kurtsiefer, M. Oberparleiter, and H. Weinfurter, Phys. Rev. A **64**, 023802 (2001).

[137] N. W. Ashcroft and N. D. Mermin, *Solid State Physics* (Thomson Learning, 1976).

[138] C. Fasth, A. Fuhrer, M. T. Bjork, and L. Samuelson, Nano Lett. **5**, 1487 (2005).

[139] J. A. Torres, E. Tosatti, A. D. Corso, F. Ercolessi, J. J. Kohanoff, F. D. D. Tolla, and J. M. Soler, Surface Science **426**, L441 (1999).

[140] J. Wei and V. Chandrasekhar, Nature Physics **6**, 494 (2010).

[141] G. Burkard, J. Phys. Condens. Matter **19**, 233202 (2007).

[142] C. Beenakker and C. Schönenberger, Physics Today **56**, 37 (2003).

[143] G. Lesovik, T. Martin, and G. Blatter, Eur. Phys. J. B **24**, 287 (2001).

[144] N. M. Chtchelkatchev, G. Blatter, G. B. Lesovik, and T. Martin, Phys. Rev. B **66**, 161320 (2002).

[145] O. Sauret, T. Martin, and D. Feinberg, Phys. Rev. B **72**, 024544 (2005).

[146] S. Sahoo, T, Kontos, J. Furer, C. Hoffmann, M. Graber, A. Cottet, and C. Schonenberger, Nature Physics **1**, 99 (2005).

[147] H. Aurich, A. Baumgartner, F. Freitag, A. Eichler, J. Trbovic, and C. Schönenberger, Appl. Phys. Lett. **97**, 153116 (2010).

[148] S. Datta and B. Das, Appl. Phys. Lett. **56**, 665 (1990).

[149] A. Bednorz and W. Belzig, cond-mat **1006.4991v2** (2010).

[150] P. Cadden-Zimansky, J. Wei, and V. Chandrasekhar, Nature Physics **5**, 393 (2009).

[151] A. L. Yeyati, F. S. Bergeret, A. Martín-Rodero, and T. M. Klapwijk, Nature Physics **3**, 455 (2007).

[152] D. Chevallier, J. Rech, T. Jonckheere, and T. Martin, Phys. Rev. B **83**, 125421 (2011).

APPENDIX A

Additional data to chapter 6

The results presented in section 6.4 contain evidence for Cooper pair splitting. However, the complexity of the devices may allow for other contributing effects. On the basis of measurements performed on yet another device, this issue is illustrated in this appendix.
The sample fabrication and experimental setup followed the concepts outlined in section 6.2. The main difference was that the two series resistors R_S which served to define the ground potential of the drain contacts, were floating in the experiment shown here. Therefore, for sample characterizations at finite DC bias (e.g. to check for superconducting correlations) the capacitor in front of the I/V converter had to be removed. To prevent damaging the sample, all the gate voltages had to be ramped down to 0 V for this procedure. This can be problematic if the device is not stable and after setup changes not the same QD configuration is found. At the other hand, if R_S is floating, all the ac current will flow through the I/V converter, something which can otherwise only be ensured by proper choices of R_S and the capacitance in front of the I/V input. Both approaches have their advantages. However in retrospective the setup as used in the experiments of chapter 6, would have been the more appropriate choice since it allows directly to analyze the QD states used for the Cooper pair splitting measurements[1].
Nevertheless, experiments were performed with this setup and a sample with

[1] In chapter 7 a more elaborate setup is used, which despite its complexity, should be the choice for all further measurements on Cooper pair splitter devices in this two-quantum-dot Y-junction geometry.

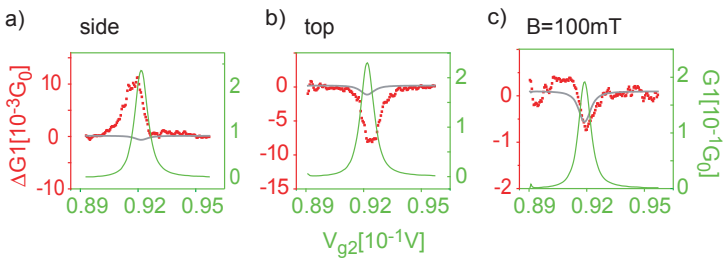

Figure A.1: *Non-local signals $\Delta G_1(V_{g2})$ measured in a third device. The main features of Cooper pair splitting are reproduced. a) Positve signal for positioning the level of QD1 on the side of a resonance and b) negative if measured on resonance. c) By applying a magnetic field (B = 100 mT) larger than the critical field of the superconductor, the non-local signal vanishes as expected.*

charging energies around 2-3 meV, $\Gamma \approx 250 - 500\mu$eV and $\Delta \sim 125\mu$eV. The basic features of the Cooper pair splitting are reproduced as shown in

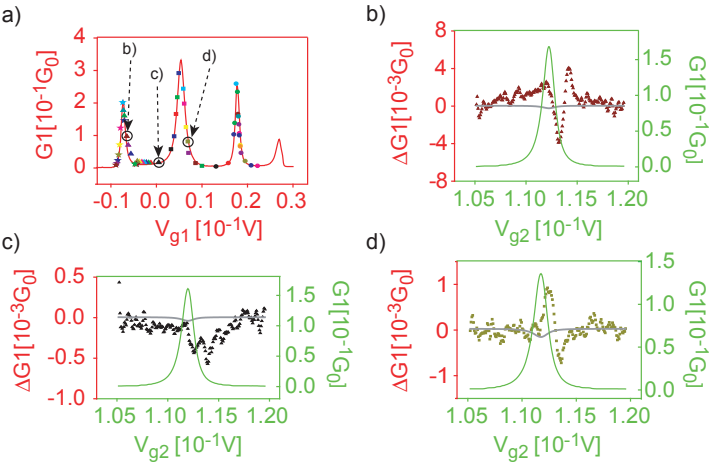

Figure A.2: *a) A $G_1(V_{g1})$ measurement of four Coulomb peaks is presented. The colored points indicate QD1 level positions where experiments, following the description in section 6.3, were performed. In panels b),c) & d) $\Delta G_1(V_{g2})$ of three specific positions (marked in panel a)) is plotted (scattered points). Furthermore the simultaneously measured linear conductance $G_2(V_{g2})$ through QD2 is shown. The light gray curve indicates the resistive cross-talk.*

Fig. A.1. There, the non-local signal $\Delta G_1(V_{g2})$ for two distinct level positions is plotted: on the side of a resonance (panel a)) and on resonance (panel b)). For both cases the signal is in agreement with the findings in section 6.4. As a consistency check a magnetic field B larger than the critical field B_c of the superconductor is applied. As shown in the Fig. A.1c the non-local signal goes over into the calculated resistive cross-talk.
However analysis of more extensive measurements through three QD1 resonances (see Fig. A.2a) revealed additional structures not observed in the devices presented in chapter 6. Some examples of unexpected non-local

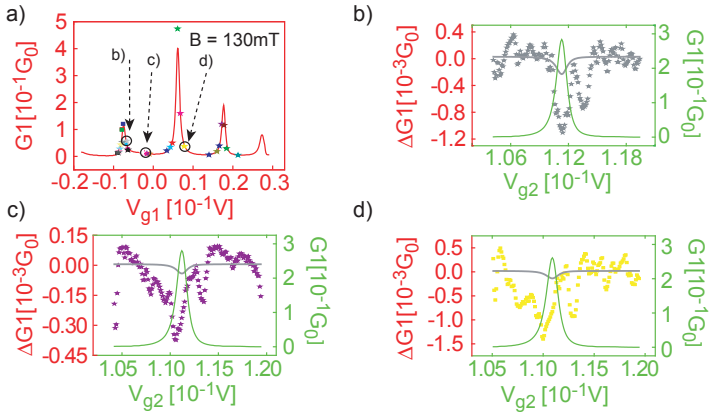

Figure A.3: *a) $G_1(V_{g1})$ measurement at $B = 130$ mT of the same V_{g1} region as in Fig. A.2. In panels b),c) & d) $\Delta G_1(V_{g2})$ of three specific positions (marked in panel a)) is plotted (scattered points).*

signals are presented in Fig. A.2b,c & d. The level positions of QD1 are indicated in Fig. A.2a. Clear signals, larger and different than the resistive cross-talk (light gray curves), but not in agreement with the measurements presented in section 6.4, are observed. Unfortunately the setup did not allow QD level characterization right after these measurements without modifying major gate parameters. This is insofar troubling, since the presence of superconductivity was not seen at all times in the QD spectroscopy of this device. Furthermore, some of these features were sometimes still visible for $B > B_c$, as can be seen in Fig. A.3. In this Figure, for $B = 130$ mT, the outcome of similar measurements as shown in Fig. A.2 are plotted. In many cases large (i.e. larger than the resistive crosstalk) negative signals with multi-peak structures, similar to Fig. A.2c are seen (see panel b,c,d). Positive signals were not observed at any of the measured V_{g1} voltages for

$B = 130$ mT. A major difference to the measurements presented in section 6.4. There, in accordance with the expected origin of the observed signal, namely Cooper pair splitting, the signals vanished always for $B > B_c$ and $T > T_c$.
Therefore, even though Cooper pair splitting may be contained in the signals of Fig. A.2b,c & d, it can not solely account for the observations. A finite interdot coupling Γ_{12} (although not directly observed) between the two QDs could be responsible for these results. To date no convincing explanation for these results exist. However, it highlights the necessity for thorough experimental studies to ensure Cooper pair splitting as the origin of signals in such structures. Furthermore, the complexity of the devices and the therefore connected manifold of possible physical processes, are very nicely demonstrated.

APPENDIX B

Fabrication recipes

The aim of this appendix is to provide the recipes for the used fabrication steps. Besides the common electron beam lithography, it includes rectifying ion etching (RIE), sulfur passivation, argon ion gun treatment, prianha etching and atomic layer deposition (ALD). Recipes for metallization are not given, since they are very material and system dependent (four different systems have been used). For these fabrication steps the reader is referred to the setup specific manuals.

Wafer cleaning

- Cutting highly doped Si wafer with 400 nm SiO_2 to desired size
  - Dopant: p, Boron
  - Resistivity: $0.003 - 0.005\ \Omega$m
- 10 min sonication in acetone
- Rinse in isopropanol (IPA)
- Place in UVO-oven for 10 min

E-beam lithography

- Clean substrate with acetone and afterwards IPA.

- Spin PMMA (AR-P 671.09 950K from ALLRESIST, diluted with Chlorobenzene) to produce ≈ 400 nm thick film (4000 rpm, time 40 s, ramping 4 s).
- Bake for 30 min at 175°C in oven or 5 min at 180°C on hotplate
- Exposure (Parameters for Zeiss Leo supra 40 SEM microscope)
  - Acceleration voltage: 20 kV
  - Working distance: 17 mm
  - Used writefields: (1) 2000 μm, (2) 500 μm and (3) 250 μm
  - Corresponding apertures: (1) 120 μm, (2) 30 μm and (3) 7.5 μm
  - Area dose (for all apertures): 210 $\mu As/cm^2$
  - Line dose (only used with (3)): 1400 pAs/cm
- Develop 90 s in MiBk : IPA = 1 : 3
- Clean in IPA for 30 s.

Rectifying ion etching (RIE) with an Oxford Plasmalab^{80Plus}

- Gas: O_2
- Base pressure: 5×10^{-5} mbar
- Process pressure: 0.25 Torr
- O_2 flow: 16 %
- RF power: 30 W
- Exposure time: 20 - 40 s

In-situ argon ion gun sputtering
Balzers evporating system:

- 30 min argon gas flow (3.2 sccm) through evacuated evaporation chamber → $p_{chamber} \approx 10^{-4}$ mbar
- Recipe 2 on Commenwealth Scientific IBS Controller
  - Cathode current: 5 A
  - Discharge current: 0.1 A
  - Beam current: 20 mA

  - Beam voltage: 500 V
  - Accelerator current: 10 mA
  - Neutralizer: 0
- Exposure: $\approx$ 8 s (PMMA etching rate: 165 Å/min $\pm$ 30 %)
- Switch system off

Bestec evporating system:

- Load device into load-lock, back-side towards the ion gun
- Evacuate load-lock down to $\approx 9 \times 10^{-6}$ mbar
- Open argon bottle and tune gas flow to give a steady chamber pressure of $\approx 5 \times 10^{-5}$ mbar
- Turn on main switch
- Increase Plasma power (tune magnetron voltage) until output current is at 20 mA
- Set extraction voltage to 0.6 kV
- Increase anode voltage to 1 kV (Anode current increases to $\approx$ 0.15 mA)
- Turn sample such that it faces the argon plasma (see also black marker on manipulation rod)
- Exposure: $\approx$ 60 s (PMMA etching rate: 20 Å/min, roughly factor 8.25 between Balzers and Bestec in the etching rate at the given settings)
- Switch system off (reverse process)

Sulfur passivation

- Mix 0.19 g sulfur with 2 ml 21 % NH_4S
- Add 18 ml of deionized (di) H_2O $\rightarrow$ 2 % stock solution
- For passivation 0.4 % solution is desired (i.e. 2 ml stock solution and 8 ml di H_2O
- Passivate for 30 min in H_2O bath at 50°C (alternatively 5 min in a 2 % solution is also possible)
- Immerse into H_2O to clean
- Dry with N_2

Piranha etching

- $H_2SO_4 : H_2O_2 : H_2O = 3 : 1 : 100$
- Etching at 29°C
- Etching rate of InAs NWs $\approx\ 1 - 2$ nm/s (can strongly vary e.g. if NWs are contacted prior to etching)

Atomic layer deposition (ALD) with a Savannah 100 system
Recipe for a ≈ 5 nm Al_2O_3 is given (for more details see [25]).

- Mounting sample into ALD chamber
- Evacuate chamber and set process temperature T= 225°C
- Program recipe and start process (1 cycle produces a layer with a tickness of $\approx 1.1\mathring{A}$)

step	command	number	time	pressure
0	H_2O pulse	0	0.1 s	1 Torr
1	wait	-	15 s	-
2	TMA pulse	2	0.04 s	1.5 Tor
3	wait	-	15 s	-
4	repeat step 0-3 50 times			

- Set T = 80°C and upon reaching it, remove device

Publications

Publications

- *Giant Fluctuations and Gate Control of the g-factor in InAs Nanowire Quantum Dots*, S. Csonka, L. Hofstetter, F. Freitag, S. Oberholzer, T. S. Jespersen, M. Aagesen, J. Nygård and C. Schönenberger, Nano Lett. **8**, 3932-3935 (2008)

- *Cooper pair splitter realized in a two-quantum-dot Y-junction*, L. Hofstetter, S. Csonka, J. Nygård and C. Schönenberger, Nature **461**, 960-963 (2009)

- *Ferromagnetic Proximity Effect in a Ferromagnet-Quantum Dot-Super--conductor Device*, L. Hofstetter, A. Geresdi, M. Aagesen, J. Nygård, C. Schönenberger and S. Csonka, Phys. Rev. Lett. **104**, 246804 (2010)

- *Kondo effect and spin-active scattering in ferromagnet-superconductor junctions*, H. Soller, L. Hofstetter, S. Csonka, A. Levy Yeyati, C. Schönenberger and A. Komnik, (in preparation)

- *Finite bias Cooper pair splitting*, L. Hofstetter, S. Csonka, A. Baumgartner, G. Fülöp, S. d'Hollosy, J. Nygård and C. Schönenberger, arXiv:1105.2583v1

Talks

- *Gate-tunable magnetic exchange in InAs nanowire hybrid structures* Talk at the Swiss Nano 2009 conference, Basel, June 11th - 12th, 2009.

- *Cooper pair splitter realized in a two quantum dot Y-junction*
  Talk at the 6th Capri Spring School on Transport in Nanostructures, April 11th - 18th, 2010.

- *Ferromagnetic proximity effect in a ferromagnet - quantum dot - superconductor devices*
  Talk at annual meeting of Swiss Physical Society, Basel, June 21th - 22nd, 2010.

- *Transport in InAs nanowire hybrid structures*
  Invited talk in the research seminar "Correlated Quantum Systems", University of Heidelberg, November 8th, 2010.

Poster contributions

- *InAs Nanowire based Hybrid Devices*
  Sz. Csonka, L. Hofstetter, A. Renfer, F. Freitag, S. Oberholzer, J. Nygård and C. Schönenberger, poster for the NCCR review panel, April 2008

- *InAs Nanowire based Hybrid Devices*
  Sz. Csonka, L. Hofstetter, A. Renfer, F. Freitag, S. Oberholzer, J. Nygård and C. Schönenberger, poster at the Swiss Workshop on Nanoscience Davos, June 4th - 6th, 2008.

- *Gate-tunable magnetic exchange in InAs NW hybrid structures*
  L. Hofstetter, Sz. Csonka, A. Geresdi, J. Nygård and C. Schönenberger, poster at Spintech V in Krakow, July 7th - 11th, 2009.

- *Cooper pair splitter realized in a two-quantum-dot Y-junction*
  L. Hofstetter, S. Csonka, J. Nygård and C. Schönenberger, poster for the NCCR review panel, April 2010.

Curriculum Vitae

Lukas Hofsetter
December 6 1982 born in Rorschach SG

Education

1995–1999	Kantonale Mittelschule (high school) in Altdorf UR
1999–2000	Exchange year at the Pinckney high school in Michigan, USA
2000–2002	Kontonale Mittelschule (high school) in Altdorf UR, Matura type PAM (Physics und applied Mathematics)
2002–2005	Bachelor of Science in Physics at the University of Basel
2005–2007	Master of Science in Physics at the University of Basel Master thesis in the group of Prof. C. Schönenberger: "Gating of InAs-based heterostructures"
2008–2011	PhD in experimental Physics at the University of Basel PhD thesis in the group of Prof. C. Schönenberger: "Hybrid Quantum Dots in InAs nanowires"

Positions

2003–2005	Teaching assistant in Computer Science
2005–2007	Research assistant in the Computer Science Department of the University of Basel in the group of Prof. H. Burkhart
2008–2011	Teaching assistant for Physics

Awards

2011	Camille und Henry Dreyfus-Stipendium

For valuable lectures during my studies I am indebted to:
G. Baur, B. Binggeli, C. Bruder, G. Burkard, H. Burkhart, A. Bussmann-Holder, M. Calame, M. Grote, H. J. Güntherodt, M. Hegner, K. Hencken, S. Gödecker, H. J. Hug, H.-C. Im Hof, E. Kolbe, B. Krusche, D. Loss, D. Masser, E. Meier, E. Parlow, T. Rauscher, C. Schönenberger, I. Sick, F.-K. Thielemann, D. Trautmann, T. Vetter, D. Zumbühl

Acknowledgments

First and most of all I would like to thank Christian Schönenberger for giving me the opportunity to do a PhD in his group. His unstoppable interest in science is truly motivating and his expertise can not be valued enough. I also like to thank him for the confidence he as been awarding me, often letting me follow my own interests. Furthermore, I am also very grateful to my friend (and collaborator) Szabolcs Csonka. His drive and energy has been highly inspiring. I am very happy and thankful that I had the opportunity to work so closely with him, especially during the first year of my PhD. The knowledge brought across in countless discussions and and his scientific eagerness have influenced me strongly. Köszi!
I also like to express my gratitude to the other members of my PhD committee: Leo Kouwenhoven and Klaus Ensslin. Your willingness to take the time to read my thesis and referee my defense is a great honor.
For support and discussions I am gratified to the entire InAs nanowire team from Basel and Budapest: Samuel d'Hollosy, Attila Geresdi, Gergő Fülöp and Peter Makk. Many shared hours in and outside the lab have led to precious insights into the field of InAs nanowire quantum dots and have been simply also a good time. Furthermore, I would like to acknowledge all the members of the office 1.25: Andreas Kleine, Hagen Aurich, Frank Freitag, Alex Eichler, Jens Schindele, Samuel d'Hollosy, Julia Samm, Matthias Bräuninger, Stefan Nau and Oren Knopfmacher. The hours of joy and jokes alongside the possibility of profound physics discussions have been a essential part for my daily motivation. Thank you all! Also the other PhD students need to be mentioned: Jon Agustsson, Jan Brunner, Toni Fröhlich, Cornelia Nef, Alexey Tarasov, Mathias Wipf, Roman Huber, Erasmus Bieri, Gunnar Gunnarsson, Dino Keller, Zheng-Ming Wu and Songmei Wu. Moreover I would like to acknowledge the present and former postdocs in our group during my thesis: Andreas Baumgartner, Markus Weiss, Stefan Ober-

holzer, Michel Calame, Jelena Trbovic, Claire Barett, Wangyang Fu, Romain Maurand, Jianhui Liao and Haichao Huang. Especially I like to thank Andreas Baumgartner for shortening the countless hours in front of the MCK fridge. It has been great fun. I also highly appreciated your support in the interpretation of the finite bias data as well as your comments on my thesis. Special thanks go to Henning Soller from Heidelberg. With his theoretical support, explanations for data presented in chapter 5 have been found. In various discussions and mails he has taken the time to increase my understanding of the complicated models used to describe the experiments. Furthermore I would like to acknowledge Verena Körting and Daniel Loss for their theoretical support and fruitful discussions.
I am also grateful for the support from the electronic and mechanical workshop. Especially I would like to mention Michael Steinacher, Dominik Sifrig, Daniel Sacker and Patrik Stöcklin. Furthermore, special thanks goes to Barbara Kammermann and Astrid Kalt from the secretary for their help in the jungle of bureaucracy.
Surely, I am very thankful to all my friends for helping me to detach from the lab and their support in more difficult times. I also like to mention Jim Sansone, my host-father in the USA. This year in the USA influenced my life. Thank you Jim. In addition, I am highly indebted to my family: without their support I would now not be there where I am. I can not thank you enough!
And last I would like to express my greatest gratitude towards Bene. It is fascinating to see how far one can get by doing 78 km: Merci infiniment!